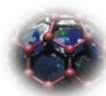JOURNAL OF

LOW DIMENSIONAL SYSTEMS

Physics, Chemistry and Biology of Low Dimensional Systems

November 2019

Aims and scope

Journal of Low Dimensional Systems publishes research and review papers on fundamental aspects of applied physics, chemistry and biology. Papers reporting work on electronic, spectroscopic and structural properties of low dimensional systems, including perfect and defect lattices, surfaces, two-dimensional electron systems, interfaces, thin films and multilayers, amorphous materials, layered-, micro- and nanostructures. This journal accepts articles related to the biomaterials for medical purposes as well.

Typical examples include the preparation and characterization of novel and advanced materials, concerning their electrical, magnetic, optical, thermal and mechanical properties and the application of appropriate experimental and theoretical techniques in these realms.

Journal of LDS

Table of Contents

LUMINESCENT PROPERTIES OF CADMIUM AND ZINC SULPHIDES, OBTAINED BY CHEMICAL PRECIPITATION FROM SOLUTION

E. F.NASIROV

Institute for Physical Problems, Baku State University

The luminescence of cadmium sulfide and zinc sulfide films obtained from halide (Cl, Br, I) thiourea coordination compounds has been studied. It is shown that the formation of impurity and intrinsic centers of radiative recombination is determined not only by preparative conditions, but also by the chemical nature of the initial thiourea coordination compounds.

1. INTRODUCTION

It is known that the defective structure of semiconductors and, therefore, their most important properties largely depend on the method of production. This allows you to directly influence the formation of certain lattice defects. The method of obtaining metal sulfides from coordination compounds (CC) with thiourea provides opportunities for controlling the properties of sulfides by designing CC of different composition and structure [1]. When producing films based on cadmium and zinc sulfides, this can be implemented in three ways: by introducing coordinated anionic substituents, such as halogen impurities [2]; the introduction of complexing cationic substituents to obtain solid solutions, for example, CdS (Cu) [2], $Cd_xZn_{1-x}S$ [3]; controlled self-disordering of the anion sublattice, including due to deviations from stoichiometry.

In the present work, comparative studies of the photoluminescence (PL) of cadmium and zinc sulfide films obtained from thiourea CC solutions under different conditions were carried out to study the effect of the production conditions on the formation of luminescence centers due to the different nature of the initial CC.

2. EXPERIMENT

The CdS and ZnS films were grown by the method of aerosol pyrolysis [1] from solutions of halide (Cl, Br, I) thiourea Cd and ZnCS on a heated cellulose substrate. The substrate temperature was varied between 250 and 500° C (±5°C). The thickness of the films is 30 - 200 nm.

According to [3], when metal sulfide is formed during thermal destruction of a thiourea CC, the first coordination sphere of the metal in the sulfide lattice is "inherited" from the nearest environment of the metal atom in the CC. In our case, when using a CC with the general formula $[Me(thio)_2\Gamma_2]$ (where Me = Cd, Zn; thio is the S-coordinated thiourea molecule; G = Cl, Br, I) there are distorted tetrahedral fragments $MeS_2\Gamma_2$, which repeat the coordination of the cation-forming agent and playing a major role in the construction of the sulfide lattice. When using these CC, this makes it possible, firstly, to alloy the sulphide with halogens directly in the production process, and, secondly, to significantly affect the defects of the anionic sublattice.

The PL spectra of the films in the region of 400-850 nm, excited by the radiation of the LGI-21 nitrogen laser (λ = 337 nm), were recorded at 250°C using an automatic spectral setup described in [6]. The spectral resolution is not worse than 10 nm.

The PL spectra of cadmium sulfide films obtained from halide CC, have a similar appearance and are characterized by the presence of two intense bands with maxima in the region of 810-840 nm (Fig. 2, a - c). In the case of films obtained from the $[Cd(thio)_2Cl_2]$ and $[Cd(thio)_2Br_2]$ complexes, the dependences of the intensity of these bands on the preparation temperature have a maximum at T ~ 350°C and at 450-500°C the 820 nm band almost completely disappears (Fig. 3, a and b). These features can be explained, assuming that the 820 nm band is due to the existence of defect complexes of the form $(V_{Cd}V_S)^{\times}$. Sulfur vacancies are formed due to the presence of coordinated halogen atoms, which "loosen" the lattice in the process of separating sulfide from the CC. It can be expected that with an increase in the production temperature to a certain limit, the number of sulfur vacancies (V_S)

increases, which are then filled with oxygen to form complexes $(V_{Cd}O_S)''$ responsible for the 830-840 nm emission [2, 6]. Such a transformation of the centers with increasing temperature explains the disappearance of the 820 nm band.

The vacancy nature of this band is also indicated by the ratio of the intensities of the 820 and 840 nm bands for films deposited from chloride and bromide CC. As can be seen from Fig. 1, a and b, the "vacancy" band for films obtained from $[Cd(thio)_2Cl_2]$ is markedly weaker, probably due to the larger size mismatch of the bromine atom to the sulfur site in the CdS structure. In this connection, the influence of coordinated bromine on the anion sublattice is somewhat larger. This assumption agrees with a significantly more "slower" drop in τ_1 for films of chloride complexes as compared with films of bromide thiourea complexes.

a

b

c

d
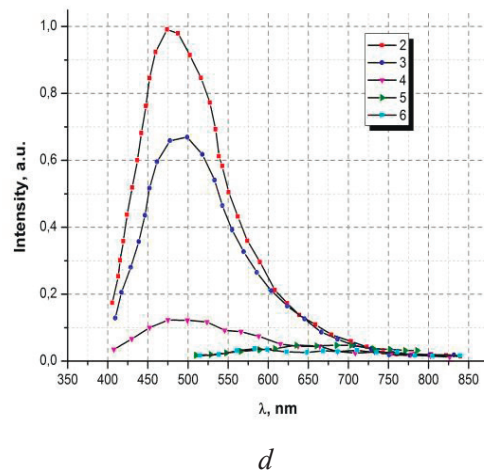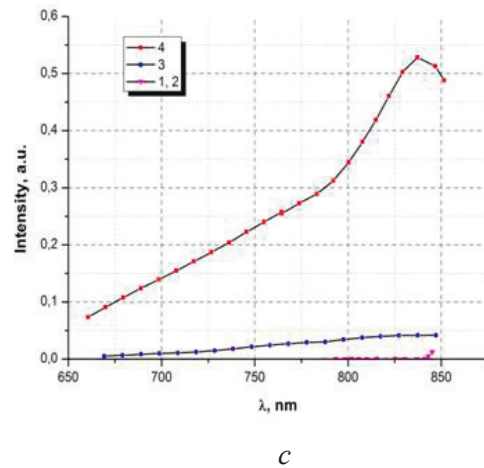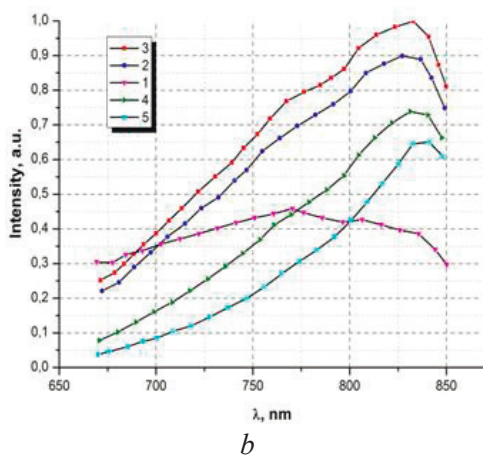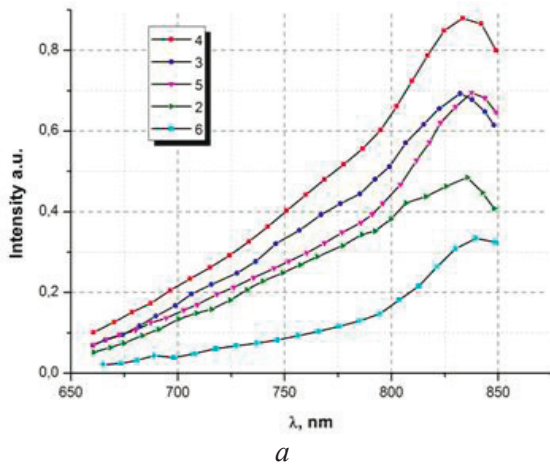
Figure 1. PL spectra of CdS films obtained from $[Cd(thio)_2Cl_2]$ (*a*), $[Cd(thio)_2Br_2]$ (*b*), $[Cd(thio)_2I_2]$ (*c*) and $[Zn(thio)_2Cl_2]$ (*d*) at a temperature of 250 (1), 300 (2), 350 (3), 400 (4), 450 (5) and 500°C (6)

The decrease in the intensity of the red glow at high temperatures is consistent with the assumptions about an increase in the electron drift mobility, made on the basis of the results of the microwave photoconductivity study. If we take the capture cross section with traps σ $\sim 10^{-14}$ cm^2 [4] and the average thermal velocity v $\sim 10^7$ cm * s^{-1}, then with a typical average value $\tau_1 \sim 100\text{-}200$ ns we get the estimate for the trap concentration is N = $1/\tau_1\sigma_v \sim 10^{14}$ cm^{-3}, which really corresponds to a relatively pure crystal.

3. RESULTS AND DISCUSSION

This assumption is consistent with the data of [4] for $Cd_xZn_{1-x}S$ compounds and with preliminary results of X-ray analysis and also correlates with the known process of "healing" imperfections with oxygen O_i [5], which begin to build into i-positions, and the "effect of

stepwise cleaning" of the film with T> 300°C [6]. In similar cases, exciton spectra were observed even at room temperature [7]. It seems surprising that, in our samples, the obtained estimate of the electron acceptor concentration did not show luminescence due to interband recombination. Apparently, the recombination rate constant for free electrons and holes is very small.

For the film obtained from $[Cd(thio)_2Br_2]$ at a minimum temperature of 250°C, close to the decomposition temperature of the CC (220-230°C), the PL spectrum contains a band of 760-770 nm, which by analogy with $(V_{Cd}Cl_S)'$ [8] can attributed to the complex $(V_{Cd}Br_S)'$. It should be noted that the intensity of the 810-840 nm bands is minimal, but increases sharply with increasing temperature when bromine is removed (Fig. 2, b). In this case (T ~ 250-300⁰C), the time τ_1 sharply decreases, which indicates a decrease in the concentration of electron traps. These data also indirectly confirm the nature of the 810–840 nm bands associated with (V_S) and (O_S).
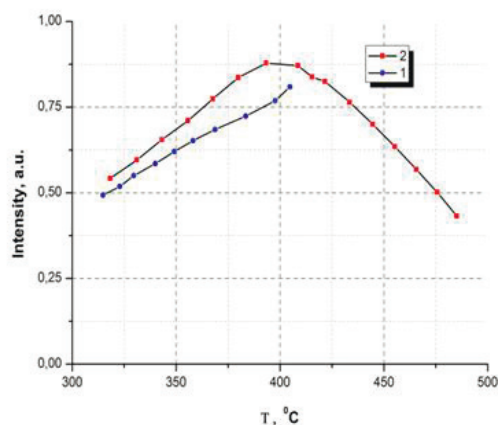
a
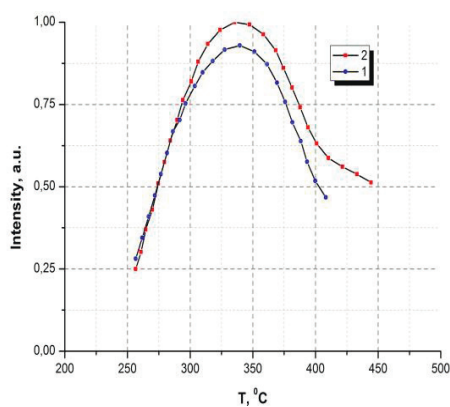
b
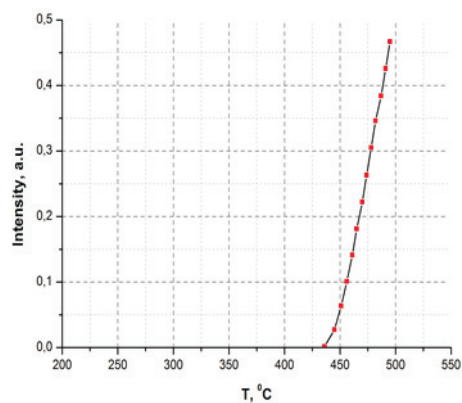
c
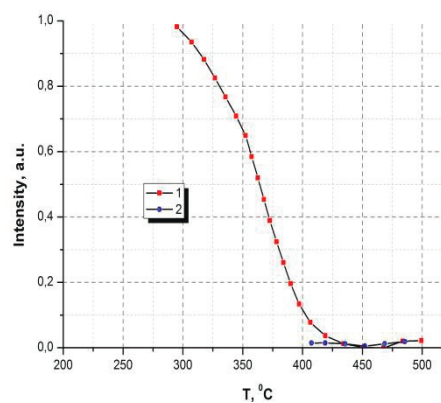
d

Figure 2. Dependence of the intensity of the 820 (1), 840 (2), 490 (1') and 670 nm (2') bands on the CdS film production temperature: *a* - from $[Cd(thio)_2Cl_2]$, *b* - $[Cd(thio)_2Br_2]$, *c* - $[Cd(thio)_2I_2]$, *d* - $[Zn(thio)_2Cl_2]$

The band 760-770 nm is blurred, which indicates its complex structure. In addition, at T > 250°C, the broadening of red bands in the short-wavelength region is partially preserved, possibly indicating the presence of (Br_S) even at these temperatures.

When studying the nature of the thermal decomposition of a CC and the properties of sulfide films, it was noted that iodide CC and the films obtained from them stand out against the general background and are anomalous in a number of properties. Indeed, the films obtained from the iodide complex have a single "oxygen" band in the red region (Fig. 1, c), the intensity of which increases sharply with increasing temperature (Fig. 2, c). These features are due to the mutual influence of ligands in the $[Cd(thio)_2I_2]$ complex, which affects the defective structure of sulfide. Iodine atoms with a large covalent radius are practically not capable of replacing sulfur in

the site and are actively replaced by oxygen in the process of sulphide release in an oxidizing atmosphere.

The PL spectrum of zinc sulfide precipitated from $[Zn(thio)_2Cl_2]$ solution has an intense band at 490 nm (Fig. 2, d), which is attributed to the presence of (Cl_S) [9], which is also indicated by the temperature dependence of the band intensity (Fig. 2, d). The weak band at 670 nm, which appears at 450-500ºC, seems to be associated with (V_S) or oxygen centers formed when chlorine releases the S-node. Note that the comparatively weaker influence of coordinated chlorine on the luminescence of CdS(Cl) films as compared to ZnS(Cl) is associated with the nature of the cadmium – CC zinc. The Zn-Cl bond is more polar than Cd-Cl, which results in a more durable chlorine retention during the destruction of $[Zn(thio)_2Cl_2]$.

4. CONCLUSION

Thus, not only the preparative conditions, but also the chemical nature of the starting materials determines the properties of the films obtained by the pyrolysis of thiourea complexes. The chemical nature of the starting materials may determine their properties as suppliers of controlled and uncontrolled impurities in the final product, as well as the nature of defects in it.

5. REFERENCES

1. Vorokh A.S., Rempel A.A. / Direct-space visualization of the short and "average" long-range orders in the noncrystalline structure of a single cadmium sulfide nanoparticle JETP Lett., 2010, 91, p.100.
2. Junkermeier C.E., Lewis J.P., Bryant G.W. / Amorphous nature of small CdS nanoparticles: Molecular dynamics simulations, Phys. Rev. B, 2009, 79, p.125323.
3. Masaya Ichimura, Kazuki Takeuchi, Atsushi Nakamura, Eisuke Arai / Photochemical deposition of Se and CdSe films from aqueous solutions, Thin Solid Films, 384 Ž, 2001. p.157-159.
4. Shena C.M., Zhang X.G., Lib H.L./ Influence of different deposition potentials on morphology and structure of CdSe films, Applied Surface Science 2005, 240, p. 34–41.
5. Nabiyouni G., Sahraei R., Toghiany M., Majles Ara M. H. and Hedayati K ./ Preparation and characterization of nanostructured ZnS thin films grown on glass and n-type Si substrates using a new chemical bath deposition technique, Rev.Adv.Mater.Sci. 2011, 27, p.52-57.
6. Mayorova T.L., Klyuyev V.Q., Semenov V.N., Bolqova T.Q., Naumov A.V. / Luminescent properties of the cadmium sulfide polycrystalline films, doped with I group metals, Messenger of VSU, 2005, v.2, p. 38-44, (in Russian).
7. Valentyn Smyntyna, Bogdan Semenenko, Valentyna Skobeeva, and Nikolay Malushin / Photoactivation of luminescence in CdS nanocrystals, Beilstein J Nanotechnol, 2014, v. 5, p. 355–359.
8. Joseph R. Lakowicz, Ignacy Gryczynski, Zygmunt Gryczynski, Catherine J. Murphy / Luminescence Spectral Properties of CdS Nanoparticles,.*J. Phys. Chem. B,* 1999, 103, (36), p.7613-7620. DOI: 10.1021/jp991469n
9. Andrea I. Lorgu, Cristian Matei, Daniela Berger, L. Alexandrescu / Synthesis of Photoluminescent pure and doped cadmium sulfide by reverse Microemulsion method. Chalcogenide Letters, 2012, v. 10, p.525-531

ELECTRICAL, PHOTOELECTRICAL CHARACTERIZATION AND GAS SENSITIVITY OF P-Si/pS/CdS and p-Si/pS/Cd$_{0.4}$Zn$_{0.6}$O HETEROJUNCTIONS

Kh.M. AHMEDOVA

Faculty of Physics, Department of Physical Electronics, Baku State University,
Az1148, Z.Khalilov str., 23, Baku, Azerbaijan

Nanostructure porous silicon layers with systematically varied pore size of 8-70 nm were fabricated onto the p-type c-Si wafers with (100) orientation using electrochemical anodizing method from HF+ethanol and HF+ethanol+CdCl2 solutions (respectively, PS and PSCD hereafter). Gas- and photo-sensors based on c-Si/PS (or PSCD)/CdS and c-Si/PS/Cd$_{0.4}$Zn$_{0.6}$O heterojunctions were synthesized by depositing of CdS and Cd$_{0.4}$Zn$_{0.6}$O films onto the c-Si/PS (or PSCD) substrates by electrochemical deposition (ED hereafter). The morphological properties of the PS and PSCD layers, CdS and Cd$_{0.4}$Zn$_{0.6}$O films were studied by scan electron microscopy (SEM). Gas and photo-sensitivity properties of heterojunctions were studied as a function of pore size. The optimal pore size is determined, which provides the maximum gas- and photo-sensitivity of heterojunctions in this study. It was established that the heterojunctions based on PSCD, possess higher gas- and photo-sensitivity, than heterojunctions based on PS.

1. INTRODUCTION

Currently, materials prepared by low-temperature electrochemical processing of semiconductors, in particular, PS, formed by electrochemical etching of monocrystalline silicon (c-Si) are of particular interest. On the other hand, nanostructured PS has emerged as an attractive material in the field of photo-electronics due to its broadband gap, wide optical transmission range, favorable absorption spectrum, and surface texture. So, PS has disadvantages, also. The surface of the PS was covered with Si-H$_x$ bond groups immediately after the deposition. In the process of storage in air, the Si-H$_x$ bond groups are replaced by Si-O$_x$ bond groups and ultimately, silicon nanocrystallites are covered by an amorphous layer which is the main reason for the instability and degradation of all electrical, photovoltaic, photoluminescent and sensor devices based on PS. There are various technological methods used for the passivating of the PS surface. For example, in [1], the passivating of PS was performed at the excretory hydrogen plasma. Passivating of PS can also be done by inserting different elements into the matrix. For example, in [2], the author's employed carbohydrate solutions in the PS matrix and then tried to carbide the matrix by thermal annealing. As the authors point out, carbohydrates decompose at temperatures of 2000C and are converted to carbon and water vapor. Since carbohydrates are not volatile, almost all carbon in them remains in the pores. At this time, the size of the molecules of the selected carbohydrate should be smaller than the size of the pores. The authors have chosen sucrose as a conventional carbohydrate product. In some cases, the process of passage of hydrogen and oxygen in the PS was carried out directly with the deposition process. For this purpose, various salts (AuCl3, FeCl3, NaNO2, KIO3, CrO3, etc.) were added to the solution in the deposition process [3-8]. In [3, 4], gold and iron chloride salts were added at different concentrations during the dissolution of PS. The main purpose of the study was to replace the non-stable Si-H$_x$ complexes by Si-Au or Si-Fe stable bonds. It has been established that anodizing in a metallic atmosphere not only stabilizes, but also improves the electrical and optical parameters of PS.

Therefore, for the purpose of comparison, the results of investigations of the morphological, electrical and photoelectrical parameters of heterojunctions p-Si/CdS and p-Si/Cd$_{0.4}$Zn$_{0.6}$O based on PS [9, 10] and PSCD are considered in this chapter.

2. EXPERIMENT

P-type single-crystal Si wafer with orientation of (100), resistivity of 0.01-2.5 Ohm×cm and thickness of 0.2-0.6 μm was etched through an electrochemical process to produce the porous structure. Before anodizing, the c-Si surface was cleaned from the SiO$_2$ oxide layer as well as contaminants, in an aqueous solution of hydrofluoric acid (HF), washed with de-ionized water at a temperature of 80°C and ethyl

alcohol, and then, dried in air. Anodizing of the c-Si substrate surface was carried out in a Teflon chamber with a platinum cathode [9, 10].

HF:ethanol (1:1) solutions with and without $CdCl_2$ (aqueous solution of $CdCl_2$ in 10:1 concentration was added to solution) were used for the formation of porous silicon. The anodizing current was 40-70 mA/cm^2. Depending on the anodizing time (30-1800 seconds) and potential in solutions, PS layers (prepared from solution without CdCl2) and PSCD layers (prepared from solution with CdCl2) with the pore sizes of 8-70 nm was prepared on the c-Si surface. For the comparison, electrical and photoelectrical properties of heterojunctions on the base of PS and PSCD layers, prepared at same anode potentials (20; 25 and 30 V) were investigated. After the formation of PS and PSCD layers, the samples were immersed in ethyl alcohol, dried in air, and placed in an electrochemical bath for deposition of nanostructured CdS and $Cd_{0.4}Zn_{0.6}O$ films.

Electrochemical deposition of CdS and $Cd_{0.4}Zn_{0.6}O$ films onto the c-Si/PS and c-Si/PSCD substrates was carried out at a temperature of 80°C in an aqueous solutions of $CdCl_2+Na_2S_2O_3$ and $Zn(NO_3)_2+Cd(NO_3)_2$ (99.5% purities) salts, respectively (Table 1) [9-11].

Table 1. Mole fraction of salts, deposition current and potential for the CdS and $Cd_{0.4}Zn_{0.6}O$ films.

Samples	Mole fraction of salts (mM)		Deposition current and potential	
CdS	$CdCl_2$	$Na_2S_2O_3$	J (mA/cm²)	U_c (V)
	200	50	20	-0.82
$Cd_{0.4}Zn_{0.6}O$	$Zn(NO_3)_2$	$Zn(NO_3)_2$	J (mA/cm²)	U_c (V)
	5.92	3.95	3.4	-1,2

Cyclic voltammetry based on obtaining and decoding the current-voltage dependences of the polarized electrode-electrolyte solution interface, was used to control electrochemical reactions in each solutions, and then, in their combined solution with the same concentration and pH. Cyclic voltammograms were scanned in the potential range from 1.2 to -1.2 V with the graphite (or Ag/AgCl) electrodes. Depending on the deposition time and pore size of the substrate, the 100-600 nm thick CdS and $Cd_{0.4}Zn_{0.6}O$ films with various surface morphologies were deposited. All the films showed n-type conductivity.

In order to fabricate the heterojunctions, an Ohmic In (or Au) electrode, in grid form was evaporated on the CdS and $Cd_{0.4}Zn_{0.6}O$ films with an area of ~0.62 cm^2 (Figure 1). Aluminum (Al) was evaporated on the back side of the p-Si wafer as the Ohmic electrode,

followed by annealing at 500°C in vacuum for 20 min.
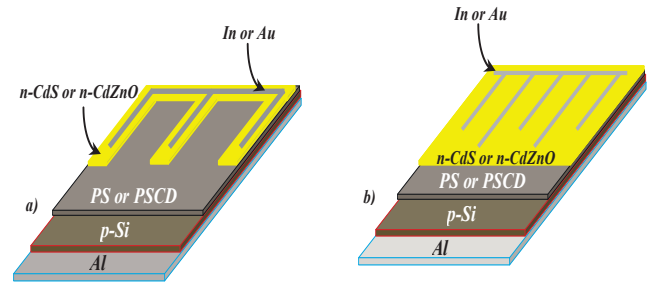
Figure 1. Schematic structure of gas sensors (a) and solar cells (b) on the basis of PS and PSCD

Electrical characterization and gas sensitivity of p-Si/PS/CdS and p-Si/PS/$Cd_{0.4}Zn_{0.6}O$ heterojunctions

Electrical properties of heterojunctions were studied depending on the crystallite and pores size. Current-voltage characteristics (*J-V*) of all heterojunctions show rectification, which rectification factor values and current passage mechanism through junction region depends on the pores and crystallite size. Figure 2 represents the *J-V* characteristics for as-deposited heterojunctions of p-Si/PSCD/CdS and p-Si/PSCD/$Cd_{0.4}Zn_{0.6}O$ based on PSCD1, PSCD2 and PSCD3 substrates. The pass direction corresponds to positive polarity of the external bias on the *c*-Si layers.
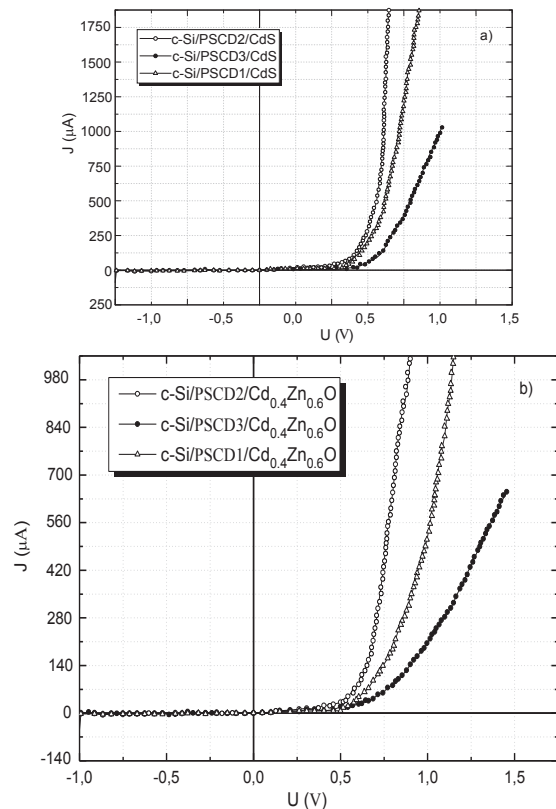
Figure 2. Dark J-V curves for as-deposited c-Si/PSCD/CdS and c-Si/PSCD/Cd$_{0.4}$Zn$_{0.6}$O heterojunctions prepared onto the PSCD1, PSCD2 and PSCD3 substrates.

The rectification at U=1V, increases from 2340 up to 4670 for c-Si/PSCD/CdS and from 780 up to 1650 for c-Si/PSCD/Cd$_{0.4}$Zn$_{0.6}$O heterojunctions, when replacing the PSCD1 substrates with PSCD2. As seen from Table 2, rectification in both types of heterojunctions is decrease sharply, when PSCD3 is used as substrate.

Table 2. Electrical parameters of c-Si/PSCD/CdS and c-Si/PSCD/Cd$_{0.4}$Zn$_{0.6}$O as-deposited heterojunctions depending on the pores size in Si

Samples	Substrates	Ideality factor	Rectification factor
c-Si/PSCD/CdS	PSCD1	1.5	2340
	PSCD2	1.24	4670
	PSCD3	2.67	1076
c-Si/PSCD/Cd$_{0.4}$Zn$_{0.6}$O	PSCD1	1.66	780
	PSCD2	1.35	1650
	PSCD3	2.84	240

It is assumed that the change in rectification factor value depending on the pore size is due to the oxygen or nitrogen molecules, because in order to remove excess water from pores and films, heterojunctions were dried in air, just after the deposition (as-deposited heterojunctions). In this case, adsorbed oxygen or nitrogen molecules to the silicon pores (mainly for PSCD3 substrates) create the acceptor states in junction region and thus increase recombination acts. It is established that the degree of adsorption depends on pores size. To confirm this fact, heterojunctions were heat treated in vacuum at 50-70°C and *J-V* characteristics were taken in vacuum. It is established that, the rectification in heterojunctions deposited onto the PSCD2 substrates, remained almost unchanged (Table 3). But the rectification in both type of heterojunctions on the base of PSCD3 substrates increases sharply, which, by our opinion, is due to desorption of oxygen or nitrogen molecules (Table 3).

Table 3. Electrical parameters of heterojunctions c-Si/PSCD/CdS and c-Si/PSCD/ Cd$_{0.4}$Zn$_{0.6}$O heat treated in vacuum at 50-70°C, depending on the pores size in Si

Samples	Substrates	Ideality factor	Rectification factor
c-Si/PSCD/CdS	PSCD1	1.5	2346
	PSCD2	1.24	4680
	PSCD3	1.63	1954
c-Si/PSCD/Cd$_{0.4}$Zn$_{0.6}$O	PSCD1	1.66	785
	PSCD2	1.35	1670
	PSCD3	1.75	1087

To prove this, we carried out additional experiments on these heterojunctions. Direct current at U= 1 V was measured in air with different concentrations. Direct current in heterojunctions with PSCD2 not changed, and in heterojunctions with PSCD3 decreased with increasing air concentration (Fig. 3).

Dependence of direct current at U=1 V for heterojunctions with PSCD1, PSCD2 and PSCD3, on the concentration of various gases (oxygen, nitrogen, methane and ethanol vapor) have been investigated. As seen from Fig. 4 the direct current decreases at insignificant change of the gas concentration. It is suggested that heterojunctions with PSCD3 can be used as gas sensors.

Experiments carried out in various atmospheres on heterojunctions with PSCD1, showed insignificant changes of current and junctions with PSCD2 do not showed any change of direct current, i.e. they have stable parameters. This fact testifies that heterojunctions with PSCD1 and PSCD2 can be used for manufacturing of solar cells.
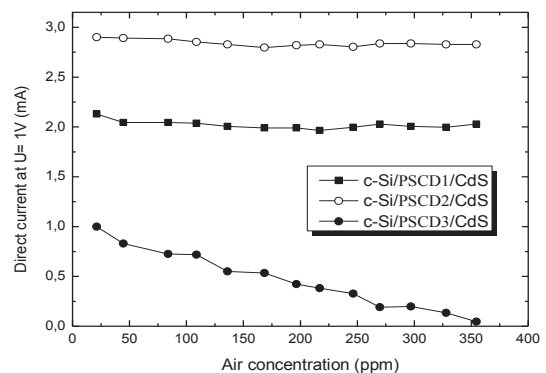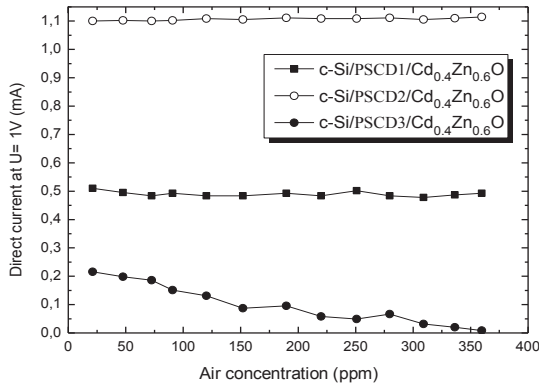
Figure 3. Dependence of direct current at U=1 V on the air concentration for as-deposited heterojunctions of c-Si/PSCD/CdS and c-Si/PSCD/Cd$_{0.4}$Zn$_{0.6}$O with different pores size.
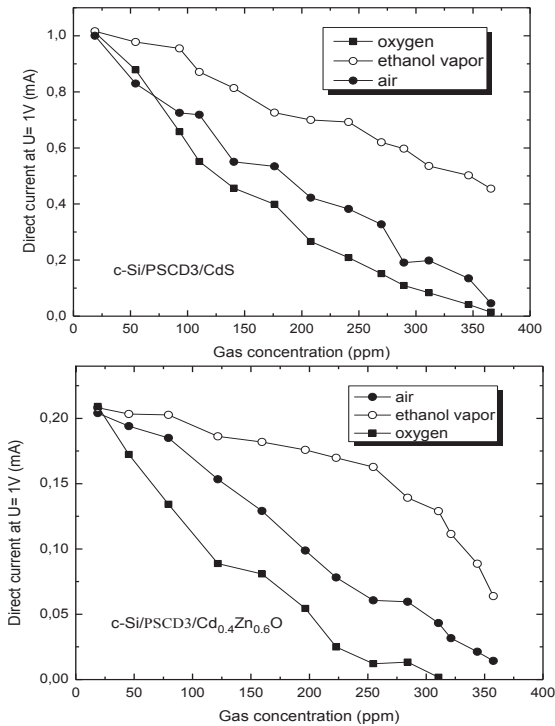
Figure 4. Dependence of direct current at U=1 V on the concentration of different gases for heterojunctions c-Si/PSCD3/CdS and c-Si/PSCD3/Cd$_{0.4}$Zn$_{0.6}$O.

The *J-V* characteristics of heterojunctions with PSCD1 and PSCD2, in natural log scale and temperature dependences of diode saturation current testify that there is the tunnel-recombination mechanism of current through the junction region at direct voltages and *J-V* characteristics of the these heterojunctions can be presented by expression:

$$= {}_0J\left[exp\left(\frac{eU}{nkT}\right) - 1\right] \qquad (1)$$

here, J_0 is the saturation current density, U is the applied voltage, e is the electron charge, n is the ideality factor, k is the Boltzmann constant, and T is the temperature.

At room temperature the ideality factor value for heterojunctions with PSCD1 were approximately 1.5 and 1.66, respectively for the heterojunctions c-Si/PSCD1/CdS and c-Si/PSCD1/Cd$_{0.4}$Zn$_{0.6}$O. The decrease of ideality factor has been observed, when PSCD2 substrates is used (Table 3).

Fig. 5 shows the room temperature capacitance-voltage (*C-V*) characteristics of heterojunctions c-Si/PSCD/CdS and c-Si/PSCD/Cd$_{0.4}$Zn$_{0.6}$O, with PSCD1 and PSCD2 substrates. The linearity of the *C-V* characteristics in $C^{-2}(V)$ coordinates indicates a sharp distribution of uncompensated acceptor impurities within the space charge region for both types of heterojunctions with PSCD2. Unlike it, *C–V* characteristics of heterojunctions c-Si/PSCD/CdS and c-Si/PSCD/Cd$_{0.4}$Zn$_{0.6}$O, with PSCD1 substrates have peculiarities, typical for heterojunctions with the presence of defects at the junction region. Since, the C–V characteristics of these junctions are poorly linearized in $C^{-2}(V)$ coordinates and its slope changes by frequency of the alternating signal. As seen from the figures, the value of cut-off voltage (V$_c$) is more in comparison with heterojunctions based on PSCD2 substrates. It can be explained by the participation of oxygen (as Si-O$_x$ bonds) on the surface of PSCD1 substrates, which can form the oxide layer (as CdO or Cd$_{1-x}$Zn$_x$O) between the porous silicon and CdS (Cd$_{1-x}$Zn$_x$O) films. This is confirmed by the frequency dependence of straight sections of the $C^{-2}(V)$ slopes, which indicates increase of heterojunction capacity with increasing frequency.
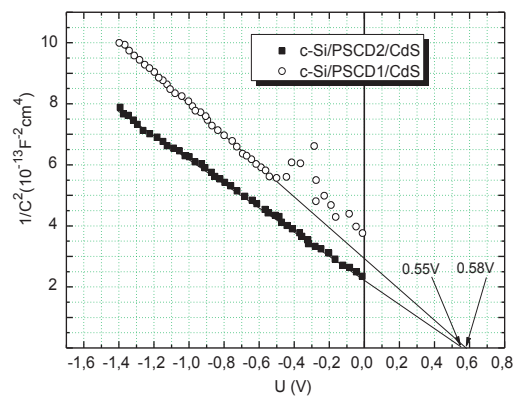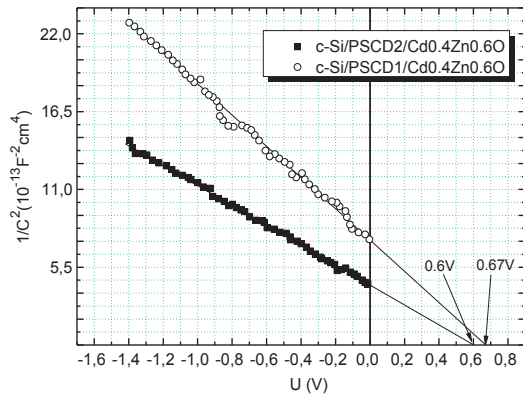
Figure 5. Capacitance-voltage characteristics of heterojunctions c-Si/PSCD/CdS and Si/PSCD/Cd$_{0.4}$Zn$_{0.6}$O c-based on PSCD1 and PSCD2 substrates

Photosensitivity of p-Si/PS/CdS and p-Si/PS/Cd$_{0.4}$Zn$_{0.6}$O heterojunctions

Investigated heterojunctions of c-Si/PSCD/CdS and c-Si/PSCD/Cd$_{0.4}$Zn$_{0.6}$O based on PSCD substrates demonstrated photovoltaic performances under AM1.5 illumination (W=100 mW/cm^2), which sign of open circuit photo-voltage (U$_{oc}$) does not change in all region of photosensitivity. However, the values of U$_{oc}$ and J$_{sc}$ non-monotonically dependent on the type of PSCD – maximum photosensitivity show the heterojunctions based on PSCD2 substrates (Fig. 6).
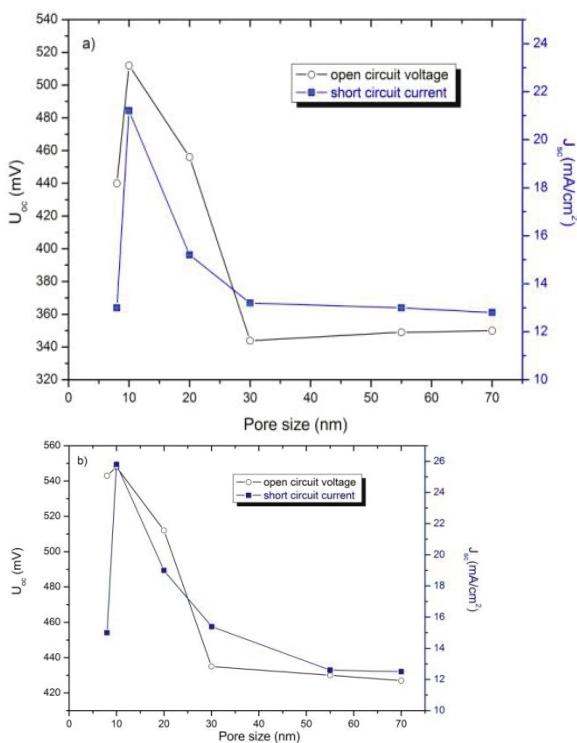
Figure 6. Dependences of U$_{oc}$ and J$_{sc}$ on the pore size in silicon for heterojunctions c-Si/PSCD/Cd$_{0.4}$Zn$_{0.6}$O (a) and c-Si/PSCD/CdS (b)

Spectral distribution of photocurrent (J$_{ph}$) in heterojunctions c-Si/PSCD/CdS and c-Si/PSCD/Cd$_{0.4}$Zn$_{0.6}$O with different type of PSCD were investigated in a wavelength range of 300÷1300 nm (Fig. 7).
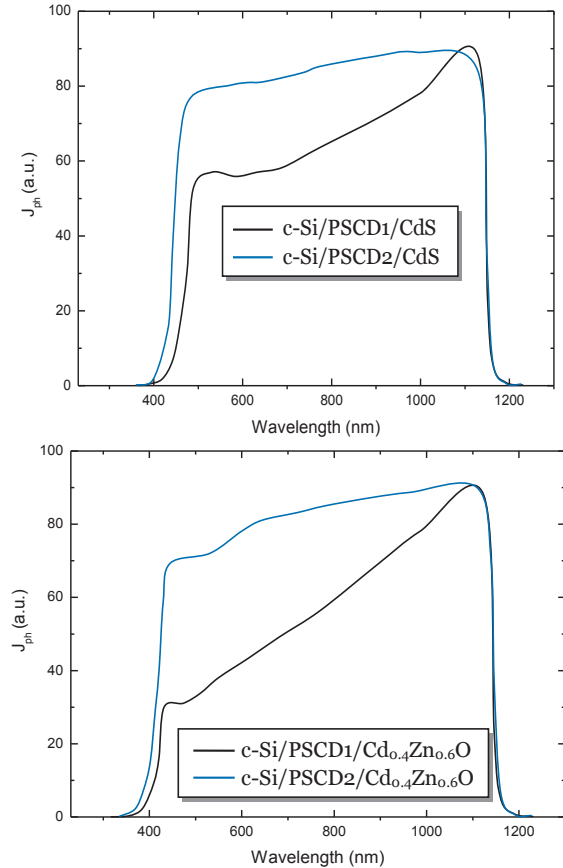
Figure 7. Spectral distribution of photocurrent for heterojunctions c-Si/PSCD/CdS and c-Si/PSCD/Cd$_{0.4}$Zn$_{0.6}$O, based on PSCD1 and PDCS2 substrates

It is established that the profile of J$_{ph}$ spectrum depends on the pore size and morphology of CdS and Cd$_{0.4}$Zn$_{0.6}$O films. As seen from the figure short wavelength peaks for heterojunctions c-Si/PSCD/CdS and c-Si/PSCD/Cd$_{0.4}$Zn$_{0.6}$O based on PSCD1, is observed respectively, at 510 nm and 420 nm, which corresponds to the band gap of CdS and Cd$_{0.4}$Zn$_{0.6}$O films. However, long-wavelength peak of spectrum at 1125 nm is due to the direct interband transitions in *c*-Si. It can be seen from Figure 7, that heterojunctions of c-Si/PSCD/CdS and c-Si/PSCD/Cd$_{0.4}$Zn$_{0.6}$O demonstrate good photo-response in the wavelength range of 512 ÷ 1125 nm and 425 ÷ 1125 nm and, which is not observed by us in heterojunctions of c-Si/A$_2$B$_6$ [13].

Table 4. Photoelectrical parameters of heterojunctions c-Si/PSCD/CdS and c-Si/PSCD/Cd$_{0.4}$Zn$_{0.6}$O heat treated in vacuum at 50-70°C, depending on the pores size in Si

Samples	Substrates	U_{oc}, mV	J_{sc}, mA/cm^2	FF	η, %
c-Si/PSCD/CdS	PSCD1	543	15	0.62	5.05
	PSCD2	548	25.8	0.68	9.61
	PSCD3	435	15.4	0.6	4.01
c-Si/PSCD/Cd$_{0.4}$Zn$_{0.6}$O	PSCD1	440	13	0.55	3.15
	PSCD2	512	21.2	0.61	6.62
	PSCD3	344	13.2	0.52	2.36

It is assumed that this is due to light absorption in porous silicon. The slight shift of short-wavelength peak in both type of heterojunctions to the more short-wavelength region of spectrum, with increasing pores size (for PSCD2), associated by us with the nano-structural properties of CdS and Cd$_{0.4}$Zn$_{0.6}$O films [9-12]. However, an increase of the optical path of light in nano-structured films leads to increase of degree of the light absorption, therefore, heterojunctions based on PSCD2, shows greater efficiency compared heterojunctions based on PSCD1 (Table 4).

3. CONCLUSIONS

Gas- and photo-sensors based on c-Si/PS (or PSCD)/CdS and c-Si/PS/Cd$_{0.4}$Zn$_{0.6}$O heterojunctions were fabricated by electrodepositing of CdS and Cd$_{0.4}$Zn$_{0.6}$O films onto the c-Si/PS (or PSCD) substrates SEM images confirmed that the morphological properties of CdS and Cd$_{0.4}$Zn$_{0.6}$O films are governed by the pore size of PS and PSCD. The maximum gas- and photo- sensitivity were achieved in heterojunctions based on PSCD, when the pores were 30 nm and 10 nm, respectively. The pronounced PS pore diameter and anodizing regime dependence of the photo- and gas- sensitivity is the main novelty of the present work. We believe that this phenomenon could be exploited in other similar heterojunction types and even in hybrid solar cells containing e.g. a perovskite charge separation layer.

4. REFERENCES

1. Venger EF, Holiney RY, Matveeva LA, Vasin AV. / The influence of hydrogen plasma on the spectrum of electromotive reflections and the spectrum of electronic states of porous silicon. Semiconductors. 2003; 37, p.103-107.
2. Sreseli OM, Goryachev DN, Osipov VY, Belyakov LV, Vul SP, Serenkov IT, Sakharov VI, Vul AY. / Preparation and study of carbidized porous silicon. Semiconductors. 2002; 36, p.574-580.
3. Primachenko VE, Kononets JF, Bulakh BM, Venger EF, Kaganovich ÉB, Kizyak IM, Kirillova SI, Manoilov ÉG, Tsyrkunov YA. / The electronic and emissive properties of Au-doped porous silicon. Semiconductors. 2005; 39, p.565-571.
4. Shevchenko OYu, Goryachev DN, Belyakov LV, Sresli OM. / Optical properties of iron-passivated nanoporous silicon. Semiconductors. 2010, 44, p.642-646.
5. Xu YK, Adachi S. / Properties of light-emitting porous silicon photoetched in aqueous HF/FeCl3solution. Journal of Applied Physics. 2007, 101(10), p.103509. DOI: 10.1063/1.2733752
6. Xu YK, Adachi S. / Properties of light-emitting porous silicon formed by stain etching in HF/KIO3 solution under light illumination. Journal of Applied Physics. 2008, 103(10), p.103512. DOI: 10.1063/1.2924423
7. Fathauer RW, George T, Ksendzov A, Vasquez RP. / Visible luminescence from silicon wafers subjected to stain etches. Applied Physics Letters. 1992, 60(8), p.995-997. DOI: 10.1063/1.106485
8. Farshid Karbassian. / Porous Silicon, Porosity - Process, Technologies and Applications, Taher Hcine Ghrib, IntechOpen: 2018. p.36 DOI: 10.5772/intechopen.72910.
9. Mamedov HM, Muradov MB, Konya Z, Kukovecz A, Kordas K, Shah SI, Mamedova VC, Ahmedova KM, Tagiyev EB, Mamedov VU. / Fabrication and characterization of c-Si/Porous-Si/CdS/Zn$_x$Cd$_{1-x}$O heterojunctions for applications in nanostructured solar cells. Photonics Letters of Poland. 2018, 10: p.73-75. DOI: 10.4302/plp.v10i3.813
10. Mamedov HM, Kukevecz A, Konya Z, Kordas K, Shah SI, Mamedov VU, Ahmedova KM, Mamedova VJ, Rzaev RM, Shamilova ShA, Khanmamedova EA, Agazade LE. / Characteristics of c-Si/porous-Si/CdS heterojunctions. News of Higher Educational Institutions. Physics (Russian journal of applied physics). 2018, 61, p.96-101.DOI: 10.1007/s11182-018-1584-2
11. Mamedov HM, Mamedov VU, Mamedova VJ, Ahmedova KM, Tagiyev EB, Agazade LE. /

Nano-structure solar cells on the base of p-Si/Cd$_{1-x}$Zn$_x$O thin film heterojunctions. Journal of Optoelectronics and Advanced Materials. 2018, 20, p.468 – 473.

12. Mamedov HM, Shah SI, Chirakadze A, Mamedov VU, Mamedova VJ, Ahmedova KM. / Photovoltaic performance of p-Si/Cd$_{1-x}$Zn$_x$O heterojunctions. Photonics Letters of Poland. 2018, 10, p. 26-28. DOI: 10.4302/plp.v10i1.797

13. Abdinov ASh, Mamedov HM, Hasanov HA, Amirova SI. / Photosensitivity of p, n-Si/n-Cd$_{1-x}$Zn$_x$S heterojunctions manufactured by a method of electrochemical deposition. Thin Solid Films. 2005, 480-481, p. 388-391.

FABRICATION of $Cu_{1.75}$ $In_{0.05}$Te MONOCRYSTALS AND INVESTIGATION OF STRUCTURE TRANSITION

H.B. GASIMOV[1], R.M. RZAYEV[1], H.M. MAMEDOV[2,1], V.U. MAMEDOV[2,1]

[1] Azerbaijan State University of Economics, Istiglaliyyat str. 6, Baku, Azerbaijan, Az1001
[2] Baku State University, Z.Khalilov str., 23, Baku, Azerbaijan, Az1148

In the present paper the influence of isovalent substitution of Cu2+ metal ions by the In2+ metal ions on the elemental crystal lattice parameters and phase transition temperature have been investigated by the roentgenographic method in $Cu_{1.75}$Te single crystals fabricated by Bridgman method. For determine the monocrystalline and monophasicity of $Cu_{1.75}$In0.05Te crystals obtained by this method, was carried out lauegram and provided X-ray phase analysis by diffractometer. The parameters of $Cu_{1.75}$Te crystal structure increases by the substituting of Cu2+ metal ions by In2+ isovalent metal ions. This increase is related to the difference in the ion radius of the metal ions of In2+ -0.92 Å and replaced Cu2+ -0.80 Å, in the $Cu_{1.75}$Te crystal structure.

1. INTRODUCTION

Because of photo-, opto- and nanoelectronics, which are the most important areas of modern electronics, are so rapidly developed; these areas of electronics always require the creation of new materials and the detailed study of the physical properties of existing materials. Undoubtedly, in this aspect, the main responsibility lies in solid matter electronics and solid matter physics. Thus, the known semiconductors are not always useful for the preparation of semiconductor modulus of demanded parameters. The management of their properties by changing the composition of these materials has received much attention. Therefore, there is a need for the technological process of synthesis and screening of special materials with the necessary complex physical, chemical and electro physical properties. In addition, successful development of the semi-conductive materials acquisition technology is the basis of modern semiconductor electronics and allows for the creation of multiple devices for different purposes.

The possibility of changing the basic parameters by composition opens up broad perspectives, which in turn enables them to learn about the nature of the interaction of the components in the investigated systems. From this point of view simple and complicated chalcogenide systems of Cu-Te system, are significantly promising.

Crystals of the Cu-Te system are one of the main semiconducting materials used in the manufacture of various electrical and thermoelectric devices, solar cells and solar panels. The research of crystals of these systems received great interest because the researchers have always been looking for the new methods of their acquisition technology. Due to, by using various additives the physical and chemical properties of these systems are manageable and in the certain temperature range these system are rather stable, it occurs a need for further improvement of physical and chemical properties of the Cu-Te system crystals.

According to the phase diagram, except the stoichiometric phases of CuTe and Cu_2Te [1], there are also non-stoichiometric phases Cu_{2-x}Te [2,4]. At room temperature the Cu_2Te combination is crystallized in structure with a_0=4.237 Å, c_0=7.274 Å, F.qr.P6/mmm (D_{6h}^1), z=2 parameters. For Cu_2Te combination it has also been defined orthorhombic structure with a=$2a_0$=7.328 Å, b=$3a_0$=22.203 Å, c=$5c_0$=37.69 Å parameters [4]. The investigation of Cu_{2-x}Te non-stoichiometric system crystals have shown that, in contrast to $Cu_{1.75}$Te and $Cu_{1.80}$Te crystals, the crystals of $Cu_{1.90}$Te, $Cu_{1.85}$Te are consist two-phase system: hexagonal and orthorhombic phases [5-8].

For one of the non-stoichiometric phases of the Cu-Te systems $Cu_{1.75}$Te hexagonal structure has been determined a=$2a_0$=8.28 Å, c=c_0=7.22 Å parameters at room temperature [2]. At room temperature, the $Cu_{1.75}$Te phase also has metastable form β1, β2, β3 modifications [6]. It was determined that, at the room temperature Cu-Te system compounds have duality in phase and several modifications. That's why fabrications of their monocrystals, phase analysis and various physical-chemical properties produce difficulties [9-10]. In this regard, the research of Cu-Te system becomes relevant for researchers.

In this work, we present fabrication of $Cu_{1.75}$In$_{0.05}$Te monocrystals by the method of Bridgeman and investigation of structure transition of this monocrystals.

2. EXPERIMENTAL

In order to obtain monocrystals of the $Cu_{1.75}In_{0.05}Te$ system, the ampoule was filled with high purification of Cu, In, Te chemical elements and was synthesized by direct fusion in 10^{-2} Pa vacuum. Then, the quartz ampoules with conical form of ends were filled synthesized sample and again were formed by Bridgeman monocrystalline method in 10^{-2} Pa vacuum. For determine the monocrystalline and monophasicity of $Cu_{1.75}In_{0.05}Te$ crystals obtained by this method, was carried out lauegram, then the sample was transformed into powder and provided X-ray phase analysis by DCS-910, ADVNCE-8D diffractometer (Table 1).

Table 1. Report of the diffractogram of crystalline powder of $Cu_{1.75}In_{0.05}Te$. CuK_α -radiation, 40kv, 40mA, λ=1.5418Å .

№	$Cu_{1.75}Te$		$Cu_{1.75}In_{0.05}Te$		Hexagonal phase		T,K
	d_{exp}, Å		d_{exp}, Å		d_{theo}, Å	hkil	
1	3.6140		3.6187		3.6083	0006	
2	3.2204		3.2241		3.2295	1013	
3	2.7117		2.7143		2.7062	0008	
4	2.5565		2.5613		2.5525	1016	
5	2.4107		2.4128		2.4106	0009	
6	2.2703		2.2740		2.2700	1128	
7	2.1692		2.1726		2.1656	1018	
8	2.0852		2.0897		2.0850	1120	
9	1.9990		2.0032		2.0021	1019	
10	1.8061		1.8106		1.8057	2020	
11	1.7553		1.7586		1.7517	2023	
12	1.6130		1.6164		1.6148	2026	
13	1.5728		1.5764		1.5756	1129	
14	1.4982		1.5012		1.5018	112.10	293
15	1.4427		1.4460		1.4441	2029	
16	1.3559		1.3570		1.3532	2132	
17	1.3390		1.3418		1.3412	2133	
18	1.2755		1.2770		1.2767	2136	
19	1.2052		1.2064		1.2019		
20	1.1880		1.1907		1.1874	3033	
21	1.1418		1.1429		1.1419	3036	
22	1.0908		1.0937		1.0999	3038	
23	1.0450		1.0476		1.0425	2240	

As a result, it has been established that the crystalline sample $Cu_{1.75}In_{0.05}Te$ crystal is monocrystalline, uniform and crystallizes in a hexagonal structure with c=c$_0$=21.7168 Å, F.qr.p6/m2-(D$_{3h}^1$). As we can see, all of the diffraction lines listed in Table 1 are fully indexed in accordance with the parameters defined in [2], as well as the calculated parameters based on Table 1 are identical to those calculated in [2].

As can be seen from the table, when Cu^{2+} metal ions are replaced by isovalent In^{2+} metal ions in the crystalline structure crystal lattice parameters are increased than a = 3.8803 Å, c = 21.6920 Å parameter, calculated at room temperature for $Cu_{1.75}Te$ crystals. The determined increase is related to the difference in the ion radius of the isovalent substituting metal ions of In^{2+} (0.92 Å) and substituted metal ions of Cu^{2+} (0.80 Å) in crystalline structure $Cu_{1.75}Te$.

Table 2. Diffractogram of monocrystalline $Cu_{1.75}In_{0.05}Te$. CuK_α -radiation, 40kv, 40mA, λ=1.5418Å.

№	$Cu_{1.75}Te$	$Cu_{1.75}In_{0.05}Te$	Hexagonal phase		FCC-phase		T,K
	d_{exp}, Å	d_{exp}, Å	D_{theo}, Å	hkil	D_{th}, Å	hkl	
1	10.8262	10.8705	10.8475	0002	-	-	
2	7.2351	7.2549	7.2317	0003	-	-	
3	5.4270	5.4377	5.4238	0004	-	-	
4	3.6140	3.6187	3.6158	101¯0; 0006	-		
5	2.7117	2.7143	2.7119	0008	-	-	
6	2.4107	2.4128	2.4106	0009	-	-	
7	2.1692	2.1726	2.1695	000.10	-	-	293
8	1.8061	1.8106	1.8079	202¯0; 000.12	-	-	
9	1.5496	1.5520	1.5496	000.14	-	-	
10	1.3559	1.3570	1.3559	000.16	-	-	
11	1.2052	1.2064	1.2053	303¯0	-	-	
12	1.1404	1.1429	1.1418	000.19	-	-	
1		11.0975	10.8475	0002	-	-	
2		7.3545	7.2317	0003	-	-	
3		5.5163	5.4238	0004	-	-	
4		3.6727	3.6158	0006	-	-	
5		2.7549	2.7119	0008	-	-	
6		2.4487	2.4106	0009	-	-	
7		2.2030	2.1695	000.10	-	-	
8		1.8367	1.8079	202¯0; 00012	-	-	
9		1.5736	1.5496	000.14	-	-	693
10		1.3774	1.3559	000.16	-	-	
11		1.2246	1.2053	303¯0; 000.18	-	-	
12		1.160	1.1418	000.19	-	-	
1	-	3.5248	-	-	3.5202	111	730

The difference of the substituent ion radius in this mutually isovalent substitution is 0.15%, which is within the limits of V.M.Goldshmid for the conditions of the isomorphism. Accordingly, electronegativity in the $Cu_{1.75}Te$ crystal lattice is not violated and as the polarizers impact of Cu^{2+} ions are stronger than the In^{2+} ions we suppose that, the tense in the elemental crystal lattice of $Cu_{1.75}Te$ will decrease.

3. RESULTS AND DISCUSSION

In order to determine of structure transition in $Cu_{1.75}In_{0.05}Te$ monocrystals and effect of In^{2+} metal ions, which replaces Cu^{2+} ions in the $Cu_{1.75}Te$ crystal structure in this transition, at a room temperature at $0 \leq 2\theta \leq 90°$ angle interval (0001) atomic plane 12 diffraction line was noted (Table 2). Then, in every 100 K was obtained diffractograms at the temperature range $293 \div 793$ K. As can be seen from Table 2, all diffraction lines are indexed in a single-dimensional manner according to the crystal lattice parameters set out in [2]. At 793 K temperature, all of the 12 diffraction lines belonging to the home temperature phase are disappeared and only indexed diffraction lines belonging to the face centralized high temperature cube phase (111) becomes visible. The transition to the hexagonal $\leftrightarrow$ cube phase in $Cu_{1.75}In_{0.05}Te$ monocrystal occurring at temperature of $725 \pm 1K$ and it is determined on the basis of the intensities of the diffraction line. It has been identified, that the specified cross-section is monocrystalline-monocrystalline type characteristic. For the high temperature cube phase "a" parameter was determined as a = 6.1053 Å. With the temperature rise the parameters of the home temperature of the monocrystal $Cu_{1.75}In_{0.05}Te$ increase in linearly (Figure 1). Note that the increase in the value of the crystal lattice "c" parameter goes farther than the "a"-parameter.
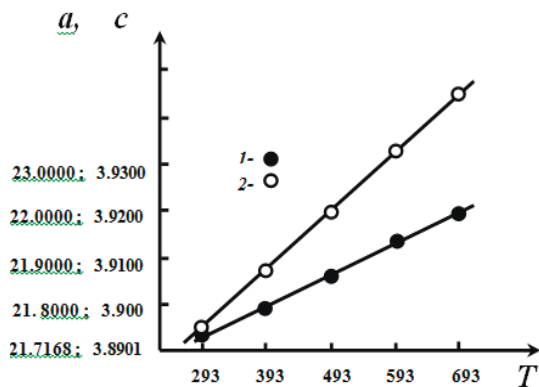
Figure 1. Temperature dependence of crystal lattice parameters in monocrystals of $Cu_{1.75}In_{0.05}Te$

As seen from the phase transition temperature determined for the $Cu_{1.75}In_{0.05}Te$ monocrystals, the In^{2+} metal ions which substitutes Cu^{2+} ions in the $Cu_{1.75}Te$ crystal structure, slides the phase transition temperature to the temperature of increase zone in the $Cu_{1.75}Te$ monocrystals.

The results obtained during the research can be summarized as follows:
- The sample containing $Cu_{1.75}In_{0.05}Te$ was synthesized and its monocrystalline was grown by the Bridgman method. After X-ray phase analysis, it's obtained that, $Cu_{1.75}In_{0.05}Te$ monocrystalline crystallizes in hexagonal structure with a_o=3.8901 Å, c_{or}=21.7168 Å, F.qr. p6/m2-(D_{3h}^1) parameters.
- The parameters of $Cu_{1.75}Te$ crystal structure increases by the substituting of Cu^{2+} metal ions by In^{2+} isovalent metal ions. This increase is related to the difference in the ion radius of the metal ions of In^{2+} - 0.92 Å and replaced Cu^{2+} -0.80 Å, in the $Cu_{1.75}Te$ crystal structure.
- The hexagonal $\leftrightarrow$ cube transition which occurs at $725 \pm 1K$ in $Cu_{1.75}In_{0.05}Te$ monocrystalline is reciprocal and its monocrystalline - monocrystalline type. For high temperature cube phase "a" parameter has been set as a = 6.1053Å. It has been defined that, as In^{2+} metal ions substitute Cu^{2+} ions in the $Cu_{1.75}Te$ crystal structure, the transition temperature slides to the temperature of increase zone.

4. CONCLUSION

The influence of isovalent substitution of Cu^{2+} metal ions by the In^{2+} metal ions on the elemental crystal lattice parameters and phase transition temperature have been investigated by the roentgenographic method in $Cu_{1.75}Te$ single crystals fabricated by Bridgman method. For determine the monocrystallinity and monophasicity of $Cu_{1.75}In_{0.05}Te$ crystals obtained by this method, was carried out lauegram and provided X-ray phase analysis by diffractometer. The parameters of $Cu_{1.75}Te$ crystal structure increases by the substitutung of Cu^{2+} metal ions by In^{2+} isovalent metal ions. This increase is related to the difference in the ion radius of the metal ions of In^{2+} -0.92 Å and replaced Cu^{2+} -0.80 Å, in the $Cu_{1.75}Te$ crystal structure.

5. REFERENCES

1. Hansen, M., & Anderko, K. Constitution of Binary Alloys. McGrow Hill Book Co. Inc., NY, 1958, p.638.
2. Baranova, R.V., V.P. Aref'ev and S.A. Semiletov / Electron diffraction study of cuprous tellurides. Izv.Ak.Nauk SSSR,ser. Neorg.Mater., 1977, 13, p.2157.
3. Nowotny, H. Die Kristallstructur von Cu_2Te. Z..Metallforsc. 1946, p.37.
4. Bikkulova N.N., Yagafarova Z.A., Sultangareeva Z.S. et al. / Phase transitions in the non-stoichiometric $Cu_{2-\delta}Te$ compound.

Bulletin of Bashkir University., 2013, 18, 4, p.995.

5. Yagafarova A., Bikkulova N.N., Kurbangulov A.R./ Electrophysical properties and phase transitions in the superionic conductor of non-stoichiometric composition $Cu_{2-\delta}Te$. Phase transitions, interfaces and nanotechnology, 2015, 4, p.39.

6. Gasymov H.B., Rzayev R.M., Mamedov H.M. / Preparation and x-ray diffraction investigation of $Cu_{1.80-x}ZnTe$ (x= 0.025, 0.050, 0.07 5, 0.10) single crystals. Journal of Radiation Researches, 2018, 5, p.128.

7. Asadov Yu.G., Jafarov K.M.,Gasimov G.B., Babayev A.G. / Structural transformation of $Cu_{1.50}Zn_{0.30}Te$/Inorganic materials, 1993, 29, p.330.

8. Asadov Yu.G., Rustamova L.V. Jafarov K.M.,Gasimov G.B., Babayev A.G. / Structural phase transitions in Cu2-xTe crystals (x=0.00, 0.10, 0.15, 0.20, 025) Phase transitions, 1992, 38, p.247.

9. Tretyakov Yu.D., Putlyayev V.I. / Introduction to the chemistry of solid phase. M.Nauka (2006)

10. Borisov S.V., Magarill S.A., Pervukhina N.V. Crystallographic analysis of atomic structures-the development of "lattice" crystallography J.Crystallography, 2011, 56, p.1001.

INFLUENCE OF SIZE OF SMALL FERROELECTRIC BARIUM TITANATE PARTICLES ON DIELECTRIC PROPERTIES OF SMECTIC A LIQUID CRYSTAL WITH A POSITIVE DIELECTRIC ANISOTROPY

A.R. IMAMALIYEV[1], M.A. RAMAZANOV[2], Sh.A. HUMBATOV[2], G.M. BAYRAMOV[2], A.K. MAMMADOV[1]

[1]Azerbaijan National Academy of Science, Institute of Physics, AZ1143, Baku, Azerbaijan
[2]Baku State University, Department Chemical Physics of Nanomaterials, Faculty of Physics, AZ1148, Baku, Azerbaijan

Using low-frequency dielectric spectroscopy, the size effect of submicron barium titanate particles on the dielectric properties of smectic A liquid crystal with positive dielectric anisotropy is studied. It is shown that the addition of ferroelectric particles significantly increases only the longitudinal component of the dielectric constant. The larger the particle size, the larger this increase. Ferroelectric particles also affect the dielectric dispersion of the liquid crystal. The dispersion of the longitudinal component of the dielectric constant, is shifted towards high frequencies. The amount of displacement increases with increasing of particle size. An interpretation of the observed patterns based on existing models is given.

1. INTRODUCTION

In the past two decades, a lot of researches has been devoted to liquid crystal colloids [1-3]. Since the addition of submicron and nanoscale functional particles (ferromagnetic, ferroelectric particles, carbon nanotubes, metal nanoparticles etc.) to liquid crystals in small quantities can cause colossal changes in the properties of the latter, and in some cases lead to qualitatively new effects that are unusual for liquid crystals [4-8]. An example is an increase in the phase transition point upon the addition of carbon nanotubes [9], a decrease in the threshold of the Fredericks effect [10-12]. When particles of ferroelectric particles are added to a nematic LC, pseudo nematic domains arisein the isotropic phase, which allows realizing an electro-optical effect with memory [13]. To achieve the maximum result when using these changes for practical purposes, one should vary the types and parameters of both the liquid crystal and functional particles. For example, the use of a smectic A LCs as a matrix, the Fredericks effect occurs with memory. In addition, smectic-based colloids are significantly stable compared to nematics, due to its high translational viscosity. But, the threshold voltage of the Fredericks effect in smectic A LCs is at least an order of magnitude higher than in nematics. We have experimentally shown the possibility of significantly lowering the threshold of the Fredericks effect by adding small ferroelectric barium titanate (BaTiO$_3$) particles to smectic A LC [12]. A further lowering of the threshold requires investigating the effect of the size and concentration of these particles on the material parameters of smectic A LC.

In this work, the effect of the size of submicron particles of barium titanate (BaTiO$_3$) on the dielectric properties of smectic A liquid crystal with positive dielectric anisotropy has been studied.

2. EXPERIMENTAL

The smectic A LC is a mixture of p-nitrophenyl p-decyloxybenzoate

$$C_5H_{11} - \langle O \rangle - \langle O \rangle - C \equiv N$$

and 4-cyano-4′-pentylbiphenyl with a molar ratio of 1:1 (Scheme 1).

$$C_nH_{2n+1}O - \langle O \rangle - COO - \langle O \rangle - NO_2$$
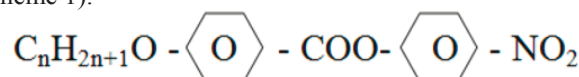
Scheme 1. Molecular structures of the liquid crystal molecules

The mixture is in the smectic A phase in the temperature range of 32.5–47.0 °C and has positive dielectric anisotropy.

BaTiO$_3$ is a ferroelectric material with high spontaneous polarization (0.26 C·m^{-2} at room temperature) [14,15]. The crystal lattice of BaTiO$_3$ has tetragonal structure. With a decreasing of particle size, the degree of tetragonality (the ratio c/a, where c is the height, and a is the side of the crystal lattice base)

19

and, accordingly, spontaneous polarization decreases. For particles with a size of the order of 100 nm, the crystal lattice transforms into a cubic one [16]. In the experiment, mono disperse $BaTiO_3$ particles with sizes of 100 nm, 200 nm, 300 nm, 400 nm, and 500 nm were used (US Research Nanomaterials).

The volume fraction of $BaTiO_3$ particles was 0.0017. Dispersion of $BaTO_3$ particles in a smectic A LC was carried out according to the following procedure. After weighing (balance ADAM PW-124), particles were added to LC, then the mixture was shaken for 40 min in Ultrasonic Cleaner (NATO CD-4800) at 75 °C (isotropic phase) with subsequent cooling to 36 °C (smectic A phase). The transition to the smectic A phase at 47 °C prevents the aggregation of particles. The cell temperature was controlled by a special oven equipped with a SYL-1512 / TC-K3 thermostat. The thermo stating accuracy was 0.1 °C.

The dielectric properties of the LC were measured at 36 °C in an electro-optical cell. The electro-optical cell with layered sandwiched structure consists of two parallel plate glasses separated by a 15 μm teflon spacer. The internal surfaces of glasses were covered by a transparent conductive ITO layer. To obtain a homeotropic orientation, the smectic A LC was subjected to periodic shear deformations. Oscillations of one substrate relative to another in the longitudinal direction for a minute led to a qualitative homeotropic orientation. Polyimide was used as a planar aligning material [17]. The process of filling of the electro-optical cell was carried out by a capillary method in the isotropic state of the LC.

The RLC meter IET-1920 allows to measure the electrical capacitance (C) and dissipation factor (D) of the LC cell in the frequency range from 20 Hz to 1 MHz. The amplitude of the AC test signal was 1 V.

The dielectric constant of the LC was determined by the expression $\varepsilon = \dfrac{C}{C_0}$, where C and C_0 are the capacities of the filled and empty cells, respectively. In the case of the homeotropic orientation of the LC, the longitudinal component of the dielectric permittivity ($\varepsilon_\parallel$) was measured, and in the case of the planar orientation of the LC, the transverse components of this quantity ($\varepsilon_\perp$) was measured. Real and imaginary parts of dielectric permitivity were determined by the formulae $\varepsilon' = \dfrac{\varepsilon}{\sqrt{1+D^2}}$ and $\varepsilon'' = \varepsilon' D$, respectively.

3. RESULTS AND DISCUSSION

Figures 1 and 2 show the frequency dependences of the real ($\varepsilon_\parallel'$) and imaginary ($\varepsilon_\parallel''$) parts of the longitudinal component of the dielectric constant of pure LC and colloids. The table 1 shows the values of these quantities at the frequency of 1 kHz.
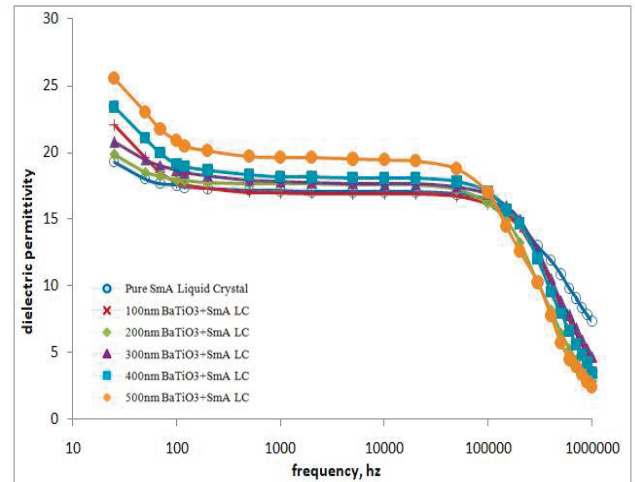
Figure 1. Frequency dependence of the real parts of the longitudinal dielectric permittivity components for pure smectic A liquid crystal and different sizes $BaTiO_3$ particles dispersed smectic A liquid crystal.

Figure 2. Frequency dependence of the imaginary parts of the longitudinal dielectric permittivity components for pure smectic A liquid crystal and different sizes $BaTiO_3$ particles dispersed smectic A liquid crystal.

Table 1. The values of real parts of the longitudinal dielectric permittivity components at the frequency of 1 kHz and relaxation frequency

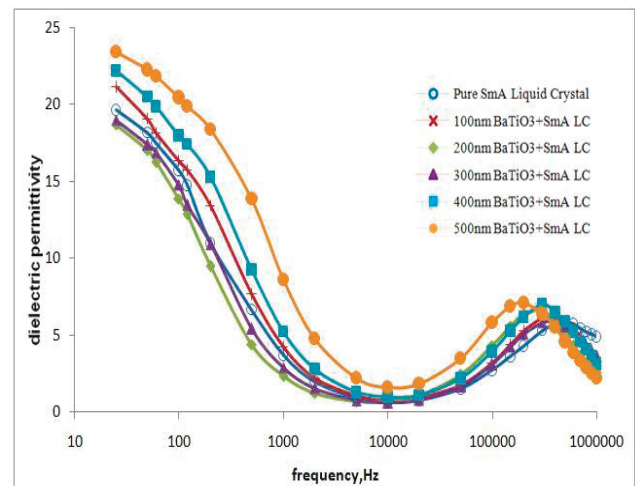| LC	SmA	SmA+BaTiO₃ (100 nm)	SmA+BaTiO₃	SmA+BaTiO₃ (300 nm)	SmA+BaTiO₃ (400 nm)	SmA+BaTiO₃ (500
$\varepsilon_{\parallel}'$	17.1	16.9	17.6	17.8	18.2	19.6
f_{rel}^{max}	500	400	350	300	300	250

As can be seen from the table, the addition of BaTiO₃ ferroelectric particles to the smectic A LC, the longitudinal component of the dielectric constant increases appreciably, and the larger the particle size, the greater the increase in the dielectric constant. The results of measurements show that the transverse component of the dielectric constant ($\varepsilon_{\perp}'$) remains almost unchanged (therefore, the corresponding graphs for $\varepsilon_{\perp}'$ are not given). At low concentrations of BaTiO₃ particles, the dielectric constant of the colloid in the linear approximation can be calculated

$$\varepsilon^{collid} = \varepsilon^{LC} + c \cdot \varepsilon^{FNP} \qquad (1)$$

ε^{LC} and ε^{FNP} are dielectric constants of liquid crystal and ferroelectric particles, respectively, c - volume fraction of ferroelectric particles. The fact that the addition of particles increases only the longitudinal component can be explained by the interaction of spontaneous polarization of BaTiO₃ particles with the LC director field [18]. In more detail, during the transition of the LC from the isotropic phase to the LC phase, the BaTiO₃ particles are oriented so that their polar axis (along which spontaneous polarization occurs) coincides with the direction of the predominant orientation of the LC molecules.
Substituting the value of dielectric constant in the direction of the polar axis $\varepsilon_c^{FNP} \propto 10^3$ [15] and $c \approx 2 \cdot 10^{-3}$ in formula (1), we obtain that the longitudinal component of the dielectric permittivity of the colloid corresponds to the values shown in table 1. With a decrease in the size of the ferroelectric particles, their dielectric constant in the direction of the polar axis decreases, which is reflected in the value of the dielectric constant of the colloid. In the case of the transverse component of dielectric permittivity, the increase is insignificant, since $\varepsilon_a^{FNP} \propto 10^2$.

The dispersion of the dielectric constant observed at high frequencies (fiq.2) is associated with the existence of strong longitudinal dipole groups –C≡N and –C-NO₂. When BaTiO₃ particles are added to the LC, the relaxation frequency shifts toward low frequency region. The amount of displacement increases with increasing of particle size (last row of Table 1). This result is explained by the existence of a local electric field around polarized BaTiO₃ particles. This field, interacting with dipole groups, makes difficult for molecules to rotate around his short axis.

4. CONCLUSION

The doping of smectic A liquid crystal with ferroelectric BaTiO₃ particles significantly increases only the longitudinal component of the dielectric constant. The larger the particle size, the larger this increase.

5. REFERENCES

1. Liquid Crystals with Nano and Microparticles (In 2 Volumes)edited by Jan P F Lagerwall and Giusy Scalia, Singapore, World Scientific, p. 920.
2. Stark H. / Physics of colloidal dispersions in nematic liquid crystals, Physics Reports, 2001, 351, p.387–474
3. Drzaic, Paul S. / Liquid Crystal Dispersions, World Scientific, Singapore, 1995, p. 429.
4. Reznikov Y., Glushchenko A., and Garbovskiy Y. / Ferromagnetic and ferroelectric nanoparticles in liquid crystals, Liquid Crystals with Nano and Microparticles (In 2 Volumes) edited by Jan P F Lagerwall and Giusy Scalia, p.637-693.
5. Garbovskiy Y. and Glushchenko A. / Ferroelectric Nanoparticles in Liquid Crystals: Recent Progress and Current Challenges, Nanomaterials 2017, 7, p.361-380.
6. Reznikov Y. Ferroelectric Colloids in Liquid Crystals, Liquid Crystals Beyond Displays: Chemistry, Physics, and Applications, Edited by Quan Li, John Wiley & Sons, Inc., Hoboken, New Jersey, 2012, p. 573.
7. Garbovskiy Y. and Glushchenko I. / Nano-Objects and Ions in Liquid Crystals: Ion Trapping Effect and Related Phenomena, Crystals, 2015, 5, p.501-533
8. Schymura S., Park J. H., Dierking I., and Scalia G. / Carbon nanotubes in thermotropic low molar mass liquid crystals, Liquid Crystals with Nano and Microparticles (In 2 Volumes) edited by Jan P. F. Lagerwall and Giusy Scalia, Singapore, World Scientific, p.603-630.

9. Duran H., Gazdecki B., Yamashita A. and Kyu T. / Effect of carbon nanotubes on phase transitions of nematic liquid crystals, Liquid Crystals, 32, 2005, p.815-821.

10. Lagerwall J., Scalia G. / A new era for liquid crystal research: Applications of liquid crystals in soft matter nano-, bio- and micro technology, Current Applied Physics, 2012, 12, p.1387-1412.

11. Ibragimov T. D., Imamaliyev A. R., Bayramov G. M. / Formation of local electric fields in the ferroelectric $BaTiO_3$ particles-liquid crystal colloids, Ferroelectrics, 2016, 495, p.60–68.

12. Imamaliyev A. R., Ramazanov M. A., and Humbatov S. A. / Effect of ferroelectric $BaTiO_3$ particles on the threshold voltage of a smectic A liquid crystal, Beilstein J. Nanotechnol. 2018, 9, p.824–828.

13. Rajratan Basu / Soft memory in a ferroelectric nanoparticle-doped liquid crystal, Physical Review E, 2014, 89, p. 022508

14. Vijatović M. M., Bobić J. D., Stojanović B. D. / History and Challenges of Barium Titanate: Part IScience of Sintering, 2008, 40, 155-165, p. 235-244.

15. Yu J., Chu J. / Nanocrystalline Barium Titanate, Encyclopedia of Nanoscience and Nanotechnology, Edited by H. S. Nalwa, 2004, 6, p. 389–416

16. Chao Fang, DongXiang Zhou, Shu Ping Gong / Core-shell structure and size effect in barium titanate nanoparticle, Physica B, 2011, 406, 1317–1322.

17. J.Cognard / Alignment of nematic liquid crystals and their mixtures, Gordon and Breach Science Publishers, 1982, p.77 .

18. Al-Zangana, S. Turner, Dierking M. / A comparison betwn size dependent paraelectric and ferroelectric $BaTiO_3$ nanoparticle doped nematic and ferroelectric liquid crystals, J. Appl. Phys. 2017, p.121-138.

INFLUENCE OF DOPING MATERIAL ON SECOND HARMONIC GENERATION in AgGaSe$_2$ CRYSTAL

Sh.A. SHAMILOVA

Baku State University

In present work, the results obtained for the conversion efficiency of AgGa$_{0.6}$In$_{0.4}$Se$_2$ crystal with analogous results for an AgGaSe$_2$ crystal with existing experimentally values are compared. The analytical used method allows calculating the optimal parameters of both the crystal and a source of radiation for conditions of noncritical phase matching in a particular experiment.

1. INTRODUCTION

Optical nonlinear infrared crystals (IR), such as ZnGeP$_2$, AgGaSe$_2$, AgGaS$_2$, GaSe [1-3] owing to their unique properties, have become of great interest in application of the middle and far infrared range. IR crystals have a large effective optical nonlinearity [4–9].

Recently the most important directions in the development of laser technology have been the creation and study of tunable sources of radiation having extremely short pulse durations and a wide spectrum of radiation. Such sources of the IR range are an irreplaceable instrument for studying semiconductor elements for optical communication systems, the basic components of a new generation of lidar-gas analyzers [10], scientific and medical devices. However, for the implementation of these tasks, coherent radiation sources with the necessary energy parameters and efficiency are necessary.

To solve the mentioned problems of modern nonlinear optics, the search for promising materials continues. The disadvantages of the used crystals, for example for a CdGeAs$_2$ crystal operating at cryogenic temperatures are high losses at the second harmonic generation, Te and ZnGeP$_2$ at the wavelengths of the fundamental radiation of the CO$_2$ laser. Tl$_3$AsSe$_3$ and AgGaSe$_2$ crystals have poor thermal properties, while GaSe crystals have low mechanical properties. Hence, in particular, the problems of creating efficient and reliable harmonic generators of CO$_2$ lasers arise. There are a number of difficulties in creating optical parametric generators (OPG) as well as.

Thus, the main restrictive factor in the development of a number of perspective parametric frequency converters (PPC) is the absence of nonlinear crystals that are transparent in the visible, near and mid-IR range, and at the same time possess a number of physical properties: first of all, high nonlinear properties, radiation resistance sufficient the fulfill of phase-matching conditions by birefringence, good mechanical properties and high thermal conductivity. The complication of the composition of crystals allows varying their physical properties in wide range and as a result to satisfy the requirements for the elemental base of nonlinear optics. All of the above stimulated the search and study of new nonlinear materials among ternary and mixed compounds most suitable for solving the above problems.

For applications in the IR spectral range, the leading role is played by CO$_2$ lasers, which represent a powerful source of optical coherent radiation in this region of the spectrum. If in the mid-IR range of the spectrum the efficient generation of radiation this laser allows to realize tunable coherent radiation, then this can be achieved in the near-IR range due to the second harmonic of the CO$_2$ laser.

As an object of study among mixed-type crystals, we have chosen the perspective AgGa$_x$In$_{1-x}$Se$_2$ crystal, due to several advantages. As the studies showed in [14], by selecting indium content, the condition of non critical 90^0 phase matching can be performed when the second harmonic is generated in the near and middle IR ranges. The value of the parameter x at the wavelength of the CO$_2$ laser radiation λ = 9.64 μm is 0.6. The measured value of the quadratic nonlinear susceptibility for

$AgGa_{0.6}In_{0.4}Se_2$ crystal is $d_{36} = 41$ pm/V [14]. For comparison, the value for the $AgGaSe_2$ crystal is 39 pm/V [13, 14].

To consider a wide range of tasks in the theory of nonlinear waves, it is necessary to solve a system of coupled nonlinear differential equations, the so-called reduced equations. Various approximate methods were used to analyze these equations. Among them, the constant-field approximation of the fundamental radiation is widespread [15-17]. The constant-field approximation correctly describes only the initial stage of nonlinear interaction of waves; so far we can ignore the inverse effect of generated or amplified waves on the pump wave. This leads to a restricted consideration interaction of waves in real media, to the loss of information about the features of the nonlinear process.

To study the nonlinear optical properties of the selected type of crystal, it is expedient to resort to the constant-intensity approximation [18, 19], which allows to take into account the inverse effect of the excited wave on the exciting one. This approximation made it possible to consider the effect of phase effects on the process of doubling the frequency of the CO_2 laser radiation in these mixed-type crystals.

The results of studies of the influence of various parameters on the conversion efficiency in an $AgGa_{0.6}In_{0.4}Se_2$ crystal under the conditions of existing experiments are presented in [8]. The angular dispersion coefficients are calculated for three types of $AgGa_xIn_{1-x}Se_2$ crystals differing by indium content. The ways of increasing conversion efficiency are shown.

In this work, we compare the results obtained for the conversion efficiency of an $AgGa_{0.6}In_{0.4}Se_2$ crystal with similar results for an $AgGaSe_2$ crystal with existing experimentally measured values. The analytical used method allows us to calculate the optimal parameters of both the crystal-converter and the radiation source for conditions of noncritical phase matching in a particular experiment. For example, the crystal length at given losses and the pump intensity, which allows us to estimate the expected conversion efficiency. It is shown that the transfer of radiation energy from the fundamental wave to the second harmonic wave in the case of the $AgGa_{0.6}In_{0.4}Se_2$ crystal occurs at a shorter length than for the $AgGaSe_2$ crystal. It was also revealed that the laser radiation intensity for the maximum value of the conversion efficiency in the $AgGa_{0.6}In_{0.4}Se_2$ crystal is small compared to the $AgGaSe_2$ crystal.

2. THEORY

Let us analyze the process of doubling the frequency of the CO_2 laser radiation (at a frequency ω_1) in a negative uniaxial $AgGa_xIn_{1-x}Se_2$ crystal in the case of $oo \rightarrow e$ scalar phase matching for the first type.

For nonlinear conversion, a theoretical analysis of the interaction of waves is carried out using the known system of reduced equations describing the second harmonic generation (at a frequency of $2\omega_1$), [8, 15-17]

$$\frac{dA_1}{dz} + \delta_1 A_1 = -i \frac{8\pi^2 d_{1eff}}{\lambda_1 n(\omega)} A_2 A_1^* \exp(-i\Delta z),$$

$$\frac{dA_2}{dz} + \delta_2 A_2 = -i \frac{4\pi^2 d_{2eff}}{\lambda_2 n(\omega)} A_1^2 \exp(i\Delta z), \quad (1)$$

where A_1, A_2 are complex amplitudes of pump wave and its second harmonic at frequencies $\omega_{1,2}$ ($\omega_2 = 2\omega_1$) correspondingly, k_1, k_2 are values of wave vectors for pump and second harmonic waves, $\Delta = k_2 - k_1$ stands for phase mismatch, d_{1eff} are efficient nonlinear coefficient for the case $oo \rightarrow e$ scalar phase matching, $\lambda_{1,2}$ signify the wavelength of pump and second harmonic waves, $n(\omega_{1,2})$ are the indices of crystal refraction, $\delta_{1,2}$ are the coefficients of absorption for waves at frequencies of respectively $\omega_{1,2}$.

We'll solve the system with the following boundary conditions

$$A_1(z=0) = A_{10} \exp(i\varphi_{10}), \quad A_2(z=0) = 0, \quad (2)$$

where z=0 corresponds to the entry to the crystal, and is the initial phase of the pump wave at the entry to the medium.

The solution (1) in the constant-intensity approximation relative to the amplitude of the second harmonic, taking into account the boundary conditions (2) at the exit from the crystal ( ), has the following form [4-9,18,19]

$$A_2(\ell) = -i\gamma_2 A_{10}^2 \ell \, \text{sinc}\lambda\ell \exp\left[2i\varphi_{10} - (\delta_2 + 2\delta_1 - i\Delta_1)\ell/2\right], \quad (3)$$

Where

$$\lambda^2 = 2\Gamma^2 - (\delta_2 - 2\delta_1 + i\Delta_1)^2/4, \quad \Gamma^2 = \gamma_1\gamma_2 I_{10},$$

$$\sin cx = \sin x/x, \quad I_j = A_j A_j^*,$$

and

$$\gamma_1 = \frac{\pi^2 d_{1eff}}{\lambda_1 \, (\omega_1)}, \quad \gamma_2 = \frac{4\,^2 d_{2eff}}{\lambda_2 n(\omega_2)}$$

are nonlinear coefficients of waves.

It can be seen from (3) that the harmonic amplitude, depending on the length of the crystal, is a periodic function. At first, at a distance of the optimal length (coherent length), the energy of the fundamental radiation is pumped into the energy of the second harmonic. Then there is a reverse transfer of energy. From (3) at $\delta_2 = 2\delta_1$ it is possible to receive optimum length of crystal. At this length in the process of frequency conversion, a harmonic signal is maximum $\ell_{opt} = \lambda^{-1}\arctan(\lambda/\delta_2)$, where $\lambda^2 = 2\Gamma^2 + \Delta^2/4$. Whence it appears that in this case, in contrast to the results of the constant-field approximation, a coherent length of nonlinear medium depends on pump intensity I_{10} and dissipation in a medium. By increasing in pump intensity and mismatch, the optimum length decreases. When we ignore the losses $\ell_{opt} = 0.5\pi/(2\Gamma^2 + \Delta^2/4)^{1/2}$ [18, 19].

At $\gamma_1 = 0$ and $\delta_i = 0$ from (3) we have an expression for conversion efficiency in the constant-field approximation.

From (3) it is possible to obtain the analytical expression for conversion efficiency of pump radiation to second harmonic $\eta_2(\ell) = I_2(\ell)/I_{10}$.

$$\eta_2(\ell) = \gamma_2^2 I_{10} \ell^2 \mathrm{sinc}^2 \lambda\ell \exp\left[-(\delta_2 + 2\delta_1)\ell\right] \quad (4)$$

An important requirement for the effective proceeding of nonlinear optical processes is the need to fulfill the optimal phase relationship between the interacting waves. Violation of this condition leads to a mismatch of the waves phase and, as a consequence, to a decrease in the efficiency of frequency conversion. One of the main reasons for violating the conditions of the optimal phase relation is phase mismatch. At frequency conversion in the conditions of phase mismatch, it is impossible to fulfill the complete transfer of basic radiation energy to second harmonic energy. In this case the spatial beatings of harmonic amplitudes are observed. This time, the minimums of harmonic intensity beatings, as an analysis shows in the constant-intensity approximation, depend on nonlinear susceptibilities of crystal [18]. This fact permits to define the nonlinear susceptibilities of substances by a simple way, more precise than in the constant-field approximation. With an increase in phase mismatch, spatial frequency increases, but at this time, maximum value of second harmonic intensity decreases.

In the experiment, for real frequency converters, it is not possible to precisely ensure the phase matching condition, i.e. synchronism ($\Delta = 0$). The error in ensuring the condition of synchronism determines the width of synchronism. The contribution to the wave mismatching is provided by the spectral width of the pump radiation, the deviation from the phase-matching angle due to the divergence of the laser radiation, and the instability of the temperature of the crystal converter. From here, obtaining information, in particular, about the angular width of phase matching allows us to calculate the maximum divergence of the pump light beam. Also, the determination of the conditions for realizing of noncritical phase matching at the selected pump wavelength is important in order to exclude of taking down the influence of birefringence on the generation efficiency. This fact allows to remove the restriction on the length of the used crystals [4–9, 11, 14, 19].

Table

Crystal	n_o^ω	n_e^ω	$n_o^{2\omega}$	$n_e^{2\omega}$	d_{36}, pm/V	Phase matching type	ϑ_s, degree	Angular dispersion coefficient of first order, cm^{-1} ang.min.$^{-5}$
AgGaSe$_2$	2.596208 2.596 [11]	2.56316	2.615267	2.58270 1 2.583[у]	39.0 [19]	oo → e	49.6679	0.046432
AgGa$_{0.7}$In$_{0.3}$Se$_2$	2.605264	2.58283 2	2.62348 9	2.60188	40.6 [11]	oo → e	66.0 [11]	0.023831

Crystal	n_o^ω	n_e^ω	$n_o^{2\omega}$	$n_e^{2\omega}$	d_{36}, pm/V	Phase matching type	ϑ_s, degree	Angular dispersion coefficient of first order, cm^{-1} ang.min.$^{-5}$
AgGa$_{0.6}$In$_{0.4}$Se$_2$	2,608277 2,6081[11]	2,589438	2,626222	2,608315	41,00 [20]	oo → e	90,0 [11]	0,0000194

Let's determine the angular width of phase matching in a negative uniaxial mixed-type AgGa$_{1-x}$In$_x$Se$_2$ crystal in the case of SHG from a CO$_2$ laser

at a pump wavelength of 9.64 μm, for three values reflecting the indium content in the crystal (0, 0.3, and 0.4). In this case, the Sellmeier coefficients given in [4–9, 11, 17] are used.

3. The calculation results for the angular dispersion coefficient of the first and second orders are presented in the table. [8] provides more detailed information for $AgGa_xIn_{1-x}Se_2$ (1-x = 0, 0.3, 0.4) at three wavelengths.

3. RESULTS AND DISCUSSION

To study ways to increase the frequency conversion efficiency in an $AgGa_{1-x}In_xSe_2$ crystal of CO_2 laser in the IR range, we'll make the numerous calculation of the analytical expression for the conversion efficiency (4) obtained in the constant-intensity approximation. Moreover, the parameters of the task are selected according to the conditions of existing experiments for a given crystal [11, 21]. In Fig. 1-3 shows the dynamic process of frequency conversion to the second harmonic in $AgGa_{1-x}In_xSe_2$ and $AgGaSe_2$ crystals.

In Fig. 1 shows the dependences of the frequency conversion efficiency on the crystal of length $\eta_2(l)$. Frequency conversions for two crystals are considered with a pump intensity $I_{10} = 1.25$ MW/cm^2 of CO_2 laser emitting at a wavelength of 9.64 μm. From the behavior of the curves that differ from the monotonic behavior in the case of constant-field approximation follows that there is an optimal value of the crystal length at which the conversion efficiency is maximum. As can be seen, the transfer of radiation energy from the fundamental wave to the second harmonic wave in the case of the $AgGa_{0.6}In_{0.4}Se_2$ crystal occurs at a shorter length than for the $AgGaSe_2$ crystal.
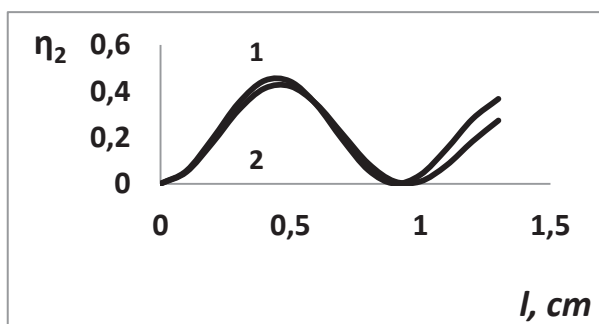
Figure 1. Dependences of conversion efficiency of radiation energy of pump wave (λ=9.64 mcm) to energy of wave of second harmonic η_2 on lengths of $AgGa_{0.6}In_{0.4}Se_2$ (1) crystal l calculated in the constant-intensity approximation for δ_1=0.06 cm^{-1}, δ_2=0.08 cm^{-1} [11] and $AgGaSe_2$ (2) δ_1=0.09 cm^{-1}, δ_2=0.15 cm^{-1} Δ=0.06 cm^{-1} at pump intensity of I_{10}= 1.25 MW/cm^2.

In Fig. 2 shows the dependences of $\eta_2(l)$ on the pump intensity. As can be seen from the figure, the radiation of a CO_2 laser generating at a wavelength of 9.64 μm is most effectively converted to a second harmonic wave at the optimal value of the pump intensity.

As is known, in mixed $AgGa_xIn_{1-x}Se_2$ structures, the indium content affects on the crystal properties [4,8].
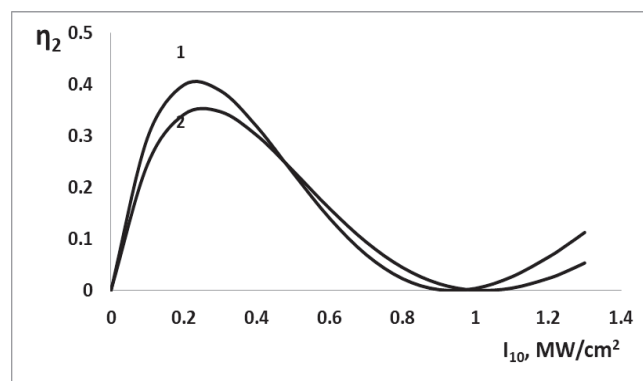
Figure 2. Dependences of conversion efficiency of radiation energy of pump wave (λ=9.64 mcm) to energy of wave of second harmonic as a function of the pump intensity calculated in the constant-intensity approximation for $AgGa_{0.6}In_{0.4}Se_2$ (1) δ_1=0.06 cm^{-1}, δ_2=0.08 cm^{-1} [11] and $AgGaSe_2$ (2) δ_1=0.09 cm^{-1}, δ_2=0.15 cm^{-1}, Δ=0.06 cm^{-1} at crystal length of l= 1.05 cm [11]

In Fig. 3 shows the results of the analysis in the constant-intensity approximation of the frequency conversion process for three different concentrations of indium in the crystal: 0, 0.3, and 0.4, the pump wavelength of the CO_2 laser is 9.64 μm.
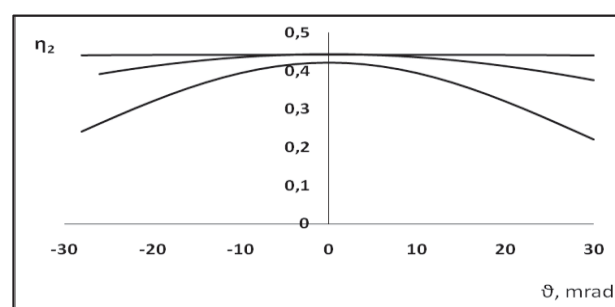
Figure 3. Dependences of conversion efficiency of radiation energy of pump wave to energy of wave of second harmonic in $AgGa_xIn_{1-x}Se_2$ crystal η_2 as a function of the phase mismatch calculated in the constant-intensity approximation at pump intensity of I_{10}= 0.25 MW/cm^2 for $AgGaSe_2$ (1) δ_1=0.09 cm^{-1}, δ_2=0.15 cm^{-1} [11], $AgGa_{0.7}In_{0.3}Se_2$ (2) and $AgGa_{0.6}In_{0.4}Se_2$ (3). For $AgGa_xIn_{1-x}Se_2$ δ_1=0.06 cm^{-1}, δ_2=0.08 cm^{-1} [11], Δ=0.06 cm^{-1} at a crystal length l = 0.5 cm.

A similar behavior was observed in [8]. A comparison of the behavior of the group of curves

1–3 shows that with an increase in the indium concentration in the mixed crystal from 0 to 0.4, the dependence η_2 (ϑ) becomes more flat. This indicates a transition to the regime of uncriticality of the crystal to fulfill the condition of phase matching. For example, in an $AgGaSe_2$ crystal, a change in the conversion efficiency by 0.032633% occurs in the angular range of values from - 0.7 mrad to + 0.7 mrad. Substitution of a part of Ga in the crystal for indium to the content x = 0.7 ($AgGa_{0.7}In_{0.3}Se_2$) leads to a similar change in efficiency, but already in the angular interval greater than 1.92 times (from -1.35 mrad to +1.35 mrad). Further introduction of indium into the crystal to x = 0.6 ($AgGa_{0.6}In_{0.4}Se_2$) increases the angular interval by 31.14 times (-21.8 mrad +21.8 mrad) compared with the case of the $AgGaSe_2$ crystal. Hence, in $AgGa_{0.6}In_{0.4}Se_2$ crystals, the noncriticality of the phase matching condition is fulfilled in a larger angular range than in $AgGa_{0.7}In_{0.3}Se_2$, and even more so in $AgGaSe_2$.

Also from figure 3 shows that under the conditions of a real experiment, the maximum conversion efficiency expected in the case of an $AgGa_{0.6}In_{0.4}Se_2$ crystal is 1.05 times higher than the conversion efficiency in an $AgGaSe_2$ crystal.

Thus, a theoretical study of the frequency conversion in mixed crystals taking into account phase effects allows to identify ways to improve the conversion efficiency. Namely, for given values of the length of crystal converter, it is possible to calculate the optimal value of the pump intensity, which in the case of the $AgGa_{0.6}In_{0.4}Se_2$ crystal is less than for $AgGaSe_2$, and also for the selected pump intensity of the laser calculate the coherent length of the crystal-converter. It is shown that the transfer of radiation energy from the fundamental wave to the second harmonic wave in the case of the $AgGa_{0.6}In_{0.4}Se_2$ crystal occurs at a shorter length than for the $AgGaSe_2$ crystal. In $AgGa_{0.6}In_{0.4}Se_2$ crystal non-criticality of the phase-matching condition is fulfilled in a larger angular range (31.14 times) than in $AgGaSe_2$. The analytical method also allows to evaluate the expected conversion efficiency at different wavelengths of laser radiation.

4. CONCLUSION

As a result of the analytical calculations, it can be argued that $AgGa_{0.6}In_{0.4}Se_2$ type crystal is more suitable for developing reliable high-efficiency second-harmonic generators of a CO_2 laser than $AgGaSe_2$ crystal.

5. REFERENCES

1. Das S. / Kvantovaya elektronika. 2012, 42, p.228-230.
2. Qeyko P.P. / Optika atmosferi i okeana, 2003, 16, p.9.
3. Schunemann P.G.,Setzler S.D., Pollak T.M. / J. Cryst. Growth, 2000, 211 (1-4), p.257.
4. Shamilova Sh.A., Kasumova R.J. Materials digest of the X International Scientific and Prac. Conf. "Trends of modern science 2014", Sheffield, 2014 , v.23, p.58-60.
5. Shamilova Sh.A., Kasumova R.J. / International J. Of Scientific & Technology Research, (189-192) 2014, 3, p.6.
6. Kasumova R.J., Shamilova Sh.A., Safarova G.A., L.S. Gadyieva. / International J. of Engineering and Sciences, IJET-IJENS' , 2015, 15, is. 02.
7. Kasumova R.J., Mamedov H.M., Shamilova Sh.A., Mamedova V.C. Materials of 8th International Scientific Conference «Science and Society» (SCIEURO-ISPC), UK, London, 2015, 24-29 November, p.43-46.
8. Kasumova R.J. / An Indian J: Material Science, 2014, 10(8), p.306-311.
9. Kasumova R.J. Materialy IX Miedzynarodowejnaukowi-konferencji "Europejskanauka XXI-2013" Matematyka, Fizyka, Budownictwo i archi-tektura, Przemysl, Nauka I studia, 2013, 27, p.41-44.
10. Kasumova R.J. Proceeding of Asia Pacific Conference on fundamental prob. Of Opto- and microelectronics and international Work Shop on optical beam transformation Vladivostok, Russia 2001, p.65-68.
11. Andreev Yu.M., Baturin I.S., Qeyko P.P., Qusamov A.I. / Kvantovaya elektronika, 1999, 29 (1), p.66-70.
12. Blombergen N. / Nonlinear Optics, W.A. Benjamin, New York, 1965.
13. Akhmanov S.A., Khokhlov R.V. / Problemy Nelineynoy Optiki [The Problems of Nonlinear Optics] Moscow, VINITI, 1964.
14. Dmitriev V.G. and Tarasov L.V. / Prikladnaya Nelineynaya Optika [Applied Nonlinear Optics] Moscow, Radio I Svyaz, 1982.
15. Tagiev Z.H., and Chirkin A.S., Zh. / Eksp. Teor. Fiz.,73, 1977, p.1271-1282 [Sov. Phys. JETP, 46 p.669-680].
16. Tagiev Z.H., Kasumova R.J., Salmanova R.A., Kerimova N.V. / J. Opt. B: Quantum Semiclas. Opt. 2001, 3, p.84-87.
17. Bhar G.C. / Appl Opt, 1976, v 15, No.2, p.305-307.

18. Tagiyev Z.A., Kasumova R.J. / Optika i spektros. 1996, .80, 6, p. 941-943.
19. Schunemann P.G., Zweiback I., Pollak T.M. Intern. Conf. on Ternary and Multinary Compounds (Salford, UK, 1997).
20. Spravochnik po lazeram pod red. Prokhorova A.M. (Handbook on Lasers), Moscow, 1978.
21. Qeyko P.P., Qusamov A.I., Andreev Yu.M. / Optika atmosferi i okeana, 1999, 2, 7, p.606-610.

DETERMINATION OF CONFORMATION AND DIMENSIONS OF POLYETHYLENE GLYCOL MACROMOLECULE IN THE SYSTEMS WATER-POLYETHYLENE GLYCOL-KOH BY VISCOSIMETER METHOD

B.G. PASHAYEV

Baku State Universitety, Department of Physics

Here, the kinematic viscosity of water-polyethylene glycol-KOH systems at temperature 293.15 K and 0-0.05 molar part of KOH, and at a concentration range of 0-5 g/dl of polyethylene glycol was investigated, polyethylene glycol molecules with a molecular weight of 1000, 1500, 3000, 4000 and 6000 were taken. Based on the experimental estimates of the kinematic viscosity,at the studied range of concentration interval intrinsic viscosity of studied solution, Haggins constant, the α parameter included in the Mark-Kuhn-Houwink formula, swelling coefficient of polyethylglycol macromolecule, intrinsic viscosity of the θ-solvent, root-mean-square distance between the ends of the polyethylene glycol chain θ-solvent and in the solution, the length of the Kuhn segment of θ-solvent and in the solution was calculated. Polyethylene glycol in macromolecules was found to be in a water-KOH medium in the form of a coil that can penetrate the surrounding fluid and as the concentration of KOH increases, the volume of this coil decreases and their urgency increases.

1. INTRODUCTION

The structural characteristics of the polymer solutions are mainly described by the conformation, dimensions, hydration of the polymer macromolecule and so on. Conformation and sizes of macromolecules in solution depend on the properties of the solvent and temperature the polymer and etc. in three-component systems, it also depends on the type and concentration of the other component. Since all biological processes occur in water, studying the conformation and sizes of macromolecules of biologically important polymers in the water environment is an interesting and important issue. One of such polymers is polyethylene glycol (PEG). Because PEG does not have a bad effect on the body's immune system, because they do not have toxic properties, and because of the rapid cleansing of the body and because of the rapid cleansing of the body it is widely used in medicine, pharmacology, food industry, etc [1, 2]. When PEG is soluble in water, due to the interaction between PEG macromolecules and water molecules, both the structure of water, size and conformation of macromolecule change. There is sufficient work in the literature to study the aqueous solution of different fraction of PEG [3-12]. However, the effects of small-molecule compounds on the conformation and size of the PEG macromolecule are very limited.

The purpose of this study is to determine of conformation and to evaluate their size of PEG macromolecules in water-PEG-KOH systems, also to investigate the effects of KOH on the macromolecular conformation and size.

2. THEORETICAL PART

According to modern concepts, in polymeric solutions linear dimensional macromolecule is converted into coil. As a result of macromolecular progression and rotation during flow friction occurs between the solvent molecules, and this leads to an increase in the viscosity. As a result of the linear and rotation of movement of the macromolecule during the flow, friction between the molecules of the solvent and the molecule is formed, which leads to increased viscosity. The rotational motion of individual macromolecules results in the intrinsic viscosity, which in turn determines the loss of energy during a flow [12, 13]. Determining the value of intrinsic viscosity allows us to estimate certain parameters of a solution (e.g., the conformation and size of macromolecules). Reduced viscosity (η_g) is first found to determine the characteristic viscosity [12, 13]:

$$\eta_g = \frac{\nu_m - \nu_h}{\nu_h c} \qquad (1)$$

Where ν_m and ν_h are the kinematic viscosities of solutions and solvents, respectively; c-is the concentration of polymer the solution. The reduced viscosity is described by the Huggins equation:

$$\eta_g = [\eta] + K_H[\eta]^2 c \qquad (2)$$

Where $[\eta] = \lim\limits_{c \to 0}(\eta_g)$ is the characteristic viscosity; K_H-is the Huggins constant, which characterizes the intensity of interaction between particles in system [12-15]. The characteristic viscosity and the Huggins constant are determined from dependence $\eta_g \sim c$ using.

It is known that the characteristic viscosity of polymer solutions correlates with the molecular weight of the polymer and is described by the Kuhn-Mark-Houwink equation [12-15].

$$[\eta] = KM^\alpha \qquad (3)$$

Where K-is a constant that depends on the properties of the dissolved substance and the solvent; α-is parameter that characterizes the conformation of macromolecules in the solution. (3) if we take a logarithm on each side of the expression

$$\ln[\eta] = \ln K + \alpha \ln M \qquad (4)$$

$\ln[\eta] \sim \ln M$ is depending on the dependency, α parameter is obtained graphically.

The value of intrinsic viscosity in θ-solvent is used to estimate the size of the polymer macromolecule in equilibrium. Note that θ-solvent is called such a solvent formed during the polymer solubility in that solvent all possible interactions in the solution compensate each other. Thermodynamic equilibrium occurs in θ-solvent, and the polymer molecule is not excited. Of course, to get such a solution in practice it is very difficult to choose the necessary conditions (pressure, temperature, etc.). Theories are built on θ-solvent [13-15]. One such theory is Flory theory [15]. In the Flory theory, the intrinsic viscosity ($[\eta]_\theta$) of a polymer solution in a θ-solvent is determined by the equation:

$$[\eta]_\theta = K_\theta M^{1/2} \qquad (5)$$

Here is K_θ-θ constant, M-is molecular mass of polymer. As we can see from equation (5), we must find K_θ for find $[\eta]_\theta$. We note that because is not θ-solvent, it is not possible to determine $[\eta]_\theta$ on the basis of experimental estimates. However, it is possible to find K_θ by determining the intrinsic viscosity in a good solvent based on the experimental values. In a good solvent, there is a large number of expressions found for the viscosity dimensions which characterize between the intrinsic viscosity $[\eta]$ and K_θ [13-15]. For example, the connection between $[\eta]$ and K_θ is like that in Stockmayer-Fixman equation [16]:

$$\frac{[\eta]}{\sqrt{M}} = K_\theta + 0{,}51 B\Phi\sqrt{M} \qquad (6)$$

where B-is a long-range interaction parameter expressed in liters. Equation (6) is used after measuring intrinsic viscosity $[\eta]$ and dependence $\frac{[\eta]}{\sqrt{M}} = f(\sqrt{M})$ is extrapolated. From the extrapolation of the straight line obtained from $\sqrt{M} \to 0$, we get K_θ. Given the value of K_θ, $[\eta]_\theta$ is calculated according to the formula (5).

Polymer coil sizes are usually characterized by the root-mean-square distance between the ends of the macromolecule chain. We can find the root-mean-square distance between the ends of the macromolecule chain from the Flory-Fox equation in the optional solvent ($\langle h \rangle$) and θ-solvent ($\langle h_\theta \rangle$) [12, 15]:

$$[\eta] = \Phi\frac{\langle h \rangle^3}{M}, \quad [\eta]_\theta = \Phi\frac{\langle h_\theta \rangle^3}{M} \qquad (7)$$

where Φ is the Flory coefficient. Flory has experimentally found that it has an $\Phi = 2{,}1 \cdot 10^{23} mol^{-1}$ value [17]. Polymer coil sizes can also be characterized by hydrodynamic radius (R_h- radius that cannot absorb soluble molecules) and mid-square inertial radius (R_g). In arbitrary solvent (R_h, R_g) and θ-solvent ($R_{h\theta}$, $R_{g\theta}$) the hydrodynamic radius and the root-mean-square inertial radius can be calculated according to the following expressions, respectively [17]:

$$R_h = \left(\frac{3M[\eta]}{10\pi N_A}\right)^{1/3}, \quad R_{h\theta} = \left(\frac{3M[\eta]_\theta}{10\pi N_A}\right)^{1/3},$$

$$R_g = \frac{\langle h \rangle}{\sqrt{6}}, \quad R_{g\theta} = \frac{\langle h_\theta \rangle}{\sqrt{6}} \qquad (8)$$

Conformation of macromolecules in solution is also characterized by parameters such as the coefficient of swelling (β) and the length of the Kuhn segment (A). Polymer macromolecule is

infused β times in a good solvent. Swelling coefficient

$$\beta = \left(\frac{[\eta]}{[\eta]_\theta}\right)^{1/3} = \frac{\langle h \rangle}{\langle h_\theta \rangle} \qquad (9)$$

can be determined by this expression [13-15]. Macromolecular flexibility is determined by the length of the Kuhn segment. The length of the Kuhn segment in the arbitrary solvent (A) and θ-solvent (A_θ) is respectively

$$A = \frac{\langle h \rangle^2}{L} = \frac{\langle h \rangle^2}{nl_0}, \quad A_\theta = \frac{\langle h_\theta \rangle^2}{L} = \frac{\langle h_\theta \rangle^2}{nl_0} \qquad (10)$$

are defined by this expression [13-15]. Where L is the length of a completely unfolded macromolecule; n is the degree of macromolecule polymerization or the number of recurring number of ring; and l_0 is the recurring contour length of the monomer. [6] in the PEG macromolecule it is shown that the length of the contour of the recurring $-CH_2-CH_2-O-$ ring is $l_0 = 2,36\ \text{Å}$.

3. EXPERIMENTAL PART

In this work, we studied the kinematic viscosity of water-polyethylene glycol-KOH systems at temperature 293.15 K and 0-0.05 molar part of KOH, and at a concentration range of 0-5 g/dl of polyethylene glycol was investigated, polyethylene glycol molecules with a molecular weight of 1000, 1500, 3000, 4000 and 6000 were taken.

The KOH and PEGs were of chemically pure, and the solutions were prepared using bidistilled water. Viscosity was measured with a viscometer. The accuracy of determining the duration of a liquid flow was $\pm 0,01\ san$.

4. RESULTS AND DISCUSSION

Based on the experimental values of the kinematic viscosity, for the given molecular mass PEGs examined by the expression (1), the reduced viscosity of the aqueous solutions at the concentration range and temperature of 293.15 K were determined. Note that, the kinematic viscosity of all the aqueous solutions studied range of the KOH concentration (x) increases with increasing x. Based on the estimates of the reduced viscosity, included in expression (2) the concentrations of KOH and at a temperature of 293.15 K of aqueous solutions corresponding to different molecular mass PEGs intrinsic viscosity ($[\eta]$) and the Haggins constant (K_H) were calculated (Table 1).

Table 1. Dependence of intrinsic viscosity ($[\eta]$, dl/q) and Haggins constant (K_H) for different molecular weight of PEGs on concentration of KOH (x) in water-PEG-KOH systems(T=293,15 K).

x	PEQ-1000	PEQ-1500	PEQ-3000	PEQ-4000	PEQ-6000
			$[\eta]$, dl/q		
0	0,0341	0,0471	0,0675	0,0837	0,1343
0,01	0,0325	0,0457	0,0670	0,0810	0,1252
0,02	0,0320	0,0450	0,0648	0,0807	0,1182
0,03	0,0323	0,0447	0,0639	0,0783	0,1213
0,04	0,0317	0,0438	0,0621	0,0783	0,1138
0,05	0,0303	0,0436	0,0622	0,0765	0,1107
			K_H		
0	5,269	3,627	1,998	1,431	1,117
0,01	6,028	3,818	1,941	1,509	1,161
0,02	6,243	3,880	2,102	1,477	1,233
0,03	5,747	3,848	2,138	1,615	1,145
0,04	5,753	3,936	2,287	1,533	1,192
0,05	5,722	3,838	2,147	1,585	1,224

As can be seen from Table 1, the value of the intrinsic viscosity increases with the increase in the molecular weight of the PEG and decreases with the increase in the concentration of KOH. Intrinsic viscosity of the solution it is an additional viscosity resulting from rotation of polymer molecules in the soluble environment [12-15]. (7) and (8)

show that the intrinsic viscosity is directly proportional to the size of the macromolecule ($[\eta] \sim R_h^3$, $[\eta] \sim R_g^3$). Increase in the size of the PEG macromolecule with increasing molecular weight, it also becomes more difficult to rotate in the environment due to its greater interaction with water molecules (by hydrogen bonding), thus increasing the intrinsic viscosity. Suppose that the taken molecular mass for PEG decrease in intrinsic viscosity dependence on the concentration of KOH as a result with increased concentration caused by a decrease in macromolecule volume the PEG macromolecule. Thus, despite the increased viscosity of the solution with increasing concentrations of KOH, although the PEG macromolecule size decreases, as a result, macromolecules are easier to rotate in the environment. The dependence of the intrinsic viscosity on the concentration of KOH indicates that as the concentration increases, the conformation and dimensions of the PEG macromolecule change.

As can be seen from Table 1, the value of the Haggins constant in the studied solutions decreases with the increase in the molar mass of PEG, increasing with the increase in KOH concentration. Haggins constant characterizes the intensity of interaction of particles in the system [12]. So the worse the solvent for a given polymer, the Haggins constant value will be higher. The decrease in the Haggins constant value with increasing molecular weight at the given temperature indicates that the water-KOH system is a better solvent for a relatively large molecular mass PEG. That is, the solubility of PEG in water is getting better with increasing molecular mass. This can be explained by the hydration of the PEG macromolecule formed by the interaction of water and PEG molecules. Apparently, as the molecular mass increases, the number of water molecules accumulated around the PEG macromolecule also increases, resulting in a decrease in the Haggins constant value. The increasing value of Haggins with increasing concentrations of KOH for given molecular mass PEG indicates that with increasing concentration, the solubility of PEP in water is getting worse. This is probably due to the hydration of K^+ and OH^- ions in the solution. Thus, in water-PEG systems, only PEG macromolecules hydrate, whereas in water-PEG-KOH systems, both PEG macromolecules and K^+ and OH^- ions are hydrated. This also leads to the deterioration of the solubility of PEG by increasing the number of K^+ and OH^- ions in the solution.

Table 2. Dependence of parameter α in Mark-Kuhn-Hawing formula on the KOH concentration (x) on the water-PEG-KOH systems (T=293.15 K).

x	0	0,01	0,02	0,03	0,04	0,05
α	0,715	0,708	0,693	0,693	0,678	0,683

α parameter which is included in the Mark-Kuhn-Hawing formula, is the quantity that allows to determine the shape of the polymer molecule in the solution and any interaction that changes the shape of the polymer molecule changes the value of α. α value varies ($0 \leq \alpha \leq 2$). When a macromolecule is spherical, the surrounding fluid medium cannot penetrate into it, and this parameter $\alpha = 0$ is characterized this case. The coil-shape non-excited macromolecules in the θ-solvent alpha is $\alpha = 0,5$. With a rod-like conformation of a rigid macromolecule, $\alpha = 2$ [12-15]. The dependence of parameter α include in the Mark-Kuhn-Hawing formula on the concentration of KOH is shown in Table 2.

Our studies show that parameter α obtains values at temperatures of 293.15 K and at the concentrations of KOH we study (0,68-0,72). Then, based on the above considerations, we can say that, PEG macromolecule is a coil form of water that can penetrate the surrounding fluid in a water-KOH environment. In other words, PEG is a good solvent in macromolecular water-KOH environment has a shape flexible chain swollen-coil [12-15]. As can be seen from Table 2, the α parameter partially decreases with increasing KOH concentration. This indicates that, with increasing concentrations of KOH in the solution, at least this molecular coil is accumulated, that is, the size of the PEG macromolecule decreases.

Based on the intrinsic viscosity ($[\eta]$) values of the water-PEG-KOH systems (table 1) (6), the θ-constant K_θ was assigned and based on the known values of K_θ, the ($[\eta]_\theta$) intrinsic viscosity of the θ-solvent according to the studied system of PEG was calculated by the expression (5) (Table 3). As can be seen from Table 3, the characteristic value of PEG in the θ-solvent increases with increasing molar mass of PEG and concentration of KOH. Changing the PEG intrinsic viscosity the θ-solvent depending on the molar mass ($[\eta]_\theta \sim M$) of the PEG, when solvent is water-KOH analogical explanation of the dependence of characteristic behavior on the molar mass ($[\eta] \sim M$) can be explained. It is known that the polymer molecules and solvent molecules in θ-solvent are not interacting with each other, that is, the polymeric macromolecules in θ-solvent are not excited and $\alpha = 0,5$ remains constant for this case [13]. Therefore, the accumulation or opening of molecular coil does not occur for the given molecular mass PEG given in the θ-solvent depending on the concentration of KOH. Suppose that for taken the molecule mass of PEG with increasing concentrations of KOH the increase in $[\eta]_\theta$ result in increase the molecular coil volume ($[\eta]_\theta \sim R_{\theta h}^3$, $[\eta]_\theta \sim R_{\theta g}^3$) and θ-solvent is partly increase viscosity of environment.

Table 3. Dependence of the intrinsic viscosity ($[\eta]_\theta$, dl/q) and the swelling coefficient (β) of the PEG macromolecule in θ-solvents on the concentration of KOH (x) according to chosen water-PEG-KOH systems (T=293,15 K).

x	PEQ-1000	PEQ-1500	PEQ-3000	PEQ-4000	PEQ-6000
	$[\eta]_\theta$, dl/q				
0	0,0212	0,0259	0,0367	0,0423	0,0519
0,01	0,0216	0,0265	0,0374	0,0432	0,0529
0,02	0,0226	0,0277	0,0392	0,0452	0,0554
0,03	0,0220	0,0269	0,0381	0,0440	0,0539
0,04	0,0230	0,0281	0,0398	0,0459	0,0563
0,05	0,0225	0,0276	0,0390	0,0450	0,0552
	β				
0	1,172	1,220	1,226	1,255	1,373
0,01	1,146	1,199	1,214	1,233	1,333
0,02	1,123	1,175	1,183	1,213	1,287
0,03	1,137	1,184	1,188	1,212	1,311
0,04	1,113	1,159	1,160	1,195	1,265
0,05	1,104	1,165	1,168	1,193	1,261

The swelling of a macromolecular coil in a non ideal solvent is β times higher than in a θ-solvent. Coefficients β of the swelling of PEG macromolecules were determined according to Eq. (9), using the obtained values of and. Our values of β depending on M and x are given in Table 3. Table 3 shows that parameter β grows along with the molecular weight of the polymer, but it is virtually independent of temperature. The size of polymer coil in non-ideal solvents β times larger than the θ-solvent due to its swelling in the solvent. Based on the water-PEG-KOH system and the intrinsic viscosity value of the selected θ-solvent according to (9), the swelling rate of macromolecular coil β was calculated (table 3). As can be seen from Table 3, the coefficient of swelling of the PEG macromolecule in the water - KOH system increases with the increase in the molar mass of PEG decreases with increasing concentrations of KOH in solution. Increase of β with increasing molecular weight of PEG is probably due to hydration of hydrogen (hydrogen bond). Thus, the relatively high molecular weight PEG is more hydrated. The decrease in β with increasing concentrations of KOH in the solution relates probably due to the hydration of K^+ and OH^- ions in the solution as well as the increase in the viscosity of the medium. It is assumed that hydration of PEG macromolecules in water-PEG-KOH systems is weaker than in water-PEG systems.

Excited in solvent ($\langle h \rangle$) and non-excited in θ-solvent ($\langle h_\theta \rangle$) PEG were calculated by the

expression of the root-mean-square distance (7) between the ends of the macromolecule chain (Table 4). As can be seen from Table 4, the root-mean square distance between the edges of the excited PEG macromolecule increases with the increase in the molar mass of the PEG, decreases with increasing concentrations of KOH in solution. However, the root-mean square distance between the edges of the non-excited PEG macromolecule chain, increases with increasing both molar mass of PEG and concentration of KOH in solution.

Table 4. Dependence of the root-mean-square distance ($\langle h \rangle$ and $\langle h_\theta \rangle$, $\mathring{A}$) in the water-PEG-KOH systems and the θ-solvents chosen according to these systems on the KOH concentration (x) (T=293,15 K).

x	PEQ-1000	PEQ-1500	PEQ-3000	PEQ-4000	PEQ-6000
			$\langle h \rangle$, $\mathring{A}$		
0	25,33	32,28	45,86	54,22	72,67
0,01	24,92	31,95	45,74	53,63	70,99
0,02	24,79	31,79	45,24	53,57	69,64
0,03	24,87	31,73	45,04	53,03	70,24
0,04	24,72	31,52	44,60	53,03	68,76
0,05	24,35	31,47	44,63	52,63	68,13
			$\langle h_\theta \rangle$, $\mathring{A}$		
0	21,60	26,46	37,42	43,20	52,91
0,01	21,75	26,64	37,67	43,50	53,27
0,02	22,08	27,04	38,25	44,16	54,09
0,03	21,88	26,80	37,90	43,76	53,60
0,04	22,20	27,19	38,45	44,40	54,37
0,05	22,05	27,01	38,19	44,10	54,01

The rigidity and mobility of a macromolecular chain play an important role in shaping the conformation of a polymer macromolecule. It is known that Kuhn segment length (A) is a characteristic of the rigidity and flexibility of a macromolecule. If the chain is very mobile, then the length of the Kuhn segment is equal to the length of the contour of a ring, if the chain is too rigid, then the full length of the chain is equal to L. For water-PEG-KOH systems excited (A) and non-excited (A_θ) in PEG macromolecules in θ-solvent the dependence of KOH concentration on the length of Kuhn segment calculated by the expression (10) is given in Table 5.

Table 5. Dependence of Kuhn segment length (A və A_θ, $\mathring{A}$) in the water-PEG-KOH systems and the θ-solvents chosen according to these systems on the KOH concentration (x) (T=293,15 K).

x	PEQ-1000	PEQ-1500	PEQ-3000	PEQ-4000	PEQ-6000	A_θ , $\mathring{A}$
			A , $\mathring{A}$			
0	11,96	12,95	13,07	13,70	16,41	8,70
0,01	11,58	12,69	13,00	13,41	15,66	8,82
0,02	11,46	12,56	12,72	13,38	15,07	9,09
0,03	11,53	12,51	12,61	13,11	15,33	8,93
0,04	11,39	12,35	12,36	13,11	14,69	9,19
0,05	11,05	12,31	12,38	12,91	14,42	9,07

As can be seen from Table 5, the Kuhn segment length of the excited PEG macromolecule by the water-PEG-KOH systems increases with the increase in the molecular weight of the PEG, decreases with increasing concentrations of KOH in solution. The length of the Kuhn segment of the non-excited PEG macromolecule in the θ-solvent is independent of the molecular mass of the PEG, and increases with increasing concentrations of KOH (Table 5). In all cases where we look at water-PEG-KOH systems since the Kuhn segment is less than 100 $\mathring{A}$, so PEG can be considered as a mobile polymer.

5. REFERENCES

1. Sung J.H., Lee D.C., Park H.J. Polymer, 2007, vol. 48, p.4205-4212.
2. Lange K.P. Surfactants, synthesis, properties, analysis, application. "Professiya", 2005. 240 p.
3. Sibileva M.A., Tarasova E.V. Russian Journal of Physical Chemistry, 2004, vol. 78, №7, p.1240-1244.
4. Polik W.F, Burchard W. Macromolecules, 1983, Vol. 16, p. 978-982.
5. Duval M. Macromolecules, 2000, Vol. 33, p.7862-7867.
6. Shulyak I.V., Grushova E.I. Russian Journal of Physical Chemistry, 2013, vol. 87, № 3, p. 453-456.
7. Masimov E.A., Pashayev B.G., Hasanov H.Sh., Musayeva S.I. Russian Journal of Physical Chemistry, 2013, vol. 87, №12, p. 2105-2107.
8. Masimov E.A., Pashayev B.G., Hasanov H.Sh. Russian Journal of Physical Chemistry, 2019, vol. 93, № 5, p. 988-990.
9. Masimov E.A., Pashayev B.G., Hasanov H.Sh., Hajiyeva Sh.N. Russian Journal of Physical Chemistry, 2019, vol. 93, № 6, p. 1054-1058.
10. Pashayev B.G. Conference Proceedings, Modern Trends In Physics Baku, 01-03 May, 2019, p.170-174.
11. Masimov E.A, Pashayev B.G., Orujova N.F. Conference Proceedings, Modern Trends In Physics Baku, 01-03 May, 2019, p. 191-195.
12. Masimov E.A., Hasanov H.Sh., Pashayev B.G. Liquid viscosity. Baku, "Publishing House Laman", 2016, p 285.
13. Tager A.A. Physico-chemistry of polymers. M.: Scientific world, 2007, 576 p.
14. Rafikov S.P., Budtov V.P., Monakov Y.B. Edited by Korshaka V.V. Introduction to the physical chemistry of polymer solutions. M.:Nauka,1978. p. 328.
15. Chvetkov V.N., Eskin V.E., Frenkel S.Y. The structure of macromolecules in solutions. M.:Nauka, 1964.
16. Stokmayer W.H., Fixman M. J. Polym. Sci. 1963, Part C. №1. p.137.
17. Manjay V.N., Saricheva G.A., Berzina E.M. High molecular weight compounds, series B, 2003, 45, № 2, p. 363-368.

EFFECT OF ETCHING ON THE ELECTRICAL PROPERTIES OF $ZnS_{1-X}Se_X$/P-Si and $ZnSe_{1-X}Te_X$/P-Si HETEROJUNCTIONS

E.A. CHANMAMMADOVA

Institute of Physics of Azerbaijan National Academy of Sciences, Huseyn Javid 33, Az1141, Baku Azerbaijan

The $ZnS_{1-x}Se_x$/p-Si and $ZnSe_{1-x}Te_x$/p-Si heterojunctions were prepared by deposition of $ZnS_{1-x}Se_x$ (or Te_x) (x = 0; 0.1; 0.2) films by electrochemical deposition onto the surface of p-Si etched in KOH+alcohol and HF+HNO$_3$ solutions. It was found that the current passage mechanism and the electrical parameters of the heterojunctions depends on the etching duration, temperature and concentration (KOH and HF (3-5%); 10 vol%) of KOH + alcohol and HF + HNO$_3$ solutions.

1. INTRODUCTION

There are several etching methods with different solvents which can improve the electrical properties of semiconductor structures [1-6]. An experiments carried out show that etching in KOH+C_3H_8O and HF+HNO$_3$ solutions leads to arising of the pyramids (or pits) on the surface of silicon that dependence of its morphology and dimensions on the temperature, concentration of solvents and etching duration [7-12]. So, as the changes arising on the surface is clear watched after etching during 20-30 minutes, in this paper are investigated heterojunctions based on Si, that etching during ≥20 min.

2. EXPERIMENT

Monocrystalline wafers of p-Si (100) with thicknesses 800 μm and resistivity (0.8-1) Ω·cm were used as absorber. Before texturization, the Si wafers were cleaned by acetone, ethanol, and deionized water and dried by N_2 gas. The texturing of wafers was carried out in two types of solutions: KOH (1-5 wt%) + C_3H_8O (3-10 vol%) + H_2O (100 ml) and HF (1-5 wt%) + HNO$_3$ (3-10%) + H_2O (100 ml). The samples with dimension of 2 × 2 cm^2 were separated from one wafersof p-Si, and each sample was etched in differentsolutions, temperature and etching time.

After texturing, the p-Si wafers were cleaned by ethanol, deionized water and dried by N_2 gas. Samples with 1×1 cm^2 dimension were separated from each textured Si wafers and used as substrate (as a cathode) for electrochemical deposition of $ZnS_{1-x}Se_x$ and $ZnS_{1-x}Te_x$ films.

Electrochemical deposition of the $ZnS_{1-x}Se_x$ (x=0; 0.1; 0.2) films onto the textured p-Sisubstrates was carried out at temperature of 80°C. The electrodeposition bath system is composed of $ZnSO_4$ as source of cation, SeO_2 and $Na_2S_2O_3$ as source of anions, H_2SO_4 as pH control, K_2SO_4 as inert electrolyte and distilled water. Cyclic voltammetry was used to monitor the electrochemical reactions in solutions of $ZnSO_4$, SeO_2 and $Na_2S_2O_3$, then in their combined solution of the same concentration and pH. The cyclic voltammograms was scanned in the potential range 1.2 V to –1.2 V versus graphite (or Ag/AgCl) electrodes. Depending on the deposition time, $ZnS_{1-x}Se_x$films with thickness up to 520÷530nm with different morphology were deposited from a solution.Pure aluminium (Al) was used as the back electrode contact. The front contact was made by Al, and indium (In) materials in a grid form.

3. RESULTS AND DISCUSSIONS

It is established that the desired distribution of the pyramids and pits can be reach by the controlling the solution concentration. The surface of Si is covered by equally distributed pyramids (or pits) after the etching by 40 minutes. It is important condition for increasing of stability of parameters of solar cells (Fig.1 and Fig.2). Note that following escalating of concentration and solution temperature and the etching duration does not lead to changes of surface morphology of the Si plates.

The static I-U characteristics of p-Si/ZnS heterojunctions before etching and after the etching in different regimes are given in Tables 1 and 2, and are presented in Fig. 3-6. As seen from figure, all types of heterojunctions show rectification and the rectification direction appropriates to positive direction of applied voltage.

Table 1. The etching regimes of the Si plates in solution of KOH+C_3H_8O

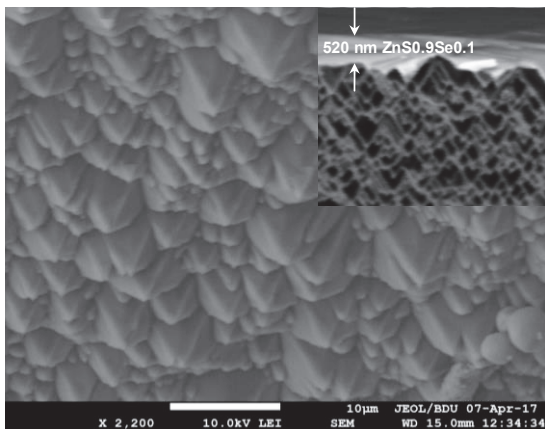| Samples	Concentration of KOH, wt%	Concentration of C_3H_8O, vol%	Solution temperature, ^0C	Etching duration, minutes
SK1	1	3	80	20
SK2	1	3	80	30
SK3	2	6	80	30
SK4	3	6	80	40
SK5	3	10	90	50
SK6	5	10	80	60

Figure 1. SEM images of SK4 samples surface

Table 2. The etching gerimes of the Si plates in solution of HF+HNO_3

Samples	Concentration of HF, wt%	Concentration of HNO_3, vol%	Solution temperature, ^0C	Etching duration, minutes
SH1	1	3	80	20
SH2	2	3	80	30
SH3	3	6	80	30
SH4	5	8	80	40
SH5	6	9	90	50
SH6	5	10	80	60

It was impossible to get good rectification (k=50-80) in heterojunctions based on the non-etched p-Si because of high resistivity of ZnS films, despite of the lattice parameters of p-Si and n-ZnS semiconductor materials are enough closely (appropriately 5.431 Å and 5.410 Å). On the other hand, existing on the Si surface SiO_x oxide type layer that is practically impossible to remove by different types technology procedures is another cause of obtaining not good rectification. However, etching in KOH+C_3H_8O solution leads to removing of the oxide layer on the surface and to arising different types of nano- and micro- junctions on interface, which all parameters of the final matrix are defined by parameters of these junctions.
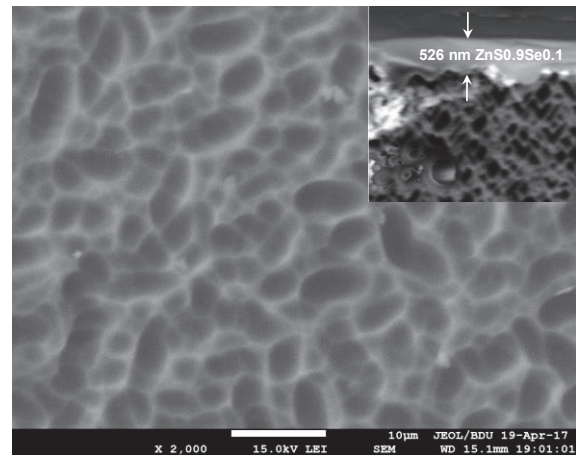
Figure 2. SEM images of SH4 samples surface

So, unequal size of pyramids on the surface of p-Si and uneven distribution of the pyramids on the surface depending on etching regimes (samples SK1, SK2 and SK3 in Table 1 and samples SH1, SH2 və SH3 in Table 2) leads to such formation of the ZnS thin films. As a result, the drift direction of electrons and holes at interface, under an external electric field changes irregularly. In this case, the carry mechanism and also the direction of current in nano size heterojunctions distributed over the surface are sharply different. The difference between the concentration of charges on the top and base of pyramids to leads arising of the same effect as on semiconductor drift transistors in case of heterogeneous alloy. So, due to concentration gradient between free charges carriers on the top and base of pyramids with height of *h,* arise the diffusion currents which are determined by following expression:

$$j_D = eD \frac{dn}{dh} \qquad (1)$$

This current leads to redistribution of free charge carriers, but the ionized donors (or acceptors) stay on junction interface. As a result, there is arising an extra electric field on the junction region, which lead to separation of electron-hole pair and finally, to arising the drift component of current. Of course, the drift electrical field that arisen due to equalization of pyramids sizes (samples SK4) can be stable and have got high value.
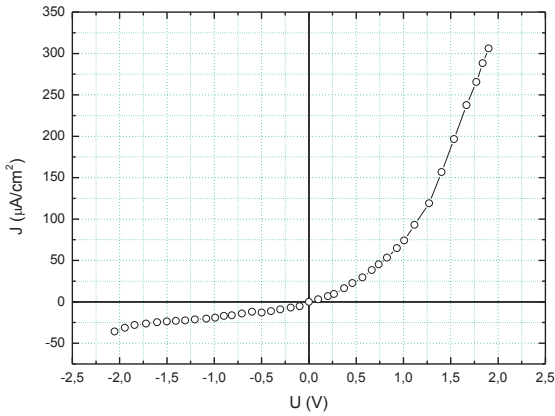
a)
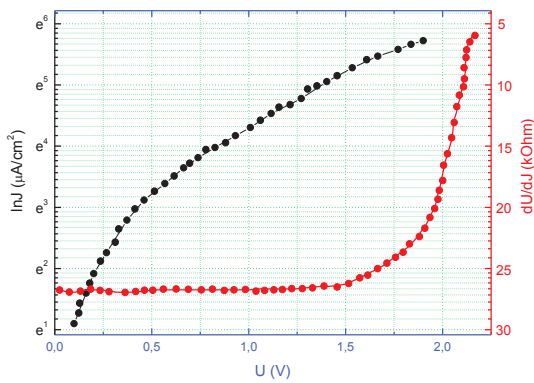
b)

Figure 3. Static I-U characteristics of non-etched p-Si/ZnS heterojunctions at 300 K (a); dependences of lnJ = f(U) and dU/dJ = f(U) (b).

Electrical field arisen due to concentration gradient

$$E(h) = \frac{D_p}{\mu_p} \cdot \frac{dn(h)}{n(h)dh} \qquad (2)$$

Here D – drift coefficient of charge carrier; μ - mobility; n – concentration of electrons.

Taken in account of $\frac{D}{\mu} = \frac{kT}{e}$ in expression (2) we will get following

$$E(h) = \frac{kT}{e} \cdot \frac{dn(h)}{n(h)dh} \qquad (3)$$

As seen from expression the drift electrical field arising due to the concentration gradient is determined by distribution law of charge carrier on the boundary line (pyramid) of junction. So, high gradient of concentration will cause the high value of electrical field. On certain approach, the concentration gradient should be determined by gradient of change of sizes between base and top of geometrical figures (pyramids or oval pits) arising on the junction during the etching. As, this difference greater on pyramid than oval after etching in same regimes of the heterojunctions based on SK samples show better rectification than the

heterojunctions based on SH samples. It is clear that a size of the field and its stability depending on homogeneity of distribution of geometrical figures.

As seen from Fig.3b, thermo-emission mechanism is priority in transfer of current in the p-Si/ZnS heterojunctions:

$$= {}_0 exp\left(\frac{eU}{AkT}\right) \qquad (4)$$

As can be seen from the figure, at lower values of the external voltage, the forward region of the I-U characteristic corresponds to the exponential law, and at higher voltages, to the linear law. The contact potential difference on the heterojunctions with value of U_d=0.84V is determined by an extrapolation of the direct part of the I-U characteristics to voltage axe.

The calculation for dependency curve ln(J)=f(U), presented in Fig.3b on semi- logarithmic scale, show that non-ideality coefficient of the I-U characteristics for the non-etched p-Si/ZnS heterojunctions are A= 2.4 (U=0.5-0.88 V) and A=4.3 (U = 0.89 V). High resistivity of ZnS films and presence of SiO_2 or SiO_x type of oxide layer on surface of Si is a reason of the high of non-ideality coefficient. It is clearly, that if series resistance will be small and an oxide layer will be away then I-U characteristic should be complied with the exponential law and A will be equal to 1. As note in [7], I-U characteristics for the studied case can be described by following expression:

$$= {}_0 exp\left(\frac{e(U-U_a)}{kT}\right) = {}_0 exp\left(\frac{e(U-JR_a)}{kT}\right) \qquad (5)$$

Here $U_a = JR_a$ is voltage drop on series resistance of the heterojunction.

Taken into account last expression the non-ideality coefficient of V-A characteristic is determined as:

$$A = \frac{U}{U-U_a} \qquad (6)$$

As, on the small external voltage $U_a = JR_a \ll U$ the main part of voltage at low voltages dropped on junction, therefore I-U characteristics corresponds to exponential dependency ($A{\approx}1$).When external voltage increases, voltage drop in series resistance also increases, at the same time is occurred retaining of the free charge carriers on the oxide layer and this leads to obtaining the high value of non-ideality coefficient of I-U characteristic due to the increasing of recombination acts in the junction zone. The series resistance is calculated by approximation of linear part of the dependence $dU/dI=f(U)$ [86] (Fig.3b). As can be seen from Fig.3b, the series resistance at low voltages is almost stable and equal 26-27 kOhm/cm². However, with increasing voltage the series resistances sharply decrease up to 1.8-2 kOhm/cm². This effect submits of real presence of an oxide layer in the junction region. So, the charge carriers retained in the oxide layer at low voltages, become free due to the strike ionization by

increasing of voltage, take part in increasing of current again. The ionization of the charge carriers and decreasing of series resistance is occurred at same time.
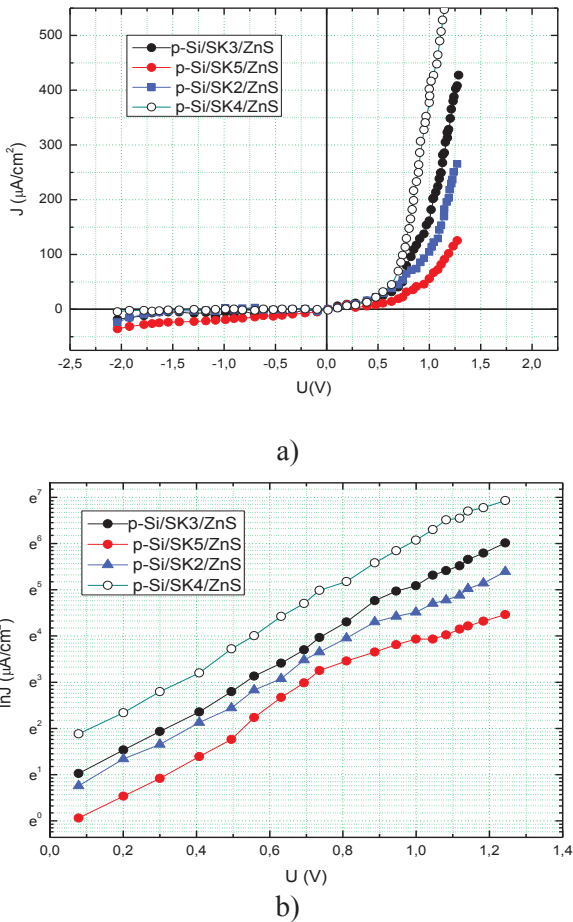

a)

b)

Figure 4. Static I-U characteristics of p-Si/SK/ZnS heterojunctions (a) and dependencies of $lnJ = f(U)$ (b) at 300 K.

The current passing mechanism in heterojunctions after etching in solutions $KOH+C_3H_8O$ and $HF+HNO_3$ sharply changes. Besides, at the same time the etching removes oxide layer in junction region of heterojunctions and increases of the series resistance value due to the increasing substrate thickness (Table 3). On the other hand, the texturization of surface creates additional drift field and stimulates to the separation of electron-hole pairs that leads to decreasing of recombination acts in junction region and to significant increasing of rectification (Fig. 5). As seen from Fig. 5, etching in solutions with small concentration (samples SK1, SK2, SK3) lead to not only increase of direct current and to change of its increasing law and the significant decrease of the reverse current. This fact once again submits of the removing of the oxide layer during the etching. While on dependency $lnJ=f(U)$ of non-etched p-Si/ZnS

heterojunctions are observed three part, after etching observed only two and even in heterojunctions based on SK4 almost observed one part with inclination (Fig. 5b). As seen from Table 3 and curve, the heterojunctions based on SK4 show the best rectification. Although during the etching with more high concentration and duration the homogenies of the texture does not break, but width of pyramids decreases due to increasing their height on the surface. And it increases tunnel recombination acts in nano-heterojunctions arising on the side surface of pyramids. As a result, in the etched on such regime heterojunctions based on substrates (SK5, SK6) and thus the rectification worse again and the incline of their dependency $lnJ=f(U)$ decreases and this show increasing of non-ideality coefficient of I-U characteristic. Though choosing of the optimal etching mode, due to the impossibility of decreasing enough of the resistivity of ZnS thin films by admixture, the heterojunctions on their base does not show good rectification. In this regard, thin films solutions of ZnS-ZnSe and ZnSe-ZnTe systems were used in this paper.

Adding of an insignificant amount of Se (20%) to ZnS has been allowed to increase the value of rectification coefficient k=1800-2000 (Fig.5 and Table 3). Really would be possible by increasing of amount of Se for to decrease of thin films of ZnS-ZnSe system, thus to increase the rectification of heterojunctions. However, increasing of the molar amount of Se up to $x=0.2$ leads to the increasing of disparity between the lattice parameters of Si and $ZnS_{1-x}Se_x$ and as a result to increasing concentration of defects in junction zone. And it leads to worse the parameters of the on their base heterojunctions.
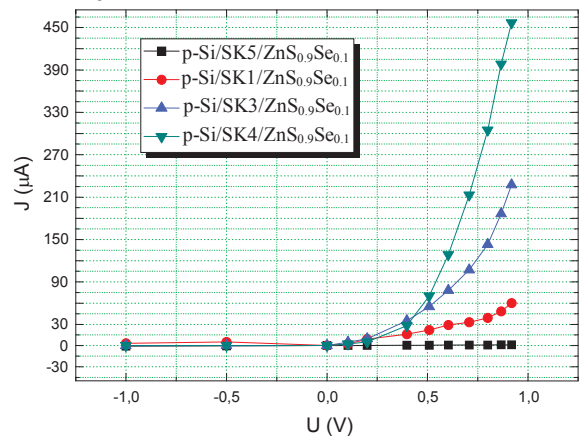

Figure 5. Static I-U characteristic of p-Si/SK/$ZnS_{1-x}Se_x$ heterojunctions based on SK substrates

The heterojunctions based on SH substrates show the same characteristics, (Table 3).

Table 3. Electrical parameters
of p-Si/ZnS$_{1-x}$Se$_x$ heterojunctions

Samples	k	R Ohm·cm	A
Non-etched p-Si/ZnS	90	2200	2.4 və 4.3
p-Si/SK1/ZnS	180	700	2.0
p-Si/SK2/ZnS	280	340	2.0
p-Si/SK4/ZnS	600	95	1.58
p-Si/SK4/ZnS$_{0.9}$Se$_{0.1}$	1790	16	1.4
p-Si/SK4/ZnS$_{0.8}$Se$_{0.2}$	1200	64	1.6
p-Si/SH1/ZnS	100	950	2.7
p-Si/SH2/ZnS	190	670	2.6
p-Si/SH4/ZnS	480	210	2.0
p-Si/SH4/ZnS$_{0.9}$Se$_{0.1}$	1400	48	1.7
p-Si/SH4/ZnS$_{0.8}$Se$_{0.2}$	900	124	1.9

Thin films of ZnSe-ZnTe system solutions show in concrete cases very good rectification, and p-Si/ZnSe$_{1-x}$Te$_x$ heterojunctions based on films ZnSe$_{1-x}$Te$_x$ even without texturing.
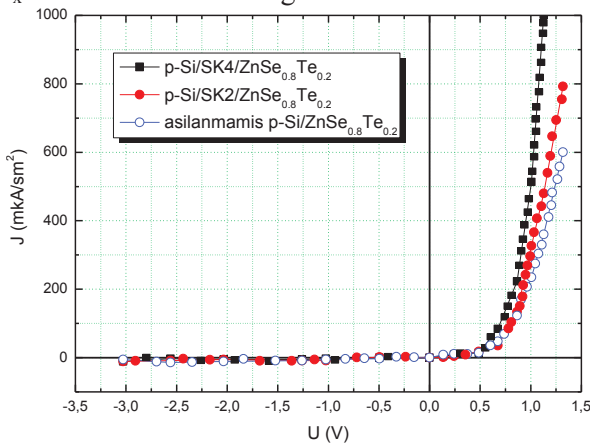

Figure 6. Static I-U characteristics of p-Si/SK/ZnSe$_{0.8}$Te$_{0.2}$ heterojunctions based on SK substrates heat treated in argon environment, non-etched and etched on different regimes.

So, p-Si/SK/ZnSe$_{0.8}$Te$_{0.2}$ heterojunctions show rectification coefficient k = 1200÷1300 after the HT at temperature 340°C in argon environment. During this due to recrystallisation process junction region is formed, and the series resistance of the heterojunctions decreases sharply, as shown in [7-9] (Table 4).

Table 4. Electrical parameters
of p-Si/ZnSe$_{1-x}$Te$_x$ heterojunctions

Samples	k	R Ohm·cm	β
Non-etched p-	25	1700	2.5
Si/ZnSe$_{0.8}$Te$_{0.2}$ before HT			
Non-etched p-Si/ZnSe$_{0.8}$Te$_{0.2}$ after HT	1280	140	1.8-2.0
p-Si/SK2/ZnSe$_{0.8}$Te$_{0.2}$	1600	80	1.5
p-Si/SK4/ZnSe$_{0.8}$Te$_{0.2}$	2500	34	1.2
p-Si/SH4/ZnSe$_{0.8}$Te$_{0.2}$	2200	60	1.2

The solid solutions of the compounds A^{II}B^{VI} with Te are very persistent to ambience – in concrete case to absorbing of oxygen to surface [7]. Therefore, at HT of the ZnSe$_{0.8}$Te$_{0.2}$ in argon environment desorbing of oxygen is not occurred almost, i.e. in thin films during the HT is occurred recrystallization process.

HT of p-Si/ZnSe$_{0.8}$Te$_{0.2}$ heterojunctions at temperature of 340°C for 11-12 minutes increases rectification 1.8-2 times (Fig.6). This is related with the drift processes. I-U characteristics in heterojunctions for direct direction until 0.6 V can be describe by following expression:

$$I = I_0 \exp(eU / \beta kT) \qquad (7)$$

Based on deviation of dependency lnJ=f(U) the non-ideality coefficient for p-Si/ZnSe$_{0.8}$Te$_{0.2}$ heterojunctions without texturing is established as $\beta = 1.8 - 2$, for heterojunctions with texturing - $\beta = 1.2$. This submit that the current in given type of heterojunctions based on thin films with Tellurium is submitted to generation-recombination mechanism and affirms the decreasing of the recombination currents in junction zone on texturing. From the V-A characteristic of heterojunctions the potential difference is determined as $V_d = 0,57$V.

4. CONCLUSION

Texturization of surface creates additional drift field and stimulates to the separation of electron-hole pairs that leads to decreasing of recombination acts in junction region and to significant increasing of rectification.

5. REFERENCES

1. Edited by Prof. Leonid A. Kosyachenko, Solar Cells - Silicon Wafer-Based Technologies, InTech, 2011, p.364.
2. Fırat Es, Gülsen Baytemir, Mustafa Kulakci, RaşitTuran / Solar Energy Materials & Solar Cells, 2017,160, p.269.
3. Wisam J. Aziz, AsmietRamizy, K. Ibrahim, Khalid Omar, Z. Hassan / Journal Of Optoelectronics And Advanced Materials, 2009, 11, p.1632.

4. Altinoluk SH, Ciftpinar HE, Demircioglu O, Es F, Baytemir G, Akar O, et al./ Energy Procedia 2016, 92, p.291.

5. Basu P.K., Khanna A., Hameiri Z. / Renewable Energy, 2015, 78, p.590.

6. Zhao J, Wang A, Green MA., Applied Physics Letters 1998, 73, p.1991.

7. Mamedov H., Mammadov V., Mammadova V., Ahmedova Kh. , Tagiyev E., Agazade L. / Journal Of Optoelectronics and Advanced Materials 2018, 20, p.468.

8. Abdinov A., Mamedov H., Amirova S. / Thin Solid Films, 2006, 511-512, p.140.

9. Mamedov H., Konya Z., Muradov M., Kukovecz A., Kordas K., Hashim D., Mamedov V. / J. Solar Energy Engineering 2014, 136, p.044503.

10. Kaifu Q., Depeng Q., Lun C., Shenghao L., Weiliang W., Zongcun L., Hui Sh./ Materials Letters 2017, 198, p.23.

11. Kaifu Q., Qi X., Depeng Q., Lun C., Weiliang W., Wenjie L., Zhirong Y., Bin A., Zongcun L., Hui Sh. / Solar Energy 2018, 165, p.35.

12. Liang-Wen J., Yu-Jen H., I-Tseng T., Teen-Hang M., Chien-Hung L., Jenn-Kai T., Tien-Chuan W. and Yue-Sian W., Nanoscale Research Letters 2013, 8, p.470.

SURFACE FREE ENERGY AND CHEMICAL STRUCTURE OF POLYIMIDE THIN FILMS PREPARED BY VAPOR DEPOSITION POLYMERIZATION

Y. YAMADA*, H. KAGAWA

Komatsu University, Department of Production Systems Engineering and Sciences
Nu-1-3, Shichou-machi, Komatsu City, Ishikawa Prefecture, 923-8511, Japan

Polyimide films were synthesized by annealing polyamic acid (PAA) films deposited on glass or quartz crystal substrates by means of the vapor deposition polymerization of pyromellitic dianhydride and oxydianiline monomers. The optimum monomer evaporation temperatures were determined using differential scanning calorimetry, X-ray diffraction and scanning electron microscopy to characterize the PAA films. Fourier transform infrared spectra showed that the imidization reaction of the PAA films was accelerated with increasing annealing temperature. The amount of water vapor adsorbed on these films was measured using a quartz crystal microbalance and the surface free energy was estimated based on contact angle measurements. The polar component of the surface free energy was found to decrease with increasing annealing temperature, due to a decrease in the concentration of hydrophilic groups in the film. These results indicate a significant positive correlation between the polar component of the surface free energy and the extent of water vapor adsorption.

1. INTRODUCTION

Polyimides (PIs) have a wide variety of applications because they exhibit exceptional mechanical, thermal, electrical and chemical properties. Fig. 1 summarizes the typically PI film fabrication procedure. In this process, a polyamic acid (PAA) film is first synthesized from pyromellitic dianhydride (PMDA) and oxydianiline (ODA) monomers using a solution cast method, after which this film is annealed to obtain the PI film. However, using this method, it is difficult to control the thickness and uniformity of the films, and pinholes are induced by residual solvent evaporation during annealing of the initial PAA [1].

Dry processing methods that do not use solvents are an alternative for the preparation of polymer films. These include sputter deposition, chemical vapor deposition (CVD) and vapor deposition polymerization (VDP). In early studies of sputter deposited PI films, the lubrication characteristics of films were investigated [2, 3], while more recent research examined the wear properties [4] and hardness [5] of sputter deposited PI films. The effects of various discharge parameters, including power, pressure and discharge gas, on the chemical structure and dielectric properties [6, 7] as well as the composition of the deposited films [7] have been investigated. However, the sputter deposition process is complicated, and the structure and composition of the resulting films are often far different to those of the sputtering targets.

VDP is an alternate dry process that is superior to sputter deposition in terms of controlling the chemical structure of the product. This method was first applied to polyimides independently by Iijima et al. [8] and Salem et al. [9]. During VDP, PAA films are prepared by means of the co-evaporation of ODA and PMDA monomers, and then transformed to PI films by annealing. In order to obtain smooth, homogeneous, and crystal-free PAA films, it is important that the ODA and PMDA monomer fluxes are well balanced during VDP [10-13]. The majority of studies to date have focused on controlling the temperature of the monomer reservoirs as a means of obtaining high quality PAA, as well as optimizing the annealing conditions.

PI films fabricated using VDP have potential applications in the separation of helium and other gases [14], as electric insulators [15] and in electroluminescent devices [12]. Solvent cast PI films are promising for use as flame retardants, UV protective coatings and waterproof coatings [16]. The sorption and diffusion of water vapor in these films [17] and their use as reverse osmosis membranes [18] have also been investigated by several researchers. The interface between such films and their substrates

is important in determining the properties of layered structures in microelectronic devices and protective coatings.

The gas permeation and water vapor sorption/diffusion properties of these materials are closely related to their surface characteristics, including surface free energy. Even so, to the best of our knowledge, the surface free energy for VDP PI films has not yet been examined. The paucity of reports on the surface properties of VDP PI films encouraged us to investigate these characteristics.

The objectives of the present study are to determine the optimum monomer evaporation temperatures for VDP (so as to obtain high-quality PAA films), to demonstrate the effects of annealing of these films on their chemical structure and surface free energy, and to establish the relationship between surface free energy and water vapor adsorption.

2. EXPERIMENTAL

2.1 Preparation of PI films

The two monomers, PMDA and ODA, were co-vaporized in a vacuum chamber to form PAA films on a substrate via the chemical reaction shown in Fig. 1. The PI was subsequently obtained as a result of the condensation reaction of the PAA. A schematic diagram
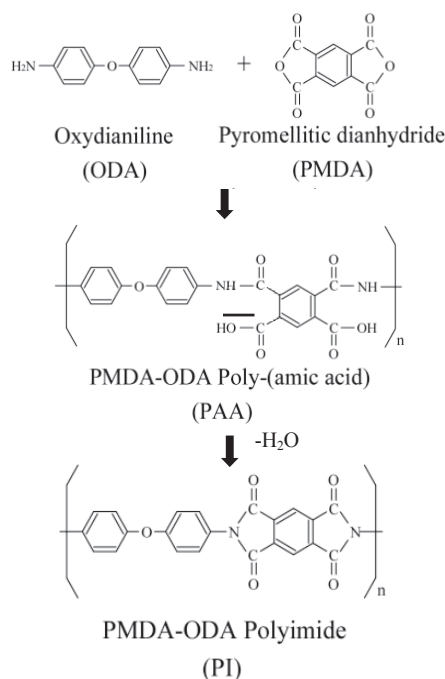

Figure 1. Chemical reactions producing polyimide.
Table 1. Evaporation temperatures for the ODA and PMDA monomers.

Temperature of ODA (°C)	Temperature of PMDA (°C)
185	180
	190
	200
	210
	220
180	200
190	
195	

Showing the apparatus is provided in Fig. 2. This apparatus included evaporation sources (Knudsen cells) and a substrate arrangement that allowed VDP. Each Knudsen cell had a small 0.5 mm diameter hole through which the monomer vapor escaped. Glass substrates (76×26×1.3 mm) were used for the measurements of the surface profiles and film thicknesses as well as the contact angle. Quartz crystal substrates (diameter of φ14 mm and thickness of 0.3 mm) were used for the water vapor adsorption measurements.

Prior to deposition, the vacuum chamber was evacuated to a pressure of 1.0×10^{-2} Pa, after which Ar gas (1.0 cm³/stp) was introduced into the chamber to give a pressure of 2.2×10^{-1} Pa. ODA and PMDA were subsequently co-evaporated to prepare PAA thin films. To establish the optimum temperatures for the evaporation sources so as to obtain homogeneous and high-quality PAA films, evaporation was performed at the temperatures listed in Table 1. In each case, the evaporation time was 20 min and the resulting film thickness was approximately 500 nm. The PAA films were annealed at 100, 150, 200 or 300 °C for 1 h in air then cooled to room temperature over a 6 h time span.
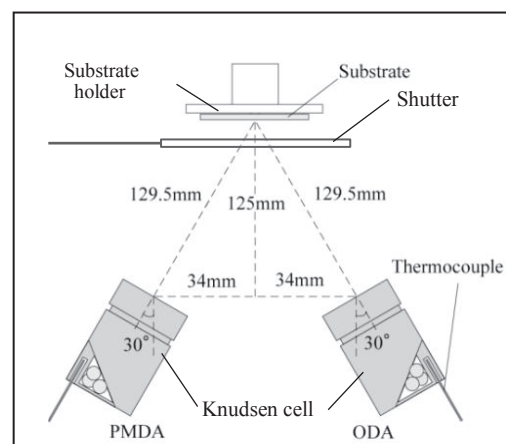

Figure 2. Schematic diagram showing VDP apparatus.

2.2 Characterization of the polymerized films

The film surfaces were examined using scanning electron microscopy (SEM) with a JSM-6390A

43

instrument (JEOL Ltd.). The thickness of the films was measured based on the step height between the film and the substrate, employing a contact probe surface profilometer (Surfcom1400A, Tokyo Seimitsu Co.). The root mean square surface roughness, Ra, was also measured using the Surfcom1400A. Differential scanning calorimetry (DSC) was carried out with a DSC-60P (Shimadzu Co.) at a heating rate of 10 °C/min. A powder sample (2 to 5 mg) scraped from the substrate was enclosed in an aluminum pan. X-ray diffraction (XRD) data were acquired using an X'Pert Pro instrument (PANalytical Co.), working with 10 μm thick films. Fourier transform infrared (FT-IR) spectra were obtained with an FT-720 (Horiba Ltd.) after forming samples scraped from the substrate into KBr pellets.

The surface free energy for the films was estimated based on contact angle measurements employing the liquid droplet method, using distilled water and diiodomethane. Drops having a volume of 4 μL were deposited on the film surface using a microsyringe and photographs of the drops were acquired with a digital camera. Contact angles were subsequently evaluated by analyzing the droplet shapes on a personal computer.

The surface free energy for the films, γ_S, as well as the dispersion and polar components, γ_S^d and γ_S^p, were calculated using equations (1) and (2) [19]

$$\gamma_S = \gamma_{SL} + \gamma_L \cos\theta \tag{1}$$

and

$$\gamma_{SL} = \gamma_S + \gamma_L - 2 \times (\gamma_S^d \times \gamma_L^d)^{1/2} - 2 \times (\gamma_S^p \times \gamma_L^p)^{1/2} \tag{2}$$

where θ is the contact angle of the probe liquid, γ_L is the surface free energy of the liquid, and γ_L^d and γ_L^p are the dispersion and polar components of γ_L (see Table 2 [19]), respectively.

Table 2. Surface free energies for the probe liquids [19] used for contact angle measurements.

	γ_L (mJ/m^2)	γ_L^p (mJ/m^2)	γ_L^d (mJ/m^2)
Distilled water	71.8	51	21.8
Diiodomethane	50.8	2.3	48.5

The quartz crystal microbalance (QCM) method was employed to evaluate the amount of adsorbed water vapor, using a quartz crystal having a resonance frequency of 6 MHz. The relationship between the mass of adsorbed water vapor, Δm (kg), and the resonance frequency shift, ΔF (Hz), is

$$\Delta F = -\frac{2 \times F_0^2}{A \times \sqrt{\mu \times \rho}} \times \Delta m \tag{3}$$

where A is the electrode area (m^2), μ is the shear stress applied to the quartz crystal (kg/(m·s^2)), ρ is the

density of the quartz crystal (kg/m^3) and F_0 is the original resonance frequency of the crystal (Hz) [20]. A schematic illustration of the apparatus used to measure water vapor adsorption is shown in Fig. 3. In these experiments, a QCM coated with a PI film was mounted on a stage in the vacuum chamber while 2 mL of water was contained in vessel C.

A typical record of the variation of the resonance frequency during adsorption measurements is provided in Fig. 4. Firstly, the chamber was evacuated to a pressure of 2.0×10^{-3} Pa in order to eliminate the impurity gases adsorbed on the QCM. Because the impurity gases are desorbed during the evacuation process, the resonance frequency increases and then plateaus at a value of F_0. Subsequently, valve A in Fig. 3 is closed and evacuation is stopped, after which valve B is opened and water vapor is introduced into the chamber for 30 min. Throughout the adsorption process, the resonance frequency decreases to a value of F, and the frequency shift, ΔF, between F and F_0 is correlated with the mass of adsorbed water vapor. The frequency shift when only air was introduced (without water vapor), ΔF_{Air}, was subtracted from the ΔF values for correction. The corrected value, $\Delta F'$, is therefore

$$\Delta F' = \Delta F - \Delta F_{Air} = (F_0 - F) - \Delta F_{Air} \tag{4}$$

Quartz crystal

Table 3 Quartz crystal specifications.

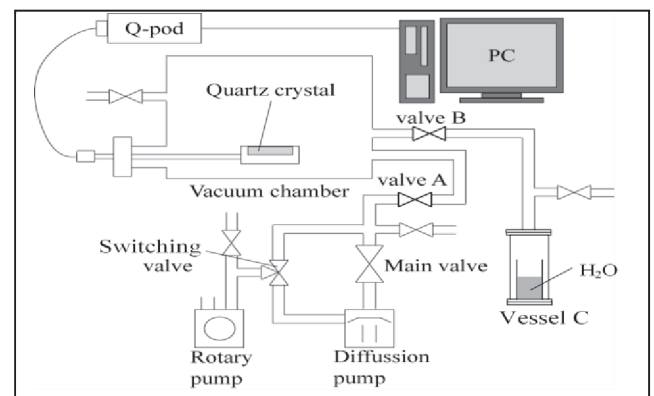| Dimensions (mm)	Ø=14, t=0.3
Resonance frequency (Hz)	6.0×10^6
Electrode	Au
μ (kg/(m·s^2))	2.95×10^{10}
ρ (kg/m^3)	2649

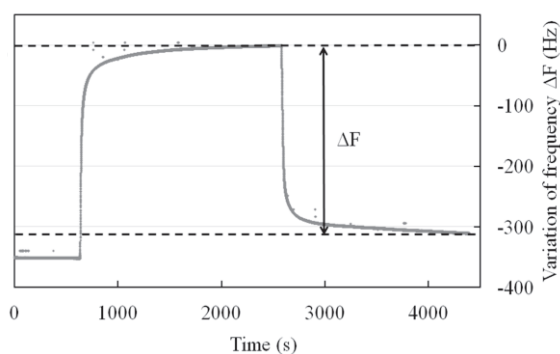Figure 3. Schematic illustration of gas adsorption measurement system.

Figure 4. Typical record of variation of resonance frequency during water vapor adsorption measurements for PAA films.

3. RESULTS AND DISCUSSION

3.1 Effects of evaporation temperature on film quality

Fig. 5 presents DSC curves obtained from films produced using an evaporation temperature for the ODA reservoir of 185 °C and various PMDA reservoir temperatures. Pure PMDA films (curve (f)) generated an endothermic peak at 290 °C while pure ODA films (curve (a)) produced an endothermic peak at 180 °C. In the case of the film deposited using a PMDA temperature of 190 °C (curve (b)), the endothermic ODA peak is clearly observed, indicating that the majority of the ODA did not react with the PMDA because the PMDA monomer flux was less than the ODA flux at that temperature. The films deposited at PMDA temperatures of 200 and 210 °C did not produce endothermic or exothermic peaks, demonstrating that the monomer fluxes were well balanced at these temperatures. In contrast, the film fabricated at a higher ODA temperature of 195 °C (curve (e)) shows a trace of the endothermic ODA peak. These data suggest that the optimum temperatures for the ODA and PMDA reservoirs were 185 and 200 or 210 °C, respectively.
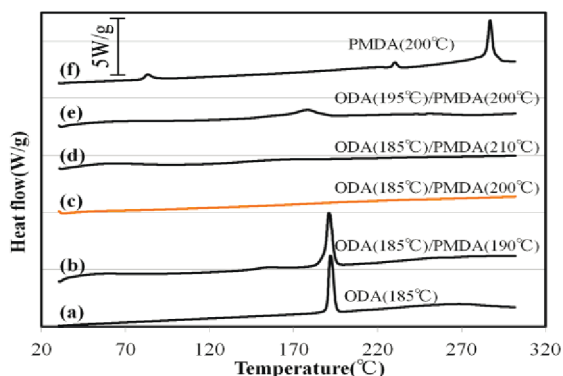

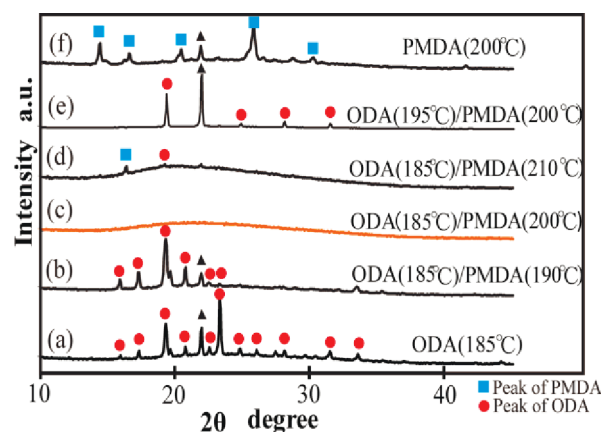Figure 5. DSC curves for films deposited at various ODA and PMDA temperatures.

Figure 6. XRD patterns for films deposited at various ODA and PMDA temperatures.

Fig. 6 shows XRD patterns acquired from films deposited at various ODA and PMDA temperatures. The pure ODA (curve (a)) produced peaks at 19.3°, 22.3° and 23.3° while the pure PMDA (curve (f)) generated peaks at 14.4°, 16.5°, 20.5°, 22.0° and 25.8°. The ODA(185 °C)/PMDA(190 °C) film (curve (b)) pattern shows peaks due to ODA. In contrast, the ODA(185 °C)/PMDA(200 °C) film pattern (curve (c)) does not contain ODA or PMDA peaks and the ODA(185 °C)/PMDA(210 °C) film pattern (curve (d)) exhibits trace ODA and PMDA peaks. These data indicate inhomogeneous mixing of PMDA and ODA crystals in the films, as verified by SEM observations. The XRD analysis also showed that the optimum evaporation temperatures were 185 °C for the ODA and 200 °C for the PMDA.

Fig. 7 provides SEM images of the film surfaces. The films deposited at a PMDA temperature of 190 °C (image (b)) show very rough surfaces based on aggregations of crystal grains. This morphology is also observed in the case of a PMDA temperature of 210 °C (image (d)). This result can possibly be ascribed to the presence of crystals of unreacted ODA. The films deposited using an ODA temperature of 195 °C (image (e)) evidently contained small crystal grains dispersed in the film matrix. However, the surface profiles for the PAA films deposited at 200 °C (image (c)) are very smooth. On the basis of these SEM observations, as well as the DSC and XRD data, the optimum temperatures for the evaporation of ODA and PMDA were estimated to be 185 and 200 °C, respectively. PAA films deposited using the optimum evaporation temperatures were very smooth, with a roughness of 1.7 nm. The surface roughness did not change after annealing and was in the range of 1.1 to 1.7 nm.
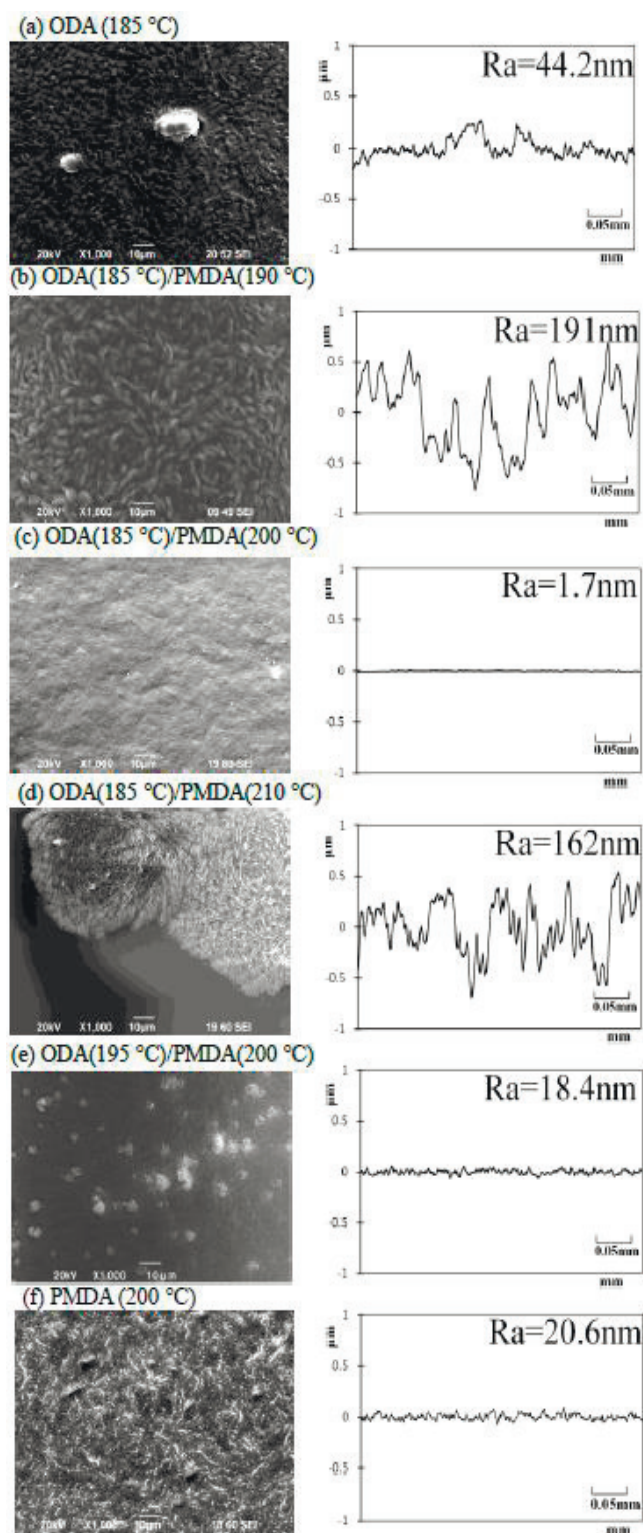
Figure 7. SEM images and surface profiles for films deposited at various PMMA and ODA temperatures.

3.2 Chemical structure of PAA and PI films

The FT-IR spectra acquired from the initial PAA film and films annealed at 200 and 300 °C are shown in Fig. 8, while peak assignments are summarized in Table 4. The PAA film produced a peak at 1540 cm^{-1} (labeled ③) due to the presence of amide groups, and

this peak disappeared after annealing. New peaks appeared at 1775, 1720 and 1370 cm^{-1} (labeled ①, ② and ⑤ attributed to the vibrational modes indicated in Table 3) after annealing. In addition, the magnitude of these peaks increased at higher annealing temperatures. These observations indicate that the imidization reaction proceeded during annealing.
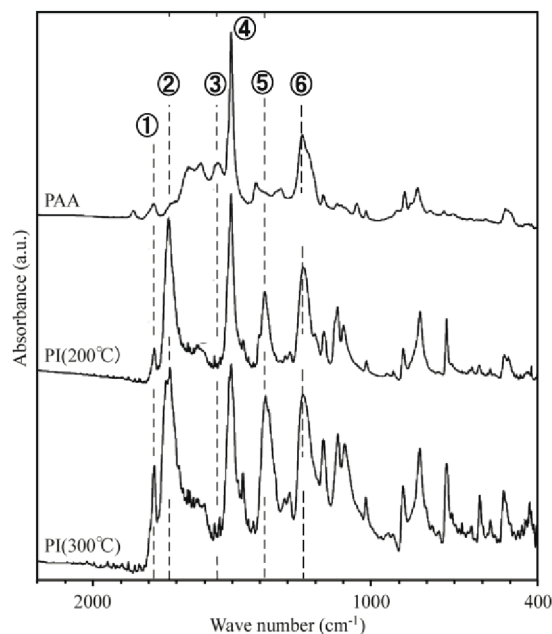
Figure 8. FT-IR absorption spectra of PI films annealed at various temperatures.

Table 4. Vibrational assignments for PAA and PI films.

① 1775 cm^{-1}	imide carbonyl C=O sym. stretching
② 1720 cm^{-1}	imide carbonyl C=O asym. stretching
③ 1540 cm^{-1}	amide N-H (–CONH) bending
④ 1500 cm^{-1}	aromatic ring C=C
⑤ 1370 cm^{-1}	imide C-N-C stretching
⑥ 1240 cm^{-1}	ether C-O-C stretching

3.3 Adsorption of water vapor

Fig. 9 summarizes the adsorption of water vapor on films annealed at various temperatures, as indicated by the frequency change. The amount of water adsorbed is seen to have increased along with the annealing temperature. Increasing the temperature would be expected to promote imidization of the PAA films that would, in turn, reduce the number of hydroxyl groups (that is, hydrophilic groups) in the films.
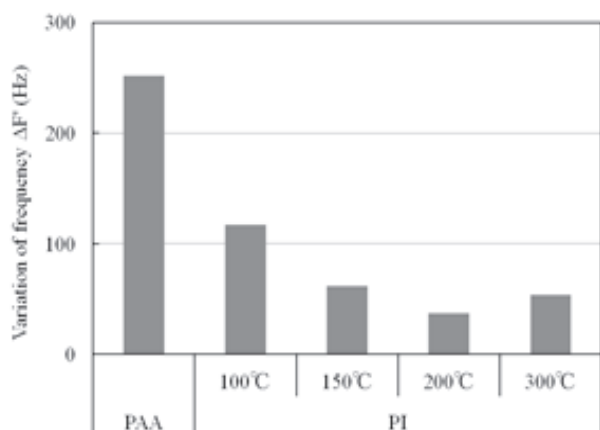
Figure 9. Water vapor adsorption by PAA and PI films prepared using various annealing conditions.

3.4 Surface free energy for the films

Fig. 10 shows the surface free energy for PI films annealed at various temperatures. It is clear that increases in the annealing temperature increased γ_s^d but

Figure 10. Surface free energy for films annealed at various temperatures.

Figure 11. Relationship between water vapor adsorption and polar component of surface free energy.

decreased γ_s^p. As the imidization reaction proceeded, the concentration of polar groups (that is, hydroxyl groups) evidently decreased. The relationship between the amount of adsorption and γ_s^p is shown in Fig. 11, which demonstrates a very good positive correlation between these two variables.

4. CONCLUSION

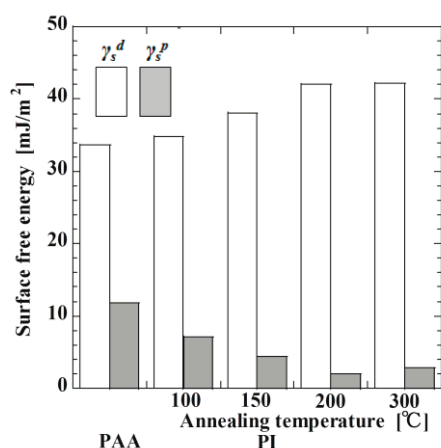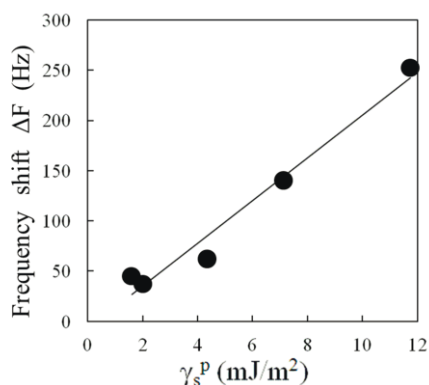Using VDP, PI films were prepared and characterized by SEM, DSC, XRD, FT-IR and surface free energy measurements. The amount of water vapor adsorbed on these films was also measured by means of the QCM method. The optimum temperature for the evaporation of monomers when polymerizing homogeneous PAA films was established. The imidization reaction, that is, a closed ring formation reaction was found to be promoted by annealing of the PAA films, on the basis of FT-IR spectra. Increases in the degree of imidization resulted in decreases in the concentration of polar hydrophilic groups, thus decreasing the magnitude of the polar component of the surface free energy. The results show a good correlation between the polar component of the surface free energy and the amount of water vapor adsorbed.

5. REFERENCES

1. Miyamae T., sukagoshiK. T, Matsuoka O., Yamamoto S. and Nozoye H. / Langmuir, 2001, v. 17, p. 8125-8130.
2. Yamada Y., Tanaka K. and Saito K. / Surface and Coating Technology, 1990, v. 43/44, p. 618.
3. Kito M. and Honda Y. /Thin Solid Films, 1995, v. 271, p. 92-95.
4. Fukushima K., Ikeda Y., Hayashi T., Kikuchi N., Kusano E. and Kinbara A. /Thin Solids Films, 2001, v. 392, p. 254-257.
5. Oya T. and Kusano E. / Vacuum, 2009, v. 83, p. 564-568.
6. Kinbara A., Hayashi T., Wakahara K., Kikuchi N., Kusano E. and Nanto H. / Thin Solid Films, 2003, v. 433, p. 274-276.
7. A. Choukourov, J. Hanus, J. Kousal, Y. Pihosh, D. Slav'inska' and H. Biederman/Vacuum, 2006, v. 81, p. 517-526.
8. Iijima M., Takahashi Y., Inagaki K. and Itoh A. / J. Vac. Sci. Jpn., 1985, v. 28, p. 437.
9. Salem J. R., Sequeda F. O., Duran J., Lee W. Y. and Yang R. M. / Journal of Vacuum Science and Technology, 1986, v. 4, p. 369.
10. Mitchell A., Stephan L. A., Katherine D., Robert C. C. and Anthony G. P. / Journal of Polymer Science, Part A, Polymer Chemistry, 2004, v. 42, p. 5999-6010.
11. Alexander P. G., Thach C. and Mitchell A. /

Chemical Vapor Deposition, 2011, v. 17, p. 141-148.

12. Xiaodong W., Kenji O., Kuniaki T. and Hiroaki U. / Thin Solid Films, 2003, v. 438-439, p. 75-79.

13. Spassova E. / Vacuum, 2003, v. 70, p. 551-561.

14. F Tsai -Y., Alfonso E. L., Harding D. R. and Chen S.H. / Journal of Physics D, Applied Physics, 2001, v. 34, p. 3011-3018.

15. Hu J., Cai H., Ren H., Wei Y., Xu Z., Liu H. and Hu Y. / Industrial and Engineering Chemistry Research, 2020, v. 49, p. 12605-12612.

16. Ayse H. S., Yasin A. and Ayse B. / Journal Applied Polymer Science., 2019, DOI: 10.1002/APP.47616.

17. Xu Y., Chen C. and Li J. / Journal of Chemical and Engineering Data, 2007, v. 52, p. 2146-2152.

18. Peter J. M., Joonsung Y., K. Jennifer Y. and John H. A. / Journal Polymer Science, Polymer Physics, 2012, v. 50, p. 168-173.

19. Kaelble D. H. / Journal of Adhesion, 1970, v. 2, p. 66-81.

20. Sauerbrey G. / Zeitschrift fur Physik, 1959, v. 155, p. 206.

21. Dutt R., Takahashi Y. and Iijima M. / Japanese Journal of Applied Physics., 1999, v. 38, p. L687-L690.

MAGNETIC NANOCOMPOSITES: PREPARATION AND CHARACTERIZATION OF POLYMER-COATED IRON OXIDE NANOPARTICLES

F.V. HAJIYEVA

Baku State University, AZ 1148, Zahid Khalilov, 23

The state of the art is analyzed in the field of preparation and investigation of polymer magnetic nanocomposites based on iron oxide nanoparticles. It has been established that a change in the magnetic properties of polymer nanocomposites depending on the type of polymer matrix can be attributed to the difference in diamagnetic anisotropy of the polymer matrix. It is also shown that the main factors affecting the properties of polymermagnetic materials are associated with long-range forces between nanoparticles and polymer macromolecules, particle surface chemistry and polarity and the interaction between the interfacial polymer layer and nanoscale nanoparticles.

1. INRODUCTION

Recently, interest in a new type of nanocomposite materials, in which the incorporation of nanometer-sized particles into a polymer matrix, has led to unusual magnetic,electrophysical, photoluminescent, superparamagnetic, catalytic and other properties has greatly increased. Polymer nanocomposites based on ferromagnetic nanoparticles are of increased interest, primarily due to the possibility of their use as a medium for recording information with high density, the possibility of implementing highly sensitive sensors of weak magnetic fields and spintronicsdeviceson their basis, as well as the prospects for their use as embedded sources of heterogeneous magnetic field. Therefore, the study of the structure of polymeric magnetic nanocomposites is an actual issue from the point of view of their study.

Composite materials, which consist of ferromagnetic nanoparticles and dielectric matrix, have peculiar physical properties. By varying the chemical composition of the dielectric polymer matrix, the magnetic phase concentration, the process mode, and other system parameters, one can influence such fundamental values as the length of the exchange correlation interaction, the magnetic anisotropy constant, which determine the magnetic properties of the material. Development of methods for the synthesis of polymer nanocompositions with a magnetic component, the study of the mechanism of their formation and stabilization, the study of their structure is of great importance for obtaining new

information about the features of the magnetic properties of a substance in the nanostate.The use of polymeric matrices of different types makes it possible, by changing the conditions of synthesis, to fairly easily and widely regulate the morphology of such systems, namely the size of the particles, the distance between them, and the degree of their aggregation. The wide range of changes in the structural characteristics provides a good opportunity to regulate the magnetic interactions between the nanoparticles and study the influence of these interactions and the size factor on the magnetic properties of nanosystems. The polymer matrix determines the structure of the nanoparticle, ensemble formed in it (size distribution of nanoparticles, the distance between them, their shape, placement order), which, in turn, determines all properties of the nanocomposite itself [1].

The work [2] presents a sonochemical method for obtaining optically active hybrid nanocomposites based on poly (amide imide)/Fe_3O_4 with different content ofFe_3O_4nanoparticles. Previously, the surface of Fe_3O_4nanoparticles was modified with 3-aminopropyl-triethoxysilane. TGA analysis shows an improvement in the thermal stability of nanocomposites compared to the pure poly (amide imide) polymer.

In given work [3], magnetic nanocomposites based on vinyl ester resin and iron oxide nanoparticles (Fe_2O_3) were synthesized. It was found that the functionalization of Fe_2O_3particles using the bifunctional binding agent of methacryloxypropyltri-methoxysilanehas a significant effect on the curing

process and the subsequent physical properties of nanocomposites. The functionalization of the particles favors a composite structure with a lower curing temperature compared to nanocomposites in which unmodified nanoparticles are introduced. TGA analysis showed an enhanced thermal stability in nanocomposites filled with modified nanoparticles compared with composites filled with unmodified particles. It was found that a more uniform dispersion of particles and a chemical bond between the matrix of nanoparticles and vinyl ether contribute to increased thermal stability and increased tensile strength. After the introduction of vinyl ether into the matrix, the nanoparticles become magnetically stable. In work [4] authors describes the magnetic behaviour of polymer nanocomposites containing nanoparticles (10 nm) of maghemite g-Fe_2O_3 and magnetite Fe_3O_4in a polyvinyl alcohol matrix. The compositions were synthesized using an in-situ method, with the formation of oxide taking place inside the polymer matrix itself. Using the magnetic measurements, the single-domain nature of the nanoparticles has been established. Giant negative magnetoresistance was found in highly filled compositions. In the work [5]nanoparticles of Fe_3O_4modified with polyacrylamidein an aqueous solution were obtainedusing in-situ polymerization. The results showed that Fe_3O_4nanoparticles have a superparamagnetic property and superdisperse stability in aqueous solution after modification with polyacrylamide.In [6], acrylic acid and styrene are polymerized with monodispersedFe_3O_4nanoparticles using the graft copolymerization method. Aniline molecules have been linked to Fe_3O_4nanoparticles using electrostatic self-assembly. Monodisperse Ag/ polyaniline/Fe_3O_4nanoparticles, which were obtained using an in situ reduction reaction between emerald PANI and silver nitrate.

In the work [7], nanoparticles of iron oxide (Fe_3O_4) were deposited on the surface of low-density polyethylene (LDPE) particles by the solvothermic method. Nanocompositions based on Fe_3O_4/LDPE, treated with a magnetic field with a vertical direction, showed high thermal conductivity and a large dielectric constant at a low concentration of filler. The increase in thermal conductivity and dielectric constant is associated with the formation of conductive Fe_3O_4circuits in the LDPE matrix under the action of a magnetic field, which can effectively enhance the heat flux and the interfacial polarization of the Fe_3O_4/ LDPE composites. In addition, relatively low dielectric losses and low conductivity are achieved by a low volume fraction of fillers and excellent compatibility between $Fe_3O_4$and LDPE. It

has been established that the dielectric properties of Fe_3O_4/LDPE composites induced by a magnetic field also maintain good stability over a wide temperature range, which contributes to the stability and life expectancy of polymer capacitors. Inwork[8]have been investigated the deposition of magnetic nanocomposite of polymethyl-methacrylate/polypyrrole bilayers from solution using the spin coating method. Using a combination of polymer dissolution and Fe_3O_4nanoparticles coated with a surfactant, the formation of nanocomposites with a uniform dispersion of nanoparticles was demonstrated.In the work [9], nanocomposites based on polyaniline-iron oxide (PANI-Fe_3O_4) were synthesized by increasing the mass content of Fe_3O_4in the presence of PANI. For the synthesis of nanocomposites based on PANI-Fe_3O_4, the mechanical method of mixing the polymer and Fe_3O_4nanoparticles was used. It was found that the band gap of nanocomposites decreases with increasing of concentration of Fe_3O_4nanoparticles. X-ray analysis showed that pure PANI is amorphous. By increasing the concentration of Fe_3O_4, the amorphous nature of pure PANI decreases, and its crystalline nature increases.In the work [10], nanocomposites based on Fe_3O_4magnetic nanoparticles and cellulose polymer acetate were obtained. It was found that Fe_3O_4nanoparticles exhibit ferromagnetic properties with a saturation magnetization of 59 emu/g and a coercivity of 105°C at room temperature. In work [11] presents a new method for the chemical modification of Fe_3O_4nanoparticles with polymerizable groups. After the synthesis of Fe_3O_4nanoparticles by the co-precipitation method, they were sequentially modified with 3-aminopropyl-tri-ethoxysilane, acryloyl chloride and benzoyl chloride. Then the modified magnetite nanoparticles with unsaturated acrylic groups were copolymerized with methyl methacrylate, butyl acrylate and acrylic acid by means of mini-emulsion polymerization. A number of magnetic nanocomposites containing different amounts of Fe_3O_4nanoparticles (0-10 wt.%) with a core-shell structure have a diameter of less than 200 nm and exhibit superparamagnetic properties.In work [12], new, magnetic polyurethanenanocomposites were synthesized by incorporating surface-modified iron oxide nanoparticles with n-(2-aminoethyl)-3-aminopropyltri-methoxy-silane. The obtained data showed significant improvements in the thermal as well as magnetic properties of nanocomposites, in the case where nanoparticles were incorporated into the polymer matrix.In work [13] the magnetic behavior of polymer nanocompositescontaining of Fe_3O_4

nanoparticles (10 nm) in a polyvinyl alcohol matrix was studied using Mössbauer transmission and Conversion-Electron spectroscopy and magnetic measurements. The results show that the concentration of Fe_3O_4nanoparticles in the volume of the polymer matrix significantly affects the magnetic properties of nanocomposites. Have been determined that the lamellar distribution of superparamagnetic islands of Fe_3O_4leads to the formation of magnetic anisotropy in the films. In work [14]were prepared two types of materials: grafted, crosslinked and plasticized, polyethylene chloride (PVC) based and magnetic polymer nanocomposites. Precursor solutions or plastisols used to produce plastic films were obtained by mixing PVC in the form of a polymer matrix, di (2-ethylhexyl) phthalate as a plasticizer, Ca/Zn salts as a heat stabilizer and at low concentrations a crosslinking agent, 3-mercaptopropyltrimethoxysilane or 3-aminopropyl tri-ethoxysilane. Flexible films were obtained from plastisols using static casting. Magneto-polymer nanocomposites were obtained by mixing the optimal composition of plastisols with ferrofluid based on magnetite (Fe_3O_4) and di (2-ethylhexyl) phthalate. Plastic films were obtained by static casting of plastisol /ferrofluidic systems.

In recent years, magnetic nanoparticles have been proposed for use as biomedical purposes.In work [15] investigated superparamagneticFe_3O_4nanoparticles (SPIONs) coated with acetylated PAMAM dendrimers. In this study, conjugated (As-PAMAM)/Fe_3O_4nanoparticles were studied as controlled release systems for parenteral administration of model drug 5-aminosalicylic acid (mesalamine) and analyzed using various kinetic release studies.

In work [16] nanocomposites based on poly (vinylidenefluoride) (PVDF) and magnetite nanoparticles were prepared. The structure and content of nanocomposite materials were studied by using scanning electron microscope, atomic-force microscope and X-ray diffraction. Magnetic properties of PVDF+Fe_3O_4nanocomposites have been studied upon increasing nanoparticle content in polymer matrix up to 20% revealing superparamagnetic behavior as Fe_3O_4 nanoparticles in polymer matrix act out like single-domain particles. It has also been observed that PVDF+Fe_3O_4 based nanocomposites can absorb the electromagnetic waves in the high frequency range 0,1-30 GHz. It has been shown that the absorption of high frequency radio waves by PVDF+Fe_3O_4nanocomposites can be explained by the different molecular structures and also by the

scattering of the radio waves at the boundary of nanoparticle-polymer matrix.In work [17]the effect size distribution of magnetite nanoparticles in a PVDF matrix on the magnetic properties of PVDF+Fe_3O_4nanocomposites was experimentally and theoretically investigated. The size distribution of nanoparticles in polymer matrix and morphology of the nanocomposites were studied by the means of scanning electron microscopy and atomic-force microscopy. It was found that when the Fe_3O_4nanoparticles are introduced into the polymer matrix, their coagulation takes place. The increase in the size of the particles depends on their concentration in the polymer matrix, the type of polymer (polar, non-polar, its viscosity, etc.), reaction the oxidation of the surface layer of particles occurs and the magnetite size decreases. Consequently, the reduced magnetic properties may also be observed. The hysteresis loops have been recorded in small magnetic field range. It was found that the magnetic hysteresis parameters depend on the size and concentration of Fe_3O_4nanoparticles. Theoretical calculations were compared with experimental results obtained from M(H)measurements. The reasons of differences between theoretical and experimental results have been explained.

In work [18] have been investigated the influence of an external permanent magnetic field on electrical resistivity and dielectric permittivity of PP+Fe_3O_4 and PVDF+Fe_3O_4 based nanocomposites. It was found that independentof the type of polymer the electric resistivity of magnitoresistive effect has been observed. Investigation of MR in PP+Fe_3O_4 and PVDF+Fe_3O_4 based nanocomposites showed that at room temperature the concentration dependence of MR is identical for both systems. However, the electrical resistance of the PVDF+Fe_3O_4 based nanocomposite was found to reduce strongly in comparison with that of the nanocomposite based on PP+Fe_3O_4 under the influence of a magnetic field. This could be explained by the fact that the diamagnetic anisotropy and the charge carriers' density of these polymers are quite different from each other. Negative magnetoresistance of composite films with ferromagnetic nanoparticles incorporated in dielectric matrix is due to the tunneling transitions of electrons between neighboring nanoparticles. Decrease on dielectric permittivity under a magnetic field is consistent with negative magnetoresistive effect.

In work [19]have been reported about the preparation of magnetic polymer nanocomposites on the basis of isotactic polypropylene and magnetite Fe_3O_4nanoparticles. The structure and composition of

polymer nanocomposite materials have been studied by scanning electron microscopy, atomic-force microscopy and X-Ray dispersive analysis. The magnetic properties of polymer nanocomposites based on PP+Fe_3O_4 have been investigated. It is found that not significant adhesion and agglomeration of nanoparticles occur, by increasing the nanoparticle content in polymer matrix up to 40% and therefore they act as single-domain nanoparticles. The samples of nanocomposites based PP+$Fe_3O_4$are able to absorb ultrahigh frequency electromagnetic waves in the frequency range from 0,1 to 30 GHz. The increase in Fe_3O_4concentration from 5 to 40% at the 400 mkm thickness of the films leads to an increase in absorption of electromagnetic waves of high frequency from 15 to 22,7%.

2. CONCLUSION

Therefore, based on the above literature data, the following conclusions can be made that a change in the magnetic properties of polymer nanocomposites depending on the type of polymer matrix can be attributed to the difference in diamagnetic anisotropy of the polymer matrix. It is also shown that the main factors affecting the properties of magnetic polymeric materials are associated with long-range forces between nanoparticles and polymer macromolecules, particle surface chemistry and polarity, and the interaction between the interfacial polymer layer and nanoparticles.

3. REFERENCES

1. Nicolais L., Carotenuto G. (ed.). Metal-polymer nanocomposites. – John Wiley & Sons, 2004.
2. Rafiee Z., Panji Z. / Synthesis and characterization of optically active magnetic PAI/Fe_3O_4nanocomposites Amino Acids p.1-6, Open access, 2018
3. Guo, Z., Lei, K., Li, Y., Ng, H. W., Prikhodko, S., & Hahn, H. T. / Fabrication and characterization of iron oxide nanoparticles reinforced vinyl-ester resin nanocomposites. Composites Science and Technology, 2008, 68(6), p.1513-1520.
4. Yu. Godovsky, D., Varfolomeev, A. V., Efremova, G. D., Cherepanov, V. M., Kapustin, G. A., Volkov, A. V., & Moskvina, M. A. / Magnetic properties of polyvinyl alcohol-based composites containing iron oxide nanoparticles. Advanced Materials for Optics and Electronics, 1999, 9(3), p.87-93.
5. Tong, R., Wang, Y., Yang, G., Ma, A., Sun, K., Yang, H., & Wang, J. / Study of preparation and properties on polymer-modified magnetite nanoparticles. South African Journal of Chemistry, 2015, 68(1), p.99-104.
6. Bian, L., Bao, L., Wang, J., & Lei, J. / In situ preparation of monodispersed Ag/polyaniline/Fe3O4 nanoparticles via heterogeneous nucleation. Nanoscale research letters, 2013, 8(1), p.309.
7. Qingguo Chi, Tao Ma, Jiufeng Dong, Yang Cui, Yue Zhang, Changhai Zhang, ShichongXu, Xuan Wang, Qingquan Enhanced thermal conductivity and dielectric properties of iron oxide/polyethylene nanocomposites induced by a magnetic field Scientific reports 7:3072, Published online, 2017.
8. Gass, J., Poddar, P., Almand, J., Srinath, S., & Srikanth, H. / Superparamagnetic polymer nanocomposites with uniform Fe_3O_4 nanoparticle dispersions Adv. Funct. Mater. 2006, 16, p.71–75.
9. Dhachanamoorthi, N., Chandra, L., Suresh, P., & Perumal, K. / Facile Preparation and Characterization of Polyaniline-iron Oxide Ternary Polymer Nanocomposites by Using" Mechanical Mixing" Approach. Mechanics, Materials Science & Engineering MMSE Journal. Open Access, 2017, p.9.
10. Jalajerdi R., GholamianF.,ShafieH., MoravejiA., Ghanbari D. Thermal and magnetic characteristics of cellulose acetate-Fe_3O_4. JNS 2 (2012), p.105-109
11. Mahdieh, A., Mahdavian, A. R., & Salehi-Mobarakeh, H. / Chemical modification of magnetite nanoparticles and preparation of acrylic-base magnetic nanocomposite particles via miniemulsion polymerization. Journal of Magnetism and Magnetic Materials, 2017, 426, p.230-238.
12. Nikje, M. M. A., Noruzian, M., & Moghaddam, S. T. / Investigation of Fe_3O_4/AEAP supermagnetic nanoparticles on the morphological, thermal and magnetite behavior of polyurethane rigid foam nanocomposites Polimery, 2015, 60, №1, p.26-32.
13. Novakova A.A., Lanchinskaya V.Yu., VolkovA.V., Gendler T.S.,KiselevaT.Yu., Moskvina M.A., Zezin S.B. / Magnetic properties of polymer nanocomposites containing iron oxide nanoparticles Journal of Magnetism and Magnetic Materials volume, 2003, 258–259, p.354–357.
14. Oliverio S.Rodrıguez-Fernandez, C.A.Rodrıguez-Calzadıaz, IsauraG.Yarnez-Flores, Sagrario M.Montemayor / Preparation and characterization of a magneto-polymericnanocomposite: Fe_3O_4nanoparticles in a grafted, cross-linked and plasticized poly(vinyl chloride) matrix Journal of Magnetism and Magnetic Materials 2008, 320, p.81–84.

15. Saboktakin M. R., Maharramov A. and Ramazanov M. A. / Synthesis and characterization of MRI-detectable magnetic dendritic nanocarriers Polymer-Plastics Technology and Engineering, 2010, 49, p.104–109.

16. Ramazanov M.A., Hajiyeva F.V., Shirinova H.A., Mamedov H.M. / The relation between the composition, structure and absorption properties of ultra-high frequency radio waves of poly(vinylidene fluoride)/magnetite nanocomposites International Journal of Modern Physics B, 2019, 33(10), p.1950083

17. Ramazanov M.A., Maharramov A.M., Ali-zada R.A., Shirinova H.A., Hajiyeva F.V. / Theoretical and experimental investigation of the magnetic properties of polyvinylidene fluoride and magnetite nanoparticles-based nanocomposites Journal of Theoretical and Applied Physics, 2018, 12(1), p.7-13.

18. Ramazanov M.A., A.M Maharramov, Luca Di Palma, Shirinova H.A., Hajiyeva F.V., M.R.Hasanova / Negative magnetoresistance of polymer nanocomposites on the basis of $PP+Fe_3O_4$ and $PVDF+Fe_3O_4$ in the magnetic field Journal Ferroelectrics, 2018, 537 (1), p.191.

19. Ramazanov M.A., HajiyevaF.V., MaharramovA.M., Luca Di Palma, Diana Sannino, Makoto Takafuji, MammadovH.M., HasanovaU.A., ShirinovaH.A., Bayramova Z.A. / New magnetic polymer nanocomposites on the basis of isotactic polypropylene and magnetite nanoparticles for adsorption of ultrahigh frequency electromagnetic waves polymer-plastics technology and engineering, 2018, 57 (5), p.449-458.

EFFECT OF pH ON NITRATES REDUCTION BY BIMETALLIC NANOPARTICLES

G.G. VALIYEVA

Baku State University, Department Ecological Chemistry, Ecology and Soil science faculty,

AZ1148, Baku, Azerbaijan

In this paper was investigated the pH effect of nitrate reduction in water by bimetallic nanoparticles on the base Fe/Ni,Fe/Pd, Fe/Cusynthesized byborohydride reduction method.The parameter investigated was the reaction pH (unbuffered, pH 3, pH 10 and fixed pH 3). It was found that the total nitrate removal after 15 min of reaction at concentration of bimetallic nanoparticles equal to 0.1 g/Lwas determined by fixing acidic conditions. The alkaline pH conditions stopped the reduction process and the nitrate removal was equal to 10-14%. Also was evaluated the initial and final pH of reactions. It was investigated that the all nitrate reduction reactions with bimetallic nanoparticles stopped at pH 8 at room temperature, cause of alkalization.

1. INRODUCTION

Different studies on nitrate reduction by various substances were reported till now [1,2]. Based on the fact that nitrates are very soluble, they are reported as one of the major contaminants. Nitrates accumulate in groundwater, subsequently in human body and lead several of health outcomes, like methemoglobinemia, birth defects, cancer and etc. The high concentration of nitrates in groundwater also generates serious environmental problems. The main sources of nitrates associate with several human exposure, such as agricultural fertilizer application, septic tanks, animal farming, industrial wastewater, residuals. Nitrate from these sources can easily reach groundwater and as a consequence drinking water too. Ecological monitoring of groundwater has shown a high nitrates contamination in agricultural regions, due to fertilizers application and animal farming [7]. For these reasons was determined the MCL of nitrates in drinking water as 50 mg NO3-/L [10].

For nitrates removal from groundwater were used a number of various methods. But chemical reduction has more attention, due to fast reaction rate and cost-effectiveness [11]. While various techniques such as the ion exchange, reverse osmosis, electrodialysis and biological denitrification have proved highly effective in the removal of nitrate contaminants, they cannot be employed in largescale water treatment plants due to their high energy consumption, technological complexity, nitrate brine concentration and secondary pollution by bacteria or other organic substrates [14].

In the previous studies has shown the effectiveness of bimetallic nanoparticles in nitrate reduction reactions. NZVI supplemented with the secondary metal is a new technique for nitrate removal, which enhances the catalytic reactivity through hydrogenation. Secondary metal also enhances reaction rate. In order to improve the nitrate removal, various bimetallic nanoparticles were tested in the previous studies [12, 13].

Using another metal catalyst such as Ni, Pt, Pd, and Cu increase the reactivity of NZVI for many times. However, a lot of studies about reducing nitrates from wastewater with bimetallic nanoparticles have been systematically reported. In previous study the effect of selected concentrations of bimetallic nanoparticles was investigated and the optimal concentration was determined as 0.2 g/L. By using this amount of nanoparticles the total removal of nitrates was achieved after 15 minutes. It was clear that pH plays a main role in the effectiveness of nitrate reduction. In this study additional tests were conducted at different initial pH values (3, 3 fixed and 10) by using 0.1 g/L of bimetallic nanoparticles to assess the operating conditions that maximized nitrate removal.

2. EXPERIMENTAL

Bimetallic nanoparticles were synthesis in a flask reactor with three open necks. Nanoscale bimetallic particles were synthesized according to a widely known method. To avoid the agglomerating, sodium oleate was used during synthesis. Bimetallic nanoparticles were prepared by mixing 0.1M Fe^{3+} solution with 0.5M solution of sodium oleate. This solution was mixed on a magnetic stirrer at 500 rpm. After 15 min, the second metal was added into the solution. On the other hand, 100 ml of 0.3 M sodium borohydride solution was prepared and added into the above solution drop by drop and stirred. All the reaction was at room temperature and in a free oxygen atmosphere under nitrogen gas. After 10 minutes sodiumborohydride solution was added to the first prepared mixture. The appearance of black particles starts by adding the first drop of borohydride solution. The final solution with black bimetallic nanoparticles was washed 3 times with ethanol and used for nitrates reduction process.

A nitrate solution was prepared by dissolving amount of $NaNO_3$ in distilled water for getting a high nitrate polluted solution (300 mg/L). The batch experiments were performed with early determined optimal concentration of bimetallic nanoparticles for investigation the pH effect (0.2 g/L).

Batch experiment was performed by adding freshly prepared various bimetallic nanoparticles to nitrates polluted solution (300 mg/L) with different selected initial pH (3, fixed 3, 10, unbuffered). After 15 minutes the reaction was stopped and the final concentration of nitrate and nitrite were determined by ion chromatography (Dionex ICS - 5000).

3. RESULTS AND DISCUSSION

The results shown in Fig. 1 confirmed the effect of pH on nitrate reduction process. The treatment of nitrate solution at pH 10 stopped the reaction and the total removal was determined as 14.41, 11.48, 10.88% by using bimetallic nanoparticles FeNi, FePd, FeCu, consequently. Regarding the test which was performed at the initial pH of 3, the removal was 59.34, 54.54, 49.62%, then the reaction stopped. This evaluation is similar with unbuffered conditions, when the nitrates removal stopped after 57, 51.64, 48.69% for nanoparticles FeNi, FePd, FeCu. Unbuffered solution test was conducted by leaving it in its normal pH during the reaction.
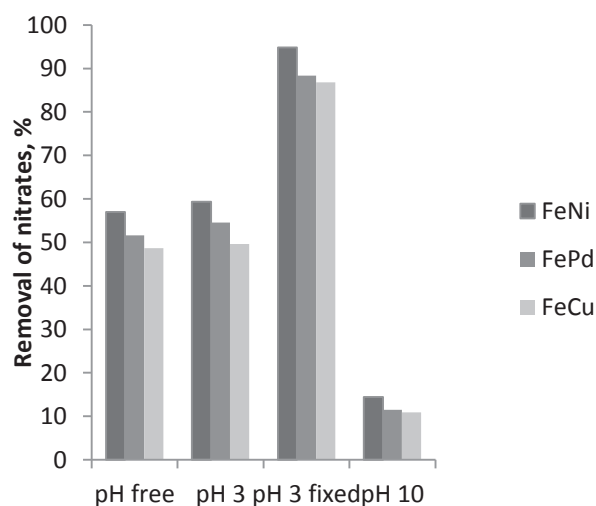

Figure 1. Nitrate removal by various bimetallic nanoparticles (FeNi, FePd, FeCu) at different pH condition. Condition: T= 298 K; 0.1 g/L bimetallic nanoparticles and [NO3-]= 300 mg/L.

The solution had an approximately neutral initial pH and final pH was evaluated as 8-9, as shown in Fig 2. These evaluations suggest that for increasing treatment efficiencies it is necessary to maintain pH in acidic conditions.
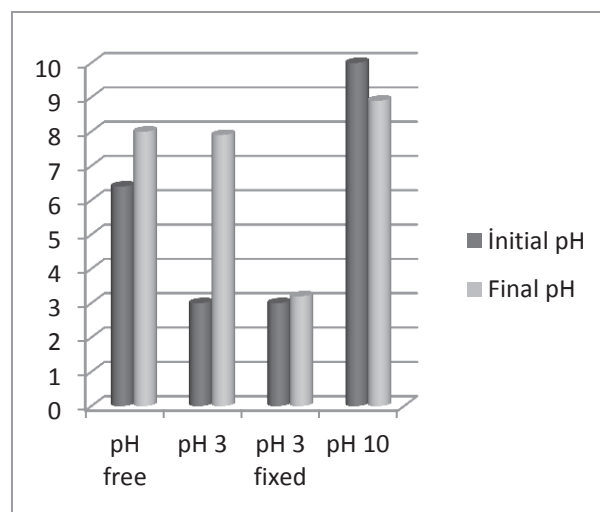
Figure 2. Evaluation of initial and final pH condition during treatment process.

To confirm that alkaline pH condition stopped the nitrate reduction process, additional tests were performed by maintaining a fixed 3 pH condition. As shown in Fig 1, the best removal efficiency was achieved by using fixed acidic conditions (94.85, 88.35, 86.83%, consequently). By comparison the reactions with initial pH 3 and fixed pH 3, it is possible to say that the alkalization of the solution lead a strong limitation of the reduction process. The best removal (86 – 95%) was recorded at acidic

55

condition and decrease (10 -14%) at alkaline pH (approximately at pH 10).

According to these results, the minimization of the bimetallic nanoparticle concentration can be achieved by fixing the pH at 3 and getting total removal.

4. CONCLUSIONS

Bimetallic nanoparticles on the base Fe/Ni, Fe/Pd, FeCu were synthesized in the presence of sodium oleate substance by borohydride reduction method undernitrogen conditions at room temperature. It was found that in the presence of acidic medium bimetallic nanoparticles were more effective for nitrate removal. It means that the efficiency of reaction strongly depend onpH.The alkaline conditions were occurred after 15 minutes of reaction and stopped the reduction process at pH around 8.

5. REFERENCE

1. Nasrabadi, H. T., Abbasi, E., Davaran, S., Kouhi, M., &Akbarzadeh, A./ Bimetallic nanoparticles: Preparation, properties, and biomedical applications. Artificial Cells, Nanomedicine, and Biotechnology, 2014, 44(1), p.376–380

2. Sharma, G.; Gupta, V.K.; Agarwal, S.; Kumar, A.; Thakur, S.; Pathania, D. / Fabrication and characterization of Fe@MoPO Nanoparticles: Ion exchange behavior and photocatalytic activity against malachite green. J. Mol. Liq. 2016, 219, p.1137–1143.

3. Tratnyek P.G., Scherer M.M., Johnson T.J., Matheson L.J./ Permeable reactive barriers of iron and other zero-valentmetals,In: M.A. Tarr (Ed.), Chemical Degradation Methods forWastes and Pollutants: Environmental and Industrial Applications, Marcel Dekker, New York, NY, 2003, p. 371–421.

4. Mossa Hosseini S., Ataie-Ashtiani B., Kholghi M./ Nitratereduction by nano-Fe/Cu particles in packed column,Desalination 2011, 276, p.214–226

5. Tie Li., Farrell J./ Reductive dechlorination of trichloroetheneand carbon tetrachloride using iron and palladized-ironcathodes, Environ. Sci. Technol., 2000, 34, p.173–179.

6. Liou Y.H., Lo S.L., Lin Ch.J., Kuan W.H., Weng Sh.Ch./ Chemical reduction of an unbuffered nitrate solution usingcatalyzed and uncatalyzednanoscale iron particles, J. Hazard.Mater. 2005, 127, p.102–110.

7. Santos, F. S., Lago, F. R., Yokoyama, L., & Fonseca, F. V./ Synthesis and characterization of zero-valent iron nanoparticles supported on SBA-15. Journal of Materials Research and Technology, 2017, 6(2), p.178–183.

8. Yuvakkumar R., Elango V., Rajendran V., Kannan N./ Digest Journal of Nanomaterials and Biostructures 2011, 6, 4, p. 1771-1776.

9. Sparis, D.; Mystrioti, C.; Xenidis, A.; Papassiopi, N. / Reduction of nitrate by copper-coated ZVI nanoparticles. Desalination and Water Treatment 2013, 51, p.2926–2933.

10. Torabian, A.S.; Hassani, A.; Abedi, S.M./ Comparing reverse osmosis and ion exchange methods of nitrate elimination. J Environ SciTechnol 2006, 8 (3), p.8-21.

11. Zumft, W.G. / Cell biology and molecular basis of denitrification. Microbiol. Mol. Biol. Rev. 1997, 61, p.533–616.

12. Kim, Y.H.; Hwang, E.D.; Shin, W.S.; Choi, J.H.; Ha, T.W.; Choi, S.J. Treatments of stainless steel wastewater containing a high concentration of nitrate using reverse osmosis and nanomembranes. Desalination 2007, 202, p.286–292.

13. Valiyeva G.G., Bavasso I., Di Palma L., Hajiyeva S.R., Ramazanov M. A., Hajiyeva F.V. / Synthesis of Fe/Ni Bimetallic Nanoparticles and Application to the Catalytic Removal of Nitrates fromWater. Nanomaterials 2019, 9, p.1130

14. Guo, J.; Guo, P.; Yu, M.; Sun, Z.; Li, P.; Yang, T.; Liu, J.; Zhang, L. / Chemical Reduction of Nitrate Using Nanoscale Bimetallic Iron/Copper Particles. Pol. J. Environ. Stud. 2018, 27 (5), p. 2023-2028.

15. Kumar M., Chakraborty, S. / Chemical denitrification of water by zero-valent magnesium powder. Journal of Hazardous Materials 2006, 135(1-3), p.112–121.

16. Murphy, A.P. Chemical removal of nitrate from water. Nature 1991, 350, p.223–225.

17. Sohn, K. Kang, S.W. Ahn, S. Woo, M. Yang, S.K. / Fe (0) nanoparticles for nitrate reduction: stability, reactivity, and transformation. Environ. Sci. Technol. 2006, 40, p.5514-5519.

PECULIARITIES OF BIOECOLOGY OF BULBULA LAKE OF THE ABSHERON PENINSULA

N.A. SADIGOVA, S.G. JAFAROVA, A.Sh. ABBASOV, M.A. BAHADDINOV

Faculty of Ecology and Soil Science, Baku State University, Baku, Azerbaijan, AZ 1148, Z.Khalilov.

It is known that passes through Azerbaijan is one of the most powerful in Eurasia migratory bird routes from Eastern Europe and Western Siberia to the South East and South-West Africa and back. The lakes of Absheron attracted migrant birds with optimal conditions: the winter is mild, the lakes on which waterfowl overwinter, do not freeze, and a lot of food. The state of "dying lakes" and, in particular, Bulbula Lake, the fauna and flora of the lake and surrounding areas are discussed in this article. The main focus is on migratory birds, the most important routes of which pass through Azerbaijan. The data on the nature of the birds registered in the lake, their biotopic distribution from the surface of the lake, food processing features, population data, as well as the conservation status are given.

1. INTRODUCTION

Absheron, figuratively speaking, is the "land of lakes" which are the most important components of the nature of the peninsula. There are over 200 lakes on Absheron, among which there are a lot of large ones that make up several square kilometers and small ones of only 100 m^2 in size. Some lakes are on the "verge of extinction". Human tears away from the nature part by part of these biotopes, which serve as a source of life for many organisms of different taxonomic ranks.But as we have noted, many lakes where waterfowl have found "shelter" are in a disastrous state as a result of human activities.

2. EXPERIMENTAL

According to the three-year research plan "Ecological monitoring of flora, fauna and soil of Absheron reservoirs and surrounding territories" of the department of "Bioecology", in the autumn of 2018 and in the winter of 2019, trips were made to Bulbula Lake.

The lake is located 10-12 km east of Baku, at a height of 8 m above sea level. The area of the mirror is 0.7 km^2. The maximum width is -360 m, the maximum depth is -1.5 m, the length of the coastline is 6 km [1]. Anthropogenic runoff dominates in the lake feeding. Since the reservoir is characterized an intense bloom of blue-green algae.

Due to the strong fluctuations in the water level, higher aquatic vegetation is found in single specimens. In the lake, 70 species of organisms were found, among which, by the number of species, chironomids dominate in phytoplankton (18 species) [2].

The lake is polluted with oil and oil products (1.5 -14 MPC), phenols (3-32 MPC), detergents (up to 2 MPC), SALW (3-4 MPC) [3,4]. Despite, we are not afraid to note, the dying of the lakes, monitoring showed that the birds still visit it.

Research on the lake and the surrounding areas have made it possible to determine the taxonomic composition of birds, aquatic and semi-aquatic ecological groups of animals and plants, a soil was taken for the determination of soil organisms. For observations were used binoculars and telescopes.The definitions were carried out by identifiers of birds [5,6], of plants [7], of soils [8].

3. RESULTS AND DISCUSSION

The following table provides information on the systematic taxonomy of birds registered on the territory of Bulbula Lake.

Thus, 9 species were marked during the wintering, of which 3 species come to nest.Numerous wintering species are the Common Pochard (*Aythya ferina*)(80 individuals) and the Tufted Duck (*Aythya fuligula*)(100 individuals). Red Book species –White-headed Duck(*Oxyura leucocephala*)very rare, but up to 33 individuals were counted on the lake.

Table. The systematic taxonomy of birds registered on the territory of Bulbula Lake

Order	Family	Species	By the nature of stay
Podicipediformes	*Podicipedidae*	*Podiceps nigricollis*	Sedentary
-	-	*Tachybaptus ruficollis*	Wintering
Ciconiiformes	*Ardeidae*	*Árdea cinérea*	Sedentary
-	-	*Egretta garzetta*	On breeding
Ansoriformes	*Anatidae*	*Aythya ferina*	Wintering
-	-	*Oxyura leucocephala*	On nesting
-	-	*Aythya fuligula*	Wintering and span
-	-	*Anas clypeata*	Wintering
Gruiformes	*Rallidae*	*Rallus aquaticus*	Sedentary
-	-	*Gallinula chloropus*	Sedentary
-	-	*Fulica atra*	Sedentary
Charadriiformes	*Accipitridae*	*Falco tinnunculus*	Sedentary
-	-	*Circus alruginosus*	Sedentary
-	-	*Accipiter nisus*	Sedentary
-	*Laridae*	*Chroicocephalus ridibundus*	Sedentary
-	-	*Larus cachinnans*	Winters and nests
Columbimorphae	*Columbidae*	*Columba livia*	Sedentary
-	-	*Streptopelia decaocto*	Sedentary
Passeriformes	*Corvidae*	*Corvus frugilegus*	Sedentary
-	-	*Corvus cornix*	Sedentary
-	*Turdidae*	*Panurus biarmicus*	Sedentary
-	*Paridae*	*Remiz pendulinus*	Sedentary
-	*Sturnidae*	*Sturnus vulgaris*	Sedentary
-	*Troglodytidae*	*Troglodytes troglodytes*	Sedentary
-	*Sylviidae*	*Phylloscopus collybita*	Sedentary
-	*Turdidae*	*Turdus merula*	Sedentary
-	*Motacillidae*	*Motacilla flava*	On the span
-	*Motacillidae*	*Motacilla alba*	On the span
-	*Fringillidae*	*Fringilla coelebs*	Nesting
-	*Passeridae*	*Passer domesticus*	Sedentary
-	-	*Passer hispaniolensis*	Sedentary

As is known, all ducks are divided into two large groups - noble or river ducks and diving ducks [9]. Of the group of river ducks on the lake, only *Anas clypeata* was registered. The diving ducks are represented by the Common Pochard (*Aythya ferina*), *Aythya fuligula* and *Oxyura leucocephala*. A certain regularity is noted in the distribution of birds along the surface of the lake.

The diving ducks are kept in open water, they were not in the reeds. The *Anas clypeata*is more tied to the thickets, especially in shallow waters.

In literary sources [10] there is evidence that only 10 -15% of all ducks are kept in reeds and up to 25% in reeds in and around the shallow waters. *Tachybaptus ruficollis* also prefer areas of the reservoir with dense thickets of reeds and other plants.The open areas of the reservoir are preferred by the Water rail (*Rallus aquaticus)*, usually a night bird, but in winter it is also active during the day; in danger, it hides in thick grass [9]. In the thickets of reeds marked Common Moorhen (*Gallinula chloropus*) and Eurasian coot (*Fulica*

atra). The Little Egret (*Egretta garzetta*)and the Gray Egret (*Ardea cinerea*)are encountered in the "littoral zone" of the lake.

Of falcons in the vicinity of the lake we observed the *Circus alruginosus*, the *Falco tinnunculus*and the *Accipiter nisus*. Of these, only the Western marsh harrier (*Circus alruginosus*), as if justifying its name, is marked in the thickets of reeds (6 individuals).

In the thickets of reeds along the bank of the lake we marked *Corvus frugilegus, Remiz pendulinus*, and along the coast were *Motacilla flava* and *Motacilla alba*. Although the *Fringilla coelebs* is numerous in all forests, but it constantly flew around the lake.

Number. Above, we noted that numerous wintering species are *Aythya fuligula*and *Aythya ferina*; then *Tachybaptus ruficollis*(50 individuals), *Gallinula chloropus*(30 individuals), *Oxyura leucocephala* (33 individuals), *Larus cachinnans* (18 individuals), *Turdus merula* (12 individuals), *Motacilla alba*(11 individuals), *Circus alruginosus* (6 individuals), *Phylloscopus collybita*(4 individuals), *Fringilla coelebs* (6 individuals), *Árdea cinérea*, *Egretta garzetta, Panurus biarmicus*,*Remiz pendulinus*,*Motacilla flava* and *Falco tinnunculus*- 2 individuals each.

The *Fulica atra* (275 individuals), the *Chroicocephalus ridibundus*(250 individuals), the *Corvus frugilegus*, the *Corvus cornix*, the *Sturnus vulgaris*, the *Passer domesticus* and *Passer hispaniolensis*were very numerous. The interest was caused by their number White-headed Duck (*Oxyura leucocephala*) - the Red Book species.

Categories and status.White-headed Duck (*Oxyura leucocephala*) - red-book species with the status EN, Common Pochard (*Aythya ferina*)- with the status - YU, other species are assigned the status LC.

For the purification of Absheron lakes, Netherlands company Witten Bos has developed by technical - economic feasibility study for the rehabilitation of 9 lakes of the Absheron peninsula. It will cost an average of 500 million manat. Of these, the cost of BulbulaLake by average can reach 17.5 million manat.

4. CONCLUSION

31 species of birds belonging to 8 detachments are registered on Bulbula Lake. The most numerous species are representatives of the passerine order.Wintering marked 9 species, of which 4 species arrive at the nesting. Red Book speciesare a White-headed Duck (*Oxyura leucocephala*) with EN status; Common Pochard (*Aythya ferina*) - VU status; the remaining ducks have LC status. Of the registered species, 21 are sedentary.

5. REFERENCES

1. Mamedov V.A. et al. / Environmental monitoring of the coast of Greater Baku and Sumgayit. Baku, 1999, p.90
2. Aliyev R.I. et al. / Biodiversity of some lakes of the Absheron Peninsula. Baku State University, Institute of Geology and Geophysics of the National Academy of Sciences of Azerbaijan, 2016, p.10-15
3. Alekperov A.B. / Absheron: problems of hydrogeology and geoecology. Baku, 2000, 190 p.
4. Sibac.info/shutcot/natur/xxx/4316
5. Mustafayev G.T. et al. / Birds of Azerbaijan. Chashioglu, 2005, p.77-115
6. Vtorov P.P. et al. / The determinant of birds of the fauna of the USSR. Moscow Enlightenment, 1980, p.15-82
7. Flora of Azerbaijan: guideline / red. D.I. Sosnovsky, I.I. Karyagin. Baku: Publishing House of the Academy of Sciences of the AzSSR, 1950, v.1, p.221.
8. Arinushkina E.V. / Manual on chemical analysis of soil. Moscow University Press, 1970, p.488
9. Sultanov E.G ./ Charadriiformes. In the book "Animal World of Azerbaijan" 2000,v.III, p.315-320
10. Mustafaev G.T. / Falconiformes. In the book "The fauna of Azerbaijan", 2000, p.292-294.

Recently, intensive research has been conducted in developed countries to study the physical, chemical and biological processes occurring in low-dimensional systems. At Baku State University, which celebrated its 100th anniversary, multidisciplinary research is conducted. These studies cover a number of areas of science and technology, and the results of these studies have made a major contribution to fundamental research and have great practical value in technology, medicine, oil industry, ecology, agriculture, and the military. BSU "Modern Trends in Physics" conference of Baku State University also discusses multidisciplinary research work of university scientists with foreign scientists and is highly appreciated by the international community. This conference, held in 2019, was dedicated to the 100th anniversary of Baku State University, and its materials are also indexed in the Web of Science Clarivate Analytics system. Journal of Low Dimensional Systems, which has been published at BSU since 2017, has also gained international recognition within a short time and has published serious scientific articles on condensed environment and materials science.

On behalf of the editorial team of the Journal of Low Dimensional Systems and the authors of articles published in the journal, I congratulate the staff of Baku State University on its 100th anniversary and wish the scientists of the team great scientific success.

The Deputy Editor-in-Chief: Professor Mahammadali Ramazanov

Address:
Az1148, Z.Khalilov str. 23,
Baku State University, Baku, Azerbaijan

E-mail: lemanabdullayeva1974@gmail.com
            nanomaterials@bsu.edu.az

**Journal covers original papers in experimental
and theoretical physics, chemistry and biology**